

ISSN 1451 - 9372(Print)  
ISSN 2217 - 7434(Online)  
JULY-SEPTEMBER 2022  
Vol.28, Number 3, 169-253

# Chemical Industry & Chemical Engineering Quarterly



The AChE Journal for Chemical Engineering,  
Biochemical Engineering, Chemical Technology,  
New Materials, Renewable Energy and Chemistry  
[www.ache.org.rs/ciceq](http://www.ache.org.rs/ciceq)



Journal of the  
Association of Chemical Engineers of  
Serbia, Belgrade, Serbia

**Chemical Industry &  
Chemical Engineering  
CI&CE Quarterly**

#### EDITOR-IN-CHIEF

**Vlada B. Veljković**

*Faculty of Technology, University of Niš, Leskovac, Serbia  
E-mail: veljkovicvb@yahoo.com*

#### ASSOCIATE EDITORS

**Jonjaua Ranogajec**

*Faculty of Technology, University of  
Novi Sad, Novi Sad, Serbia*

**Srdan Pejanović**

*Department of Chemical Engineering,  
Faculty of Technology and Metallurgy,  
University of Belgrade, Belgrade, Serbia*

**Milan Jakšić**

*ICEHT/FORTH, University of Patras,  
Patras, Greece*

#### EDITORIAL BOARD (Serbia)

**Dorđe Janačković, Sanja Podunavac-Kuzmanović, Viktor Nedović, Sandra Konstantinović, Ivanka Popović, Siniša Dodić, Zoran Todorović, Olivera Stamenković, Marija Tasić, Jelena Avramović, Goran Nikolić, Dunja Sokolović**

#### ADVISORY BOARD (International)

**Dragomir Bukur**

*Texas A&M University,*

*College Station, TX, USA*

**Milorad Dudukovic**

*Washington University,  
St. Luis, MO, USA*

**Jiri Hanika**

*Institute of Chemical Process Fundamentals, Academy of Sciences  
of the Czech Republic, Prague, Czech Republic*

**Maria Jose Cocero**

*University of Valladolid,  
Valladolid, Spain*

**Tajalli Keshavarz**

*University of Westminster,  
London, UK*

**Zeljko Knez**

*University of Maribor,  
Maribor, Slovenia*

**Igor Lacik**

*Polymer Institute of the Slovak Academy of Sciences,  
Bratislava, Slovakia*

**Denis Poncelet**

*ENITIAA, Nantes, France*

**Ljubisa Radovic**

*Pen State University,*

*PA, USA*

**Peter Raspor**

*University of Ljubljana,  
Ljubljana, Slovenia*

**Constantinos Vayenas**

*University of Patras,  
Patras, Greece*

**Xenophon Verykios**

*University of Patras,  
Patras, Greece*

**Ronnie Willaert**

*Vrije Universiteit,  
Brussel, Belgium*

**Gordana Vunjak Novakovic**

*Columbia University,  
New York, USA*

**Dimitrios P. Tassios**

*National Technical University of Athens,  
Athens, Greece*

**Hui Liu**

*China University of Geosciences, Wuhan, China*

#### FORMER EDITOR (2005-2007)

**Professor Dejan Skala**

*University of Belgrade, Faculty of Technology and Metallurgy, Belgrade, Serbia*



Journal of the  
Association of Chemical Engineers of  
Serbia, Belgrade, Serbia

**Chemical Industry &  
Chemical Engineering  
CI&CE Quarterly**

Vol. 28

Belgrade, July-September 2022

No. 3

Chemical Industry & Chemical Engineering  
Quarterly (ISSN 1451-9372) is published  
quarterly by the Association of Chemical  
Engineers of Serbia, Kneza Miloša 9/1,  
11000 Belgrade, Serbia

*Editor:*  
Vlada B. Veljković  
veljkovic@yahoo.com

*Editorial Office:*  
Kneza Miloša 9/1, 11000 Belgrade, Serbia  
Phone/Fax: +381 (0)11 3240 018  
E-mail: shi@yubc.net  
www.ache.org.rs

*For publisher:*  
Ivana T. Drvenica

*Secretary of the Editorial Office:*  
Slavica Desnica

*Marketing and advertising:*  
AChE Marketing Office  
Kneza Miloša 9/1, 11000 Belgrade, Serbia  
Phone/Fax: +381 (0)11 3240 018

Publication of this Journal is supported by the  
Ministry of Education, Science and  
Technological Development of the Republic of  
Serbia

Subscription and advertisements make payable  
to the account of the Association of Chemical  
Engineers of Serbia, Belgrade, No. 205-2172-  
71, Komercijalna banka a.d., Beograd

*Computer typeface and paging:*  
Marija Tasić

*Printed by:*  
Faculty of Technology and Metallurgy,  
Research and Development Centre of Printing  
Technology, Karnegijeva 4, P.O. Box 3503,  
11120 Belgrade, Serbia

*Abstracting/Indexing:*  
Articles published in this Journal are indexed in  
Thompson Reuters products: *Science Citation  
Index - Expanded™* - access via *Web of  
Science®*, part of *ISI Web of Knowledge™*

## CONTENTS

- R. Barathiraja, P. Thirumal, G. Saraswathy, I. Rahamathullah,  
**Effects of pretreatments on drying of Turkey berry (*Solanum  
torvum*) in fluidized bed dryer** ..... 169
- Alex Leandro Andrade de Lucena, Rayany Magali da Rocha  
Santana, Marcos André Soares de Oliveira, Luciano Costa  
Almeida, Marta Maria Menezes Bezerra Duarte, Daniella  
Carla Napoleão, **Evaluation of combined radiation for the  
treatment of lamivudine and zidovudine via AOP** ..... 179
- Bruna Pratto, Martha Suzana Rodrigues dos Santos-Rocha,  
Gustavo Batista, Inti Doraci Cavalcanti-Montaño, Carlos  
Alberto Galeano Suarez, Antonio José Gonçalves Cruz, Ruy  
de Sousa Júnior, **Rational feeding strategies of substrate  
and enzymes to enzymatic hydrolysis bioreactors** ..... 191
- Abulhassan Ali, Khuram Maqsood, Aymn Abdulrahman, Ahmad.S.  
Alsaadi, Abdullah Bin Mahfouz, **Optimal dissolution and  
viscoelastic behavior of polyamide-66 in formic acid for  
membrane fabrication** ..... 203
- Mia Radonjić, Jelena Petrović, Milena Milivojević, Milena  
Stevanović, Stojkovska Jasmina, Bojana Obradović,  
**Chemical engineering methods in analyses of 3D cancer cell  
cultures: Hydrodynamic and mass transport considerations**  
..... 211
- Predrag Kojić, Jovana Kojić, Milada Pezo, Jelena Krulj, Lato Pezo,  
Nikola Mirkov, **Numerical study of the hydrodynamics and  
mass transfer in the external loop airlift reactor** ..... 225
- Marija B. Tasić, Miona S. Stanković, Milan D. Kostić, Olivera S.  
Stamenković, Vlada B. Veljković, **Circular economy in apple  
processing industry: Biodiesel production from waste apple  
seeds** ..... 237
- Thayammal Ganesan Arul, Varatharaju Perumal, Rajasekaran  
Thanigaivelan, **Performance study of electrochemical  
micromachining using square composite electrode for copper**  
..... 247

**Activities of the Association of Chemical Engineers of Serbia are supported by:**

- Ministry of Education, Science and Technological Development, Republic of Serbia
- Hemofarm Koncern AD, Vršac, Serbia
- Faculty of Technology and Metallurgy, University of Belgrade, Belgrade, Serbia
- Faculty of Technology, University of Novi Sad, Novi Sad, Serbia
- Faculty of Technology, University of Niš, Leskovac, Serbia
- Institute of Chemistry, Technology and Metallurgy, University of Belgrade, Belgrade, Serbia

R. BARATHIRAJA <sup>1</sup>  
P. THIRUMAL <sup>1</sup>  
G. SARASWATHY <sup>2</sup>  
I. RAHAMATHULLAH <sup>3</sup>

<sup>1</sup> Department of Mechanical Engineering, Government College of Engineering, Bargur, India

<sup>2</sup> Department of Chemistry, Government College of Engineering, Bargur, India

<sup>3</sup> Department of Mechanical Engineering, Government College of Engineering, Srirangam, Tiruchirappalli, India

SCIENTIFIC PAPER

UDC 631/635:66.047

## EFFECTS OF PRETREATMENTS ON DRYING OF TURKEY BERRY (*Solanum torvum*) IN FLUIDIZED BED DRYER

### Article Highlights

- The combined pretreated drying process exhibits enhanced drying kinetics of the fruits
- The pretreated drying process resulted in improved qualities of the fruits
- Enhance the character of heat and mass transfer by both physical and chemical treatments

### Abstract

*The influence of pretreatment methods like physical, chemical, combined physical, and hybrid treatments on the Turkey berry (*Solanum torvum*) fruits to enhance the water diffusion during drying was assessed due to removing a waxy layer on the peel. Pretreated and untreated samples were dried at 70 °C and 4 m/s of air flow in a fluidized bed dryer. Fruits pretreated with combined abrasion and blanching have the lowest drying time and good vitamin C content retention of 36%. The highest drying rate of 0.396 kg water/kg<sub>db</sub> min<sup>-1</sup>, maximum effective moisture diffusivity of 6.002 × 10<sup>-10</sup> m<sup>2</sup>/s, and volumetric shrinkage ratio of 0.68 were obtained for fruits that undergone combined physical pretreatment along with drying. The maximum change in color ΔE = 14.75 and Chroma ΔC = - 10.53 were obtained for the untreated samples.*

*Keywords: color, effective moisture diffusivity, pretreatment, shrinkage, Turkey berry, vitamin C.*

Turkey's berry fruits are like green peas that grow in clusters of tiny green spheres, identified as *Solanum torvum* in the family of Solanaceae. Every hundred grams of young Turkey berry fruit are a good source of important micro-nutrients, like 104 mg Ca, 70 mg P, 4.6 mg Fe, 390 μg β-carotene, and 4 mg ascorbic acid, as well as 85.4 g of water [1]. However, this fruit quickly deteriorates with spoilage and thus needs techniques for conservation.

The high moisture content of agri-food-stuffs makes it difficult to preserve for a long time. Removing the water content by drying extends the self-life of those products. As a result, it prevents the growth and reproduction of microorganisms [2-4]. Furthermore, food-stuffs are susceptible to drying environments

such as processing temperature, inlet fluid flow, relative humidity that can lead to the quality degradation of the products by oxidation, changes in color, and loss of physical and biochemical properties [5].

Drying significantly decreases food-stuff weight and volume and brings many advantages such as reducing packaging and transport cost and storage space [2-4]. Commercially many kinds of dryers were available in the market like convection dryer, fluidized bed dryer, microwave dryer, drum dryer, freeze dryer, solar dryer, infra-red radiation dryer, etc. Fluidized bed drying has been widely used to dry food products [6].

Fluidized bed drying, which considerably eliminates the water content from the sample with a high degree of thermal efficiency, has been recognized for uniform drying with excellent heat and mass transfer [7-8]. Also, FBD is a convenient method that avoids overheating food products that are heat sensitive. It has been stated that pretreatment of agri-food-stuffs before dehydration can improve the drying kinetics and minimize unnecessary changes in physical and bio-

Correspondence: P. Thirumal, Department of Mechanical Engineering, Government College of Engineering, Bargur, India.  
E-mail: ptml76@gmail.com  
Paper received: 20 November, 2020  
Paper revised: 22 July, 2021  
Paper accepted: 6 August, 2021

chemical properties like color, texture, shrinkage, micro-nutrients, etc. [2].

The drying of Turkey berry fruits is restricted by a waxy skin layer similar to grapes, Cape gooseberry, plums, and cheery fruits, preventing water movement across the peel and slowing the drying rate [5]. Agricultural food products with waxy skin have been pretreated physically, chemically, and in combination to improve drying characteristics, as has been reported by many authors [9-13].

Physical pretreatments such as blanching, skin puncturing, and surface abrasion preceding the dehydration of samples are typically intended to promote water transfer mechanisms. Blanching can be carried out either at “short-time” with a high temperature or at “long-time” with low temperatures, and its performance depends on the selection of process [9,14]. Adeletta *et al.* [5] revealed that grapes treated with skin abrasion and dehydrated at low temperatures could reduce changes in physicochemical properties. In forced convection dryer, cape gooseberry fruits pretreated by physical and chemical resulted in better final qualities and drying kinetics [9].

In this present investigation, the effects of Turkey berry's physical, chemical, combined physical, and hybrid pretreatments on drying kinetics, physical, and nutritional properties were analyzed in a fluidized bed dryer. The influence of the edible oils with varying concentrations and the soaking time was studied.

## MATERIALS AND METHODS

### Samples preparation

Turkey berries with  $12.5 \pm 0.5$  mm average diameter and weighing  $2 \pm 0.2$  g were used for the experiments. Samples were collected from the native market at Krishnagiri town of Tamilnadu, India. About 10 g of fresh fruits were taken to study the sample's initial moisture content, and the average moisture content is measured as suggested by the AOAC method [15]. From the test, the initial moisture content of fruit is observed as  $84 \pm 1\%$  on a wet basis (w.b.), and each test was carried out thrice.

### Pretreatment preparations

The details of the physical and chemical pretreatment processes used are listed in Table 1. Sample and solutions were prepared freshly for each treatment with a ratio of 1:2.5 (fruits: solution). Untreated (T1), two physically treated (T2 & T3), two combined physically treated (T4 & T5), four chemically treated (T6, T7, T8, and T10), and one combined

physically and chemically treated (T9) were prepared.

Table 1. Pretreatment methods of samples

Treatment	Description
T1	Samples were untreated (control process)
T2 <sup>a</sup>	Samples balanced by hot water immersion at 90 °C for 20 s
T3	Abrasive treatment 30 min at 30 rpm
T4 <sup>a</sup>	Abrasive treatment + Hot water at 90 °C for 20 s
T5 <sup>a</sup>	Hot water at 90 °C for 20 s + Abrasive treatment
T6	Peanut oil (9.5%) + K <sub>2</sub> CO <sub>3</sub> (4.75%) 60 min
T7	Sesame oil (9.5%) + K <sub>2</sub> CO <sub>3</sub> (4.75%) 60 min
T8	Sesame oil (0.5%) + K <sub>2</sub> CO <sub>3</sub> (4.75%) (soaking time - 60 min)
T9 <sup>a</sup>	Sesame oil (5%) + KOH (1.5%) 90 °C 20 s
T10	Sesame oil (0.5%) + K <sub>2</sub> CO <sub>3</sub> (4.75%) (soaking time - 30 min)

<sup>a</sup>The samples were cooled down to room temperature by cold water until the residual surface water was extracted.

After the pretreatment processes, the fruits were cleaned with the help of tissue paper, in which water on the sample surface was absorbed. In chemical pretreatments, the fruits were immersed in solutions at an average temperature of 30 °C and stirred continuously for 60 min using a Laboratory magnetic stirrer at 300 rpm except for the T10 (Remi Laboratory Instruments, Maharashtra, India).

Abrasion of the samples T3, T4, and T5 were executed on a mechanized revolving drum with a diameter of 250 mm, length of 400 mm, and made of acrylic material with sandpaper (Grit 400) pasted inside the drum. The rotation speed of the drum was kept at 30 rpm and the pretreatment time was 30 min. The T6 and T7 processes have been conducted to examine the impact of the same chemical compound comprising two different oils. The chemical pretreatments (T7, T8, and T10) of a sesame oil solution were carried out with K<sub>2</sub>CO<sub>3</sub> at various solution concentrations and soaking times. Similarly, the pretreatment T9 was carried out by KOH and sesame oil with blanching. After the pretreatment, the samples were dried at room temperature on an absorbent paper before feeding to the drying chamber.

### Experimental set-up and procedure

A laboratory-scale fluidized bed dryer, as shown in Figure 1, was used to analyze the drying properties of the Turkey berry. The FBD has a centrifugal blower with a variable frequency drive controller, an electric heater, and a bag filter. The drying chamber (height 0.9 m and

inner diameter 0.15 m), made of stainless steel, is connected with a truncated cone (the funnel) of a total disengagement height (TDH) of 1.2 m and a top diameter of 0.25 m. The air flew into the bed through a perforated stainless steel plate (an open area of  $20 \pm 0.05\%$ ) with  $4.0 \pm 0.01$  mm diameter holes in a triangular pitch of  $8.0 \pm 0.02$  mm. The inlet air velocity was measured with an anemometer (AM-4201) with an accuracy of 0.1 m/s. The air was heated by an electric heater and sent to the drying chamber. In all drying processes, the investigations were conducted at an inlet air temperature of  $70^\circ\text{C}$  and an inlet air velocity of 4 m/s.

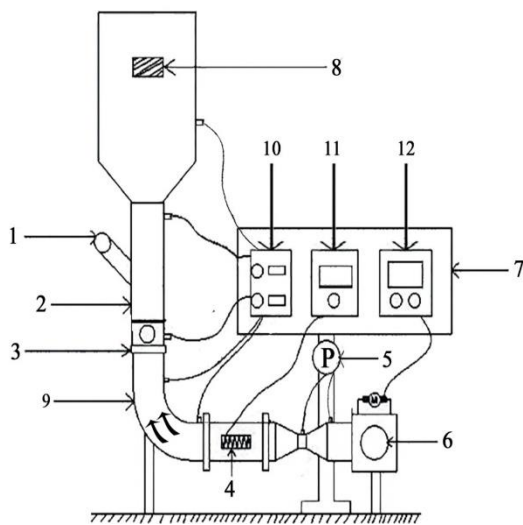


Figure 1. Schematic diagram of FBD setup: (1) inlet port (2) drying chamber (3) air distributor (4) electrical heater (5) differential pressure sensor (6) blower (7) control unit (8) filter-bag (9) plenum chamber (10) temperature indicator (11) energy meter (12) VFD controller.

The pretreated samples were placed into the drying chamber when the bed reached a stable state by controlling the temperature and the air flow rate. At time intervals of 10 min, the whole sample was unloaded from the drying chamber, and the weight was measured using a digital weighing balance (Kerro, BL5002, range 0 g - 500 g) with a reading accuracy of 0.01 g. After weight measurement, the sample was again loaded into the drying chamber for another 10 min to reduce its moisture content further. The loading of the fruits proceeded until the moisture content reduced below  $14 \pm 0.5\%$  (d.b). To confirm the repeatability of the analysis, three runs were conducted for every drying process.

### Response variables

The effect of physically, chemically, combined physically, and combined physiochemically pretreated

fruit samples on the fluidized bed drying were evaluated by measuring the drying time and rate throughout the drying process, together with the color, shrinkage, and vitamin C.

### Response variables

Drying kinetics was investigated by assessing the weight reduction of a sample with time. Drying curves can be denoted in many ways, such as variations of the moisture content and the drying rate with time or the drying rate as a function of the moisture content. The moisture content of Turkey berry is assessed on a dry basis (d.b.) using the following equation [8, 16]:

$$M_{db} = \left( \frac{W_{st} - W_{dry}}{W_{dry}} \right) \quad (1)$$

The moisture ratio (MR) of Turkey berry during the drying experiments is calculated by using the following equation [11, 17]:

$$MR = \left( \frac{M_{st} - M_{eq}}{M_{in} - M_{eq}} \right) \quad (2)$$

The above formula can also be modified to  $MR = M_{st} / M_{in}$ . The unit of MR is dimensionless. The drying rate (DR) of Turkey berry during dehydration was calculated using Eq. (3) [16, 17]:

$$\text{Drying Rate} = \left( \frac{M_{s,t_1} - M_{s,t_2}}{t_1 - t_2} \right) \quad (3)$$

### Determination of effective moisture diffusivity

Fick's second law of diffusion equation was used to investigate dehydration data and estimate the effective moisture diffusivity ( $D_{eff}$ ):

$$\frac{\partial M}{\partial t} = D_{eff} \frac{\partial^2}{\partial t} \quad (4)$$

Assuming the sample is spherical and moisture movement occurs only by diffusion, the moisture ratio can be calculated using the formula of Eq. 5. [11, 17]:

$$MR = \frac{M_{st} - M_{eq}}{M_{in} - M_{eq}} = \frac{6}{\pi^2} \sum_{n=1}^{\infty} \frac{1}{n^2} \exp\left( \frac{-D_{eff} n^2 \pi^2 t}{R_p^2} \right) \quad (5)$$

For long drying times when the moisture ratio is greater than 0.6, the first term in their series of equations can be considered, and then the Eq. (5) can be rewritten as Eq. (6) [11, 17]:

$$MR = \left( \frac{6}{\pi^2} \right) \exp\left( \frac{-D_{eff} \pi^2 t}{R_p^2} \right) \quad (6)$$

By taking natural logarithm on both sides, Eq. (6) can be linearized to Eq. (7):

$$\ln MR = \ln \left( \frac{M_{st} - M_{eq}}{M_{in} - M_{eq}} \right) = \ln \left( \frac{6}{\pi^2} \right) - \left( \frac{D_{eff} \pi^2 t}{R_p^2} \right) \quad (7)$$

The linear slope  $S_1$  is determined by plotting  $\ln(MR)$  against  $t$ .

$$S_1 = \left( \frac{D_{eff} \pi^2}{R_p^2} \right) \quad (8)$$

### Volumetric shrinkage ( $S_p$ )

The sample volumes have been measured with the help of a digital Vernier caliper by three measurements of the young Turkey berry diameter in the respective coordinate axes. During the dehydration, three samples were measured for every test. The volume reduction was acquired as a ratio of the sample volume at any time of dehydration ( $V_{s,t}$ ) to the original volume of the fruit ( $V_{in}$ ).

According to the following equation, as mentioned by Junquera *et al.* [18], a second-order polynomial equation is suitable for the relationship between variations in volume ratio to sample moisture content, as described in Eq. (9):

$$\frac{V_{s,t}}{V_{in}} = a_1 M_{s,t}^2 + b_1 M_{s,t} + c_1 \quad (9)$$

### Color measurement

A tri-stimulus colorimeter (model 2810) was used to test the Turkey berry color under a D65 illuminated lamp at a 10° viewing angle, calibrated with the help of a white ceramic tile. Color values were represented as L- varying from lightness to darkness (100-0), "a" varying from redness to greenness (+ ve to - ve), and "b" varying from yellowness to blueness (+ ve to - ve), on the Hunter scale; the subscripts of 'fi' and 'in' denotes final and initial value. Three measurements were taken for each sample at three different places, and the average value was recorded. The following values of the total color difference (TCD or  $\Delta E$ ) and the Chroma differences ( $\Delta C$ ) were calculated from the values of "L", "a" and "b" [9,19].

$$\Delta E = \sqrt{(L_{fi} - L_{in})^2 + (a_{fi} - a_{in})^2 + (b_{fi} - b_{in})^2} \quad (10)$$

$$\Delta C = C_{fi} - C_{in} \quad (11)$$

$$C_{fi} = \sqrt{(a_{fi})^2 + (b_{fi})^2} \quad (12)$$

$$C_{in} = \sqrt{(a_{in})^2 + (b_{in})^2} \quad (13)$$

### Ascorbic acid content (AA)

Ascorbic acid content was evaluated (AA or

vitamin C) using 2,4-dinitrophenyl hydrazine [18], as described by the colorimetric procedure. AA was extricated with 0.5% oxalic acid, purified, and dosed up in the extract. Then, the absorbance was measured at 520 nm by a spectrophotometer using the standard AA; the measurements were repeated thrice, and their values were given in mg/100 g.

### Microstructure analysis

The microstructure of dehydrated turkey berries was examined using a scanning electron microscope (VEGA3, TESCAN). To acquire SEM pictures, tiny fragments were collected from the fruit skin and covered with a fine layer of Nano-gold under a high vacuum to offer an illuminating surface for the electron beam. The gold coating was deposited on the sputter coater (SC-7620, Mini Sputter Coater) with argon gas as a medium at a pressure lower than the atmosphere.

### Statistical evaluation of the quality analysis

Three batches were independently conducted for every drying test, and the data were mutually analyzed. Result analysis of one-way ANOVA was performed using the software IBM SPSS Statistics 22.0. To find statistical significance, different variables were compared using the Tukey test at a confidence level of 95% [20]. The results obtained were presented as mean values with a standard deviation.

## RESULTS AND DISCUSSION

### Drying curves

To examine the effect of different pretreatment methods on the drying kinetics of Turkey berry, the curves showing the variation of the moisture content with time were analyzed (Figure 2). The initial moisture content of  $5.25 \pm 0.05$  (kg water/kg dry matter) was reduced to final moisture content. It was observed that a higher amount of water was removed from the pretreated samples than from the untreated ones.

The untreated samples were dried for 645 min. Similarly, the drying duration for the physically pretreated samples (T2 and T3) was from 495 min to 530 min, while the chemically pretreated samples (T6, T7, T8, and T10) took 480 to 580 min. The drying times of the hybrid (T9) and combined physical (T4 and T5) pretreatments were 420 min and 330-400 min, respectively, thus being shorter by 38-49% and 34% than the untreated samples.

The combined physically pretreated samples (T5 and T4) dipped in hot water (blanching) with abrasive before the dehydration process had shorter drying times than the other samples. The T5 samples were initially blanched, followed by a friction process. As a result, the



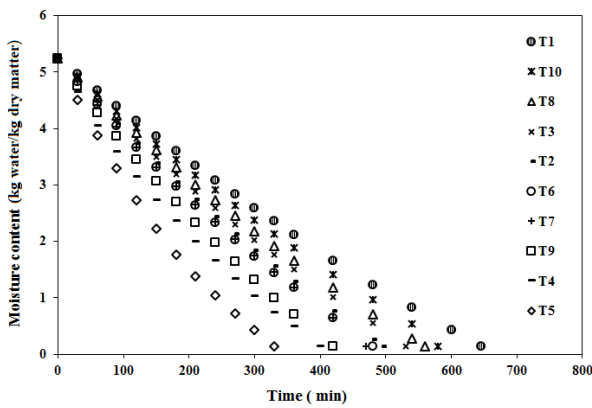


Figure 2. Evolution of moisture content of pretreated samples during drying at 70 °C and 4 m/s.

softened solid tissues were obtained, and the microscopic cracks on the fruits were effectively developed. At the same time, the T4 process created the micro-cracks initially, which might be partially closed by the effect of swelling due to the blanching action. Hence, the T5 process was approximately 17.5% shorter than the T4 one.

From the analysis of the drying curve and variability, it was found that the oil type in the T6 and T7 samples had an insignificant effect during the dehydration of fruit, and its drying time was observed as 430 and 435 min. The drying curve of the T7 sample showed that the drying rate was higher than that of the T8 sample while using a high concentration of Sesame oil. However, increasing the immersion period for the T8 sample, compared to the T10 sample, did not affect the dehydration process. Significant differences were observed for the T2, T4, T5, and T9 samples. Still, the curve shows no considerable difference when the T4 and T9 samples were compared during the dehydration process.

Figure 3 shows the time variations of the drying rate for the fruits. The maximum dehydration rate occurred for the fruit pretreatments in the following order: T5, T4, and T9, followed by the remaining processes. In addition, the drying rate of the samples from the combined physical and hybrid pretreatment was approximately 2.5 times and twice higher for the T5 and the T9 samples than for the untreated samples. A similar result was obtained as grapes dried in a convective dryer [5]. The experimental results confirm that the exposure of the samples to the physical and chemical pretreatment increases the drying rate positively.

The fruit's wax layer is exposed to high temperatures, converting the cellular structure of solids from anisotropic to isotropic, subsequently increasing the permeability of the peel surface. Similarly,

chemical pretreatments of peanut or sesame oil with a salt solution alter the texture of the fruit's wax layer and reduce surface tension, resulting in improved water permeability of the samples. In addition, these “fatty acids” interrelate with soluble waxes and establish “hydrophilic” relationships between the fruit surface [9] and the water-rich cellular tissue (intra and inter cells). Similar results were observed in several products, such as red kidney bean seeds [2], grapes [5], cape gooseberries [9], and plums [11].

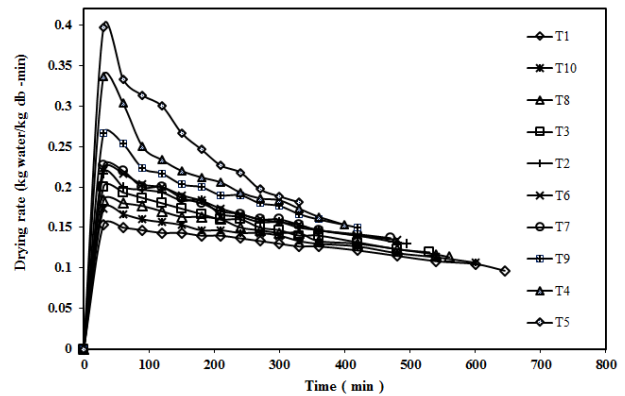


Figure 3. Drying rate (DR) of pretreated Turkey berries drying at 70 °C and 4 m/s.

**Effective moisture diffusivity**

The relation of  $\ln(MR)$  with time for various pretreated and untreated samples can be seen in Figure 4. The  $D_{eff}$  values of the fruits computed using Eq.7, along with the coefficient of determination ( $R^2$ ), are presented in Table 2.

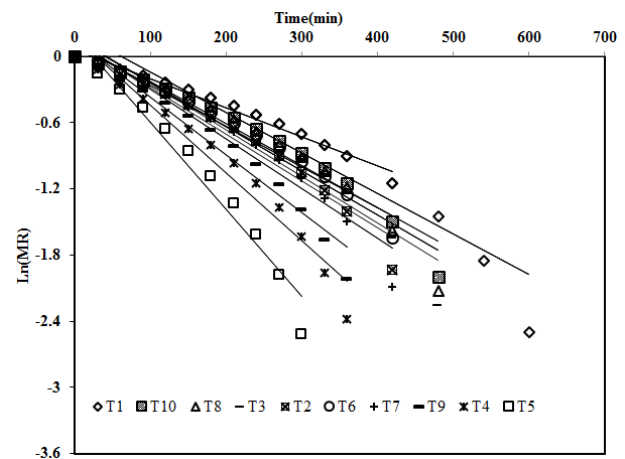


Figure 4.  $\ln(MR)$  vs. time for different pretreated samples during drying at 70 °C and 4 m/s.

The  $D_{eff}$  values of the pretreated and untreated samples range from  $2.928 \times 10^{-10} \text{ m}^2\text{s}^{-1}$  to  $6.002 \times 10^{-10} \text{ m}^2\text{s}^{-1}$  and are within the range of  $10^{-11} \text{ m}^2\text{s}^{-1}$  to

Table 2. Variation of moisture diffusivity coefficients ( $D_{eff}$ ) and volumetric shrinkage coefficients

Parameters		T1	T2	T3	T4	T5	T6	T7	T8	T9	T10
Shrinkage ( $S_p$ )	a	0.0012	-0.0032	-0.0049	-0.0078	-0.0076	-0.002	-0.0045	-0.0028	0.001	-0.003
	b	0.0971	0.1011	0.1145	0.1075	0.1006	0.0969	0.0979	0.1157	0.066	0.1182
	c	0.4451	0.5552	0.5265	0.6495	0.6781	0.5585	0.6057	0.4694	0.6352	0.4509
	$R^2$	0.9979	0.9972	0.9934	0.9969	0.9946	0.9945	0.9934	0.9924	0.9962	0.9925
Effective moisture diffusivity ( $m^2/s$ )	$\times 10^{-10}$	2.928	4.154	3.769	5.543	6.002	4.308	4.385	3.462	5.232	3.154
	$R^2$	0.924	0.959	0.941	0.959	0.962	0.951	0.959	0.945	0.958	0.952

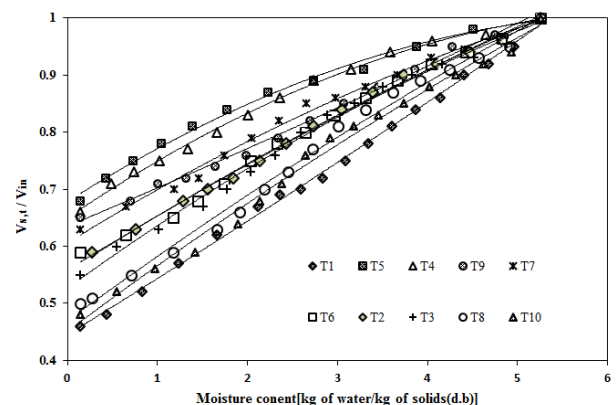
$10^{-8} m^2s^{-1}$  found for several agri-products [17]. For the untreated samples, the effective moisture diffusivity is  $2.928 \times 10^{-10} m^2s^{-1}$ . In the case of the physically pretreated samples (T2 and T3), the effective moisture diffusivity was  $4.154 \times 10^{-10} m^2s^{-1}$  and  $3.769 \times 10^{-10} m^2s^{-1}$ , respectively, whereas for the chemical pretreated samples (T6, T7, T8, and T10) range from  $3.154 \times 10^{-10} m^2s^{-1}$  to  $4.385 \times 10^{-10} m^2s^{-1}$ . The effective moisture diffusivity of the T9 sample is  $5.232 \times 10^{-10} m^2s^{-1}$ , while for the combined physically pretreated samples (T4 and T5), it is  $5.543 \times 10^{-10} m^2s^{-1}$  to  $6.002 \times 10^{-10} m^2s^{-1}$ . The  $D_{eff}$  value of the T5 sample increases drastically due to higher micropores and cracks, increasing the mass transfer efficiency during drying.

Similarly, for high-temperature physical, combined physical, and hybrid pretreatment methods, the action of "turgidity" reduces considerably and improves the porosity of sample tissues. Consequently, it enhances the sample's permeability [5]. Chemical pretreatments alter the peel structure of the fruit and minimize the surface tension effect on the cell wall. The above-mentioned causes for the pretreated samples positively enhance the effective moisture diffusivity by modifying the cell membrane structures. Effective moisture diffusivity is directly proportional to the drying rate [5,9].

### Volumetric shrinkage

The volume ratio ( $V_{s,t}/V_{in}$ ) was calculated to evaluate the volume reduction of turkey berries during dehydration while the volume of fresh fruit was  $0.144 \pm 0.002 \times 10^{-5} m^3$ . The effect of the change in volume ratio against the reduction in moisture content is shown in Figure 5. When the samples reached the specified final moisture content, the highest volumetric shrinkage ratio of 0.68 and 0.66 was found in the T5 and T4 samples, respectively. In contrast, the lowest value of 0.46 was found for the T1 sample.

Typically, when samples are subjected to an extended dehydration process resulting injuries to the

Figure 5. Volumetric shrinkage of different pretreated samples during drying at  $70^\circ C$  and 4 m/s.

cell structure and induce significant shrinkage of the volume [18]. Figure 5 shows that chemical, combined physical, and hybrid pretreatments lead to a slight volume change and have an optimistic effect on maintaining the structure of the dried fruit. In this study, it was observed that the volumetric shrinkage was inversely proportional to the drying rate.

The second-order polynomial equation, Eq. (2), was adopted to correlate the moisture content and the volumetric ratio. Table 2 shows the  $R^2$ -values and the parameters of Eq. (2) for all pretreated and untreated samples. In addition, the higher values of  $R^2$  (0.9) demonstrate that the equation is in excellent agreement with the experimental data [5].

### Color

Color is one of the essential consistent proof of food quality in the food industry. To calculate the color change in fruit, Eqs.(10-13) were used. Table 3 shows the color variations of dried fruits, which are affected by the physical and chemical preparations, and the actual values of fresh and dehydrated turkey berries. Fresh fruit color values were measured as the lightness of 70.77, the greenness of-7.78, and the yellowness of 26.38, as shown in Table 3. The lightness values of untreated, physical, and combined physically pre-

treated samples were decreased to some extent, whereas in the chemically and hybrid pretreated samples were increased marginally. Table 3 shows that the final value of lightness ( $L^*$ ) varied from 62.28 to 66.18 for the physical and combined physical pretreated dried samples. In contrast, for the chemically and physicochemically pretreated samples, the values ranged from 72.86 to 75.23, while for the untreated sample, it was 60.46.

The final  $a^*$ -value varied from -5.64 to -4.68 in the case of the physically and combined physically pretreated samples, whereas for the chemical and hybrid pretreated samples, it varied from 1.98 to -5.78; for the untreated samples, it was -4.28. Similarly, the final value of  $b^*$  varied from 17.46 to 19.22 for the physically and combined physically pretreated samples, whereas the chemically and physicochemically pretreated samples ranged from 19.81 to 29.16; for the untreated samples, it was 16.43 (Table 3).

The total color differences (TCD or  $\Delta E$ ) of the pretreated samples were found as significantly different ( $\alpha < 0.05$ ) (Table 3). The TCD values of physical and combined physical treated dried samples varied from 8.55 to 12.7, whereas chemical and hybrid treated dried samples ranged from 7.18 to 10.88. The untreated sample value of 14.75 was observed from this study.

During the dehydration process, the untreated sample was dried prolonged time; consequently, the sample was strongly affected by the caramelization and enzymatic browning reactions. Generally, when the foodstuffs are exposed to high-temperature conditions, the oxidation of total phenolic acids and the chemical reactions of carbohydrates or amino acids occur in foodstuff. The degree of color change depended on the drying temperature, processing time, and oxygen level in the air used in the process [21].

Compared with the untreated sample, less degradation of color was observed in the abrasion-treated fruits (T3). In the HTST process, the least color damage occurs in thermal treatment, inhibiting the enzymatic browning due to the inactivation of polyphenol-oxidase (PPO) during the drying [20,22]. The degradation of skin color on the sample was observed in the HTST processes, as listed in the table in the following order: T4 > T2 > T5 > T9.

Based on the experimental results, the lowest degree of darkening was found in all chemically pretreated samples (highest L-values). The edible oils, such as peanut and sesame oils, were used in the T6-T10 treatments to help to mitigate the changes in the color of the fruit due to the development of a defensive coating on the outer surface of the samples. Thus, the

chemical and hybrid treated samples were preventive against oxidation and controlled the caramelization and enzymatic browning reactions during the dehydration process [9].

Chroma represents the degree of color; it has varied from low Chroma values (dull colors) to high Chroma values (bright colors). From Table 3, Chroma ( $\Delta C$ ) variations are negative for the pretreated and untreated samples except for the T7, T8, and T10 samples. This result indicates that the drying processes with the chemically pretreated samples were better than those with the physically pretreated ones. From Table 3, the difference in Chroma values confirms the color saturation shown in the photo images. The visuals of the fruits are sequenced as dark to bright color in Table 3 as in this progression: T1 < T4 < T3 < T5 < T2 < T9 < T6 and T8 < T10 < T7.












#### Ascorbic acid retention

Table 3 displays the content of ascorbic acid (vitamin C) in the dehydrated Turkey berries. The vitamin C content of fresh fruit is  $3.81 \pm 0.32$  mg/100 g (d.b.). This is in line with the earlier reports showing that the vitamin C content in Turkey berries is 2.86 mg/100 g [1] and 4 mg/100 g [23]. The vitamin C losses of the untreated and treated samples were significantly different ( $\alpha < 0.05$ ) as observed in the dehydration process (Table 3). Unavoidable losses of vitamin C occurred due to its thermo-sensitivity character during the drying at 70 °C. Even though HTST achieved a short drying time in the case of the pretreated samples of T4, T5, and T9, the vitamin C losses were inevitable because of its solubility in water and sensitivity to heat during the blanching. Based on the experimental results, 34-36% of vitamin C content was retained in the T4, T5, and T9 samples.

Significant variations in the average values of the vitamin C content of dried berries in different pretreatments were observed by the analysis of variance ( $\alpha < 0.05$ ). Vitamin C retention was higher in the physically pretreated samples, like the abrasively treated T3 sample, and the combined physically treated T4 and T5 samples, than in the untreated sample. Both blanching and abrasion prevented the samples from the influence of O<sub>2</sub> during the period of dehydration and minimal changes in the skin with short drying [10]. The untreated dried sample showed a significant loss of 70% in vitamin C due to the prolonged drying time of 645 min.

Despite the different oil types, the maximum ascorbic acid retention of 41% and 39% was found in the T6 and T7 samples, respectively. The vitamin E contents of peanut and sesame oil are 398.6 mg/kg and 450 mg/kg, respectively [24-25]. Thus, Vitamin E from

Table 3. Colour and nutrition evaluation of Turkey Berry fruits dried after chemical and physical pretreatments

Parameters	Fresh	T1	T2	T3	T4	T5	T6	T7	T8	T9	T10
L*	70.77 <sup>bc</sup> ±1.36	60.46 <sup>f</sup> ±1.06	65.60 <sup>de</sup> ±1.86	62.28 <sup>ef</sup> ±1.12	64.14 <sup>ef</sup> ±1.42	66.18 <sup>cd</sup> ±1.08	73.23 <sup>abc</sup> ±1.08	75.23 <sup>a</sup> ±2.36	74.72 <sup>ab</sup> ±2.32	72.86 <sup>abc</sup> ±1.96	74.63 <sup>ab</sup> ±2.06
a*	-7.78 <sup>b</sup> ±1.24	-4.28 <sup>b</sup> ±1.98	-5.64 <sup>b</sup> ±2.44	-4.68 <sup>b</sup> ±1.88	-5.28 <sup>b</sup> ±2.02	-5.64 <sup>b</sup> ±2.12	1.88 <sup>a</sup> ±2.12	1.98 <sup>a</sup> ±0.86	1.94 <sup>a</sup> ±0.44	-5.78 <sup>b</sup> ±2.22	1.98 <sup>a</sup> ±1.02
b*	26.38 <sup>a</sup> ±1.24	16.43 <sup>f</sup> ±1.14	19.22 <sup>bc</sup> ±2.44	17.46 <sup>e</sup> ±1.08	18.85 <sup>b</sup> ±1.36	19.12 <sup>bc</sup> ±1.12	29.04 <sup>a</sup> ±1.12	29.16 <sup>a</sup> ±3.24	28.52 <sup>a</sup> ±2.66	19.81 <sup>bc</sup> ±3.04	28.42 <sup>a</sup> ±2.86
ΔE	-	14.75 <sup>a</sup> ±0.35	9.09 <sup>cd</sup> ±1.08	12.70 <sup>b</sup> ±0.33	10.34 <sup>bc</sup> ±0.05	8.55 <sup>cd</sup> ±0.30	10.32 <sup>bc</sup> ±0.30	10.88 <sup>bc</sup> ±0.31	10.70 <sup>bc</sup> ±0.42	7.18 <sup>a</sup> ±1.33	10.69 <sup>bc</sup> ±0.03
ΔC	-	-10.53 <sup>c</sup> ±0.15	-7.47 <sup>c</sup> ±0.88	-9.43 <sup>c</sup> ±0.20	-7.93 <sup>c</sup> ±0.05	-7.57 <sup>c</sup> ±0.20	1.60 <sup>a</sup> ±0.20	0.73 <sup>ab</sup> ±1.54	0.47 <sup>ab</sup> ±1.94	-6.87 <sup>c</sup> ±1.52	0.99 <sup>a</sup> ±0.27
mg/100g*	3.81 <sup>a</sup> ±0.02	1.14 <sup>f</sup> ±0.02	0.95 <sup>g</sup> ±0.05	1.16 <sup>de</sup> ±0.02	1.26 <sup>d</sup> ±0.04	1.33 <sup>cd</sup> ±0.06	1.48 <sup>bc</sup> ±0.05	1.42 <sup>bc</sup> ±0.03	1.22 <sup>ef</sup> ±0.02	0.97 <sup>g</sup> ±0.06	1.14 <sup>f</sup> ±0.04
Picture											

\*Ascorbic acid content , Means followed by the same letter are not significantly different using the Tukey test (alpha = 0.05).

peanut and sesame oils donates free radicals to vitamin C for regeneration during drying, where the antioxidants prevent one another and strengthen oxidation resistance.

The experimental results reveal that vitamin C retention depends on processing temperature, pretreatment option, and drying time. However, the processing temperature plays a significant role in preserving the vitamin C content.

**Microstructure evaluation**

Microstructure evaluation was done by Scanning Electron Microscopy (SEM) to study the effects of the chemical and physical pretreatment processes (T1, T5, T6, T7, and T9) that occurred at high drying rates compared to the untreated samples. The SEM images of the samples before and after drying are shown in Figure 6.

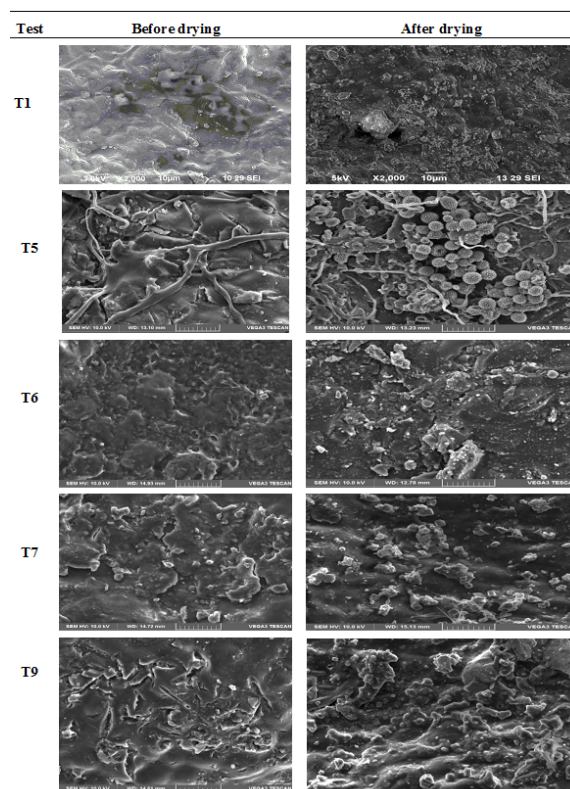


Figure 6. SEM images of fresh and dried Turkey berries.

Typical surface wax in fresh Turkey berry is shown in Figure 6. The better wax removal and the developed micro-cracks were observed in the combined physical pretreatment of T5 before drying. Formation of micro-pores and fully developed micro-cracks were visible after drying in the SEM image due to blanching with abrasion action. These micro-pores and micro-cracks support the shorter drying time of 330 min, shown in Figure 2. Microstructure evaluation

images of the chemically pretreated samples T6 and T7 were similar. The images before drying show traces of wax on the surface, and micro-cracks are minimal compared to the T5 sample. After drying, the images of the T6 and T7 samples show fully developed micro-cracks and minimal micro pores compared to the T5 sample. The images of the T9 sample taken before and after drying show better micro-cracks and pores on the surface than the T6 and T7 samples. The primary structure of the cell membrane of the sample was disturbed because of the chemical and HTST actions [12,20].

SEM images show the effect of the chemical pretreatment in which micro-cracks were created in Turkey berry fruit peel by potassium carbonate and potassium hydroxide, with oil solution, resulting in a rapid drying rate. As well as in abrasion, treatment did not involve any loss of juice since not one big crack was observed either after the physical pretreatment or after drying in addition to the increased drying rate efficiently [5,9].

## CONCLUSION

The effects of different pretreatments like an untreated, physical, chemical, combine and hybrid, on the drying kinetics and their qualities of Turkey berries were investigated using a fluidized bed dryer. Physical and chemical treatments have shortened drying times by reducing the samples' waxy skin obstinacy and enhanced heat and mass transfer.

Better wax removal and micro-cracks were produced in the combined physical and hybrid pretreatment methods followed by other pretreatment methods. Higher effective moisture diffusivity was obtained in the dehydration of Turkey berries when the fruits were exposed to combined physical and hybrid pretreatment. The combined physical pretreatment had the shortest drying time, the lowest shrinkage, acceptable retention of vitamin C, and color change were observed. In the HTST processing of the T9 sample, the loss of color was comparatively lower than that caused by the blanching and combined physical treatments. Increasing the time of immersing the chemically pretreated sample in the solution did not affect the drying process significantly. The chemical pretreatment with sesame oil of 9.5% and potassium carbonate of 4.75% was desirable to preserve the biochemical properties, like vitamin C retention. The processing temperature plays an important role in maintaining vitamin C content.

## NOMENCLATURE

$a_1, b_1, c_1$	Quadratic equation constant, (dimensionless)
$D_0$	Preexponential factor of the Arrhenius equation, (m <sup>2</sup> /s)
$D_{eff}$	Effective moisture diffusivity, (m <sup>2</sup> /s)
DR	Drying rate a kg water/ kg dry matter x min
$S_1$	Slope of the line, (dimensionless)
$M_s$	Moisture content of the sample, (kg water / kg dry matter)
$M_{in}$	Initial moisture content of the sample, (kg water / kg dry matter)
$M_{eq}$	Equilibrium moisture content of the sample, (kg water/kg dry matter)
$M_{st}$	Moisture content at any time, (kg water/kg dry matter)
MR	Moisture ratio, (dimensionless)
$n$	Constant, positive integer of the equation
$R_p$	Radius of product, (m)
$S_p$	Shrinkage percentage of product, (dimensionless)
$t, t_1, t_2$	Time, (s)
$V_{in}$	Initial volume of sample, (m <sup>3</sup> )
$V_{s,t}$	Volume of sample at any time, (m <sup>3</sup> )
$W_{st}$	Sample weight at a specific time (g)
$W_{dry}$	Sample dry weight (g)
HTST	High temperature short time
K <sub>2</sub> CO <sub>3</sub>	Potassium carbonate
KOH	Potassium hydroxide
$\Delta E$	Total color difference

## REFERENCES

- [1] P.N.Y. Otu, F. Sarpong, J.E. Gidah, A.M. Labanan, D. Anim, *Afr. J. Food, Agric., Nutr. Dev.* 1 (2017) 9-14.
- [2] L.Z. Deng, A.S. Mujumdar, Q. Zhang, X.H. Yang, J. Wang, Z.A. Zheng, H.W. Xiao, *Crit. Rev. Food Sci. Nutr.* 59 (2019) 1408-1432.
- [3] D.C.L.L. Domingues, D.S.L.F. Gomes, M. Nitz, *Chem. Ind. Chem. Eng. Q.* 25 (2019) 229-237.
- [4] D. Tiroutchelvame, V. Sivakumar, P.J. Maran, *Chem. Ind. Chem. Eng. Q.* 21 (2015) 547-559.
- [5] G. Adiletta, P. Russo, W. Senadeera, M.D. Matteo, *J. Food Eng.* 172 (2015) 9-18.
- [6] C. Srinivasakannan, N. Balasubramanian, *Adv. Powder Technol.* 20 (2009) 390-394.
- [7] W. Senadeera, B.R. Bhandari, G. Young, B. Wijesinghe, *J. Food Eng.* 58 (2003) 277-283.
- [8] N. Parlak, *Heat Mass Transfer.* 51 (2015) 1085-1095.
- [9] J.E. Vásquez-Parra, C.I. Ochoa-Martínez, M. Bustos-Parra, *J. Food Eng.* 119 (2013) 648-654.
- [10] J. Carranza-Concha, M. Benlloch, M.M. Camacho, N. Martínez-Navarrete, *Food Bioprod. Process.* 90 (2012)

- 243-248.
- [11] M.H. Jazini, M.S. Hatamipour, *Food Bioprod. Process.* 88 (2010) 133-137.
- [12] L. Cinquanta, M. Di Matteo, M. Estia, *Food Chem.* 79 (2002) 233-238.
- [13] M. Di Matteo, L. Cinquanta, G. Galiero, S. Crescitelli, *Food Chem.* 79 (2002) 227-232.
- [14] P.P. Lewicki, *Trends Food Sci. Technol.* 17 (2006) 153-163.
- [15] AOAC (Association of Official Analytical Chemists), *Official Methods of Analysis of AOAC International*, 16th ed., AOAC International, Rockville, MD, 1995.
- [16] M. Beigi, *Chem. Ind. Chem. Eng. Q.* 23 (2017) 431-440.
- [17] A.S. Kipcak, İ. Doymaz, E. Moroydor-Derun, *Chem. Ind. Chem. Eng. Q.* 25 (2019) 1-10.
- [18] J.R. De Jesus Junqueira, J.L.G. Corrêa, H.M. De Oliveira, R.I.S. Avelar, L.A.S. Pio, *LWT--Food Sci. Technol.* 82 (2017) 404-410.
- [19] A. Saxena, T. Maity, P.S. Raju, A.S. Bawa, *Food Bioprod. Process.* 95 (2015) 106-117.
- [20] B. Hiranvarachat, S. Devahastin, N. Chiewchan, *Food Bioprod. Process.* 89 (2011) 116-127.
- [21] N. Therdthai, W. Zhou, *J. Food Eng.* 91 (2009) 482-489.
- [22] G. Ergunes, S. Tarhan, *J. Food Eng.* 76 (2006) 446-452.
- [23] T.K. Lim, *Solanum torvum*, in *Edible Medicinal And Non-Medicinal Plants*, Springer Dordrecht (2013) 429-441.
- [24] H. Schwartz, V. Ollilainen, V. Piironen, A.M. Lampi, *J. Food Compos. Anal.* 21 (2008) 152-161.
- [25] C.I.G. Tuberoso, A. Kowalczyk, E. Sarritzu, P. Cabras, *Food Chem.* 103 (2007) 1494-1501.

R. BARATHIRAJA <sup>1</sup>  
 P. THIRUMAL <sup>1</sup>  
 G. SARASWATHY <sup>2</sup>  
 I. RAHAMATHULLAH <sup>3</sup>

<sup>1</sup> Department of Mechanical Engineering, Government College of Engineering, Bargur, India

<sup>2</sup> Department of Chemistry, Government College of Engineering, Bargur, India

<sup>3</sup> Department of Mechanical Engineering, Government College of Engineering, Srirangam, Tiruchirapalli, India

## EFEKTI PRETHODNIH OBRADA NA SUŠENJE BOBICA GRAŠKA PATLIDŽANA (*SOLANUM TORVUM*) U SUŠARI SA FLUIDIZOVANIM SLOJEM

*Utjecaj metoda prethodne obrade, kao što su fizički, hemijski, kombinovani fizički i hibridni postupci na bobice graška patlidžana (*Solanum torvum*) na poboljšanje difuzije vode tokom sušenja je procenjen zbog uklanjanja voštanog sloja na kori. Prethodno obrađeni i neobrađeni uzorci su sušeni na temperaturi od 70 °C i protoku vazduha od 4 m/s u sušari sa fluidizovanim slojem. Bobice koje su prethodno tretirane kombinovano abrazijom i blanširanjem imaju najkraće vreme sušenja i dobro očuvanje sadržaja vitamina C od 36%. Najveće vrednosti brzine sušenja od 0,396 kg vode/kg min, maksimalne efektivne difuzivnosti vlage od  $6,002 \times 10^{-10} \text{ m}^2/\text{s}$  i koeficijenta zapreminskog skupljanja od 0,68 imaju bobice tretirane kombinovanom fizičkom postupku. Maksimalne promene boje  $\Delta E = 14,75$  i Chroma  $\Delta C = -10,53$  uočene su kod neobrađenih uzoraka.*

*Ključne reči: boja, efikasna difuzija vlage, prethodna obrada, skupljanje, bobice graška patlidžana.*

NAUČNI RAD

ALEX LEANDRO ANDRADE  
DE LUCENA  
RAYANY MAGALI DA ROCHA  
SANTANA  
MARCOS ANDRÉ SOARES  
DE OLIVEIRA  
LUCIANO COSTA ALMEIDA  
MARTA MARIA MENEZES  
BEZERRA DUARTE  
DANIELLA CARLA  
NAPOLEÃO

Chemical Engineering  
Department Federal University of  
Pernambuco, Recife, Brazil

SCIENTIFIC PAPER

UDC 615.2:502:66:543.544

## EVALUATION OF COMBINED RADIATION FOR THE TREATMENT OF LAMIVUDINE AND ZIDOVUDINE VIA AOP

### Article Highlights

- Use of advanced oxidation processes to degrade antiretrovirals applying combined irradiation
- Degradation of the pharmaceuticals lamivudine and zidovudine in a synthetic effluent
- Degradation of 90.53% for photoperoxidation and 89.32% for photo-Fenton in aqueous drug mixture
- Degradation of 88.69% for photoperoxidation and 85.79% for photo-Fenton in synthetic mixture
- Toxicity tests for the drugs, after submissions to the AOP, in both studied media

### Abstract

*The presence of pharmaceutical contaminants in nature is an environmental problem generating increasing concerns. Due to this, it is necessary to evaluate treatments capable of degrading these contaminants, such as the advanced oxidation processes (AOPs). In this work, the photoperoxidation and photo-Fenton AOP were applied to degrade a mixture of lamivudine and zidovudine in an aqueous medium and synthetic effluent (SE). To this end, a bench reactor (UV-C; UV-A and sunlight irradiations) was built. The AOP treatments efficiency was evaluated by ultraviolet/visible spectrophotometry. The tests involved the application of the irradiations individually and combined. The best operational conditions were  $[H_2O_2]$  of  $600 \text{ mg L}^{-1}$  and  $[Fe]$  of  $0.5 \text{ mg L}^{-1}$ , for both matrices, with degradations of 90.53% and 89.32% for the photoperoxidation and photo-Fenton processes in aqueous media and 88.69% and 85.79% in SE. Kinetic studies showed a good fit for two pseudo-first-order models with  $R^2 > 0.93$ . Toxicity tests involving the application of lettuce, carrot, and tomato seeds showed an inhibition for the three seeds when submitted to solutions after treatment, for both matrices, this fact is corroborated by the HPLC analysis, in which the formation of small peaks was verified, suggestive of the formation of by-products. Thus, it can be affirmed that both photo-Fenton and photoperoxidation processes efficiently degrade the drug mixture when applying UV-C radiation.*

*Keywords: chromatography, drugs, kinetic modeling, synthetic effluent, toxicity.*

The pharmaceuticals comprise a large group of active medicinal products, used for personal health or aesthetics, to evoke biological or physiological

responses in the target of use, indispensable for living beings' health [1,2]. Among the various classes of pharmaceuticals, products are the antiretrovirals, which are used to treat diseases such as influenza, herpes, hepatitis, and, in particular, the human immunodeficiency virus (HIV) [3,4]. Due to their efficiency in treating HIV, the use and application of antiretrovirals have grown rapidly worldwide, with many of them being considered essential by the world health organization (WHO) [5,6].

Correspondence: D.C. Napoleão, Chemical Engineering Department Federal University of Pernambuco, Av. Prof. Arthur de Sá, s/n, 50740-521, Recife - PE - Brazil.  
E-mail: [daniella.napoleao@ufpe.br](mailto:daniella.napoleao@ufpe.br)  
Paper received: 9 March, 2021  
Paper revised: 16 July, 2021  
Paper accepted: 17 August, 2021

<https://doi.org/10.2298/CICEQ210309029L>

In the class of antiretrovirals, the following ones

stand out as the most commonly used: abacavir, nevirapine, stavudine, lamivudine (3TC), and zidovudine (AZT). The latter two are usually combined therapy to treat acquired immunodeficiency syndrome (AIDS) [7,8].

The increasing use of antiretrovirals drugs has generated an environmental concern. Without completely metabolizing the body, these substances are excreted via urine and feces, following the sewage collection network to the wastewater treatment plants (WWTPs) [3,8]. In these, the conventional physical-chemical and biological treatments are not efficient for completely degrading pharmaceutical contaminants, meaning that part of them can reach nature. This concern covers WWTPs related to domestic and industrial effluents [9].

As a consequence, there is an increasingly common identification and presence of drugs such as lamivudine and zidovudine in nature, with the majority of cases being identified in the African continent [8-12] and some in Europe [13-15], showing the scope of this type of contamination. This indicates that such substances may be present in countries that commonly use these drugs to treat diseases but have not yet identified or studied this type of problem in depth.

Knowing this, it is necessary to evaluate the efficiency of other treatments that act as an alternative or addition to the conventional processes, making it possible to degrade these contaminants efficiently [16,17] completely. The advanced oxidation processes (AOPs) are among alternative treatments, which can completely degrade organic contaminants, oxidizing them to non-toxic, smaller molecules or mineralizing to water, carbon dioxide, and mineral salts [18-20].

Different types of AOPs have been used to treat water and effluents, deserving of their investigation, capacity, and efficiency in the degradation of pharmaceuticals contaminants, the photoperoxidation, and photo-Fenton processes [8,21,22]. The photoperoxidation consists of a combination of solar or ultraviolet (UV) radiation with hydrogen peroxide (H<sub>2</sub>O<sub>2</sub>) to promote the formation of hydroxyl radicals (OH•). These are highly reactive and capable of degrading complex organic pollutants [23,24]. While the photo-Fenton process involves the reaction between (Fe<sup>2+</sup>/H<sub>2</sub>O<sub>2</sub>) and (Fe<sup>3+</sup>/H<sub>2</sub>O<sub>2</sub>) for the formation of hydroxyl radicals, in the presence of visible or UV radiation, with iron acting as a catalyst [25-26].

Several studies have suggested and proved the applicability of these two AOP as an effective tertiary treatment for the degradation of different classes of pharmaceutical contaminants [27-29]. These studies are important since drugs that resist the treatment

present on WWTPs have been identified in other aquatic bodies. This fact can be evidenced by the average removal of lamivudine and zidovudine in wastewater treatment plants, which respectively reach values of the order of 76% and 68% [8,30].

When working with (AOPs) to degrade different types of organic contaminants, some steps are essential: to evaluate the parameters involved, the controlling kinetics of the process, and analyze the toxicity [31]. The degradation kinetics of organic contaminants by AOP can be described, in general, by rate expressions of pseudo-first-order, as according to Eq. (1) [32,33]:

$$-\ln \frac{c}{c_0} = k \cdot t \quad (1)$$

where  $c$  is the concentration in a specific time,  $c_0$  is the initial concentration,  $k$  is the rate constant of the system under study, and  $t$  is the reaction time.

The toxicity assessment is also important, considering that the intermediates and products formed in the degradation process can be more biologically active and, consequently, more toxic than the original compounds. Thus, evaluating the response of different organisms is crucial after applying AOPs as a treatment [34].

However, despite the above, studies on the removal of the pharmaceuticals lamivudine and zidovudine using AOP are still rare when compared to other classes of drugs [14,35]. Thus, this work aims to treat a mixture of the drugs lamivudine and zidovudine using the photoperoxidation and photo-Fenton processes, started by Lucena *et al.* [36], including a new analysis of the efficiency of the AOP not only in an aqueous medium but also, in synthetic effluent, besides evaluating the efficiency of the AOP when combined radiation is applied. To this end, kinetic studies were carried out to assess the suitability of the pseudo-first-order kinetic models to the concentration and degradation data of the drugs under investigation. Complementing the study, the efficacy of the process applied to the degradation of the drugs was investigated through a toxicity test using seeds of *Lactuca sativa* (lettuce), *Daucus carota* (carrot), and *Solanum lycopersicum* (tomato). Finally, chromatographic analysis evaluated the formation of by-products to understand better the results obtained after the submission of drugs to AOP treatments. The drugs and zidovudine are produced by the Laboratório Farmacêutico de Pernambuco (Pharmaceutical Laboratory of Pernambuco - LAFEPE), located near the Federal University of Pernambuco (UFPE), and a stream that is used as a receiving body for the effluents treated by both LAFEPE and UFPE. Allied to this, the



study by Funke *et al.* [14] indicates the resistance of these two drugs to conventional effluent treatments.

## MATERIALS AND METHODS

### Identification/quantification of the pharmaceuticals and preparation of the working solutions

The active principles of lamivudine (3TC) and zidovudine (AZT) were provided by LAPEFE with batch numbers 17933 and 17925, respectively. Both with a purity degree > 99%. The physicochemical properties of both drugs, such as molecular formula, weight, solubility in water,  $pK_a$ , and  $\log K_{now}$ , are given in Supplementary Table 1.

A stock solution containing  $1000 \text{ mg L}^{-1}$  of the mixture of drugs 3TC and AZT was prepared using distilled water and methanol (Merck brand) in a volumetric ratio of 9:1. The work solutions used were prepared by diluting the stock solution in water. These solutions were analyzed using an ultraviolet/visible (UV/Vis) spectrophotometer (Thermoscientific) at a maximum absorbance wavelength ( $\lambda$ ) of 269 nm. For quantification, was used, an analytical curve with a linear range from 1 to  $30 \text{ mg L}^{-1}$ , correlation coefficient > 0.99, variance coefficient of 1.43%, and limits of detection (LOD) and quantification (LOQ) equals  $0.77 \text{ mg L}^{-1}$  and  $2.34 \text{ mg L}^{-1}$ , respectively.

The synthetic effluent (SE) was composed of inorganic salts and other organic compounds, as described elsewhere [37, 38]. The components present in the SE and their respective concentrations are described in Table 1.

Table 1. Components and their concentrations in the synthetic effluent

Components	Concentration ( $\text{mg}\cdot\text{L}^{-1}$ )
Lamivudine	15
Zidovudine	15
Sucrose	25
Glucose	15
Urea	20
Ammonium phosphate	20
Sodium sulfate	25
Sodium chloride	25
Sodium carbonate	25
Sodium acetate	20
Magnesium carbonate	25
Potassium nitrate	10

### Bench reactor configuration

The degradation tests were performed comparing the efficiency of the AOPs of photoperoxidation ( $\text{UV}/\text{H}_2\text{O}^{2-}$ ) and photo-Fenton ( $\text{H}_2\text{O}_2/\text{Fe}^{2+}/\text{UV}$ ) in addition to the photolysis process. For this purpose, a bench photolytic reactor equipped with lamps emitting three types of radiation (UV-C, UV-A, and Sunlight) was used, as shown in Figure 1.

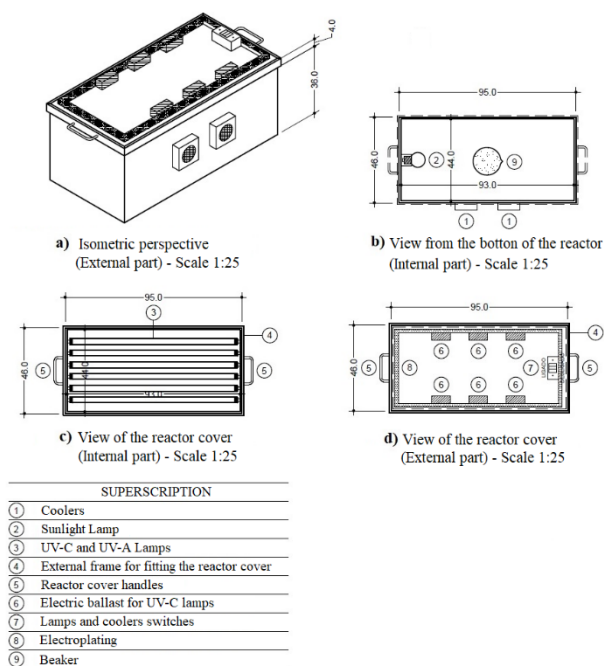


Figure 1. Bench-top photolytic reactor with combined radiation, general views, and isometric perspective. Measures in centimeters.

As can be seen in Figure 1, the reactor is equipped with three UV-C germicidal fluorescent tube lamps (Osram brand) of 30 W, three UV-A tube lamps (Tovalight brand) of 20 W, these two types installed interchangeably on the cover, and a 300 W sunlight lamp (Osram brand). When evaluated separately through radiometers (Emporionet), the radiations from these lamps had photon emission of respectively  $3.32 \cdot 10^3 \text{ W cm}^{-2}$ ,  $1.39 \cdot 10^3 \text{ W cm}^{-2}$ , and  $1.58 \cdot 10^5 \text{ W cm}^{-2}$ . In addition to the lamps, two coolers (Darkforce) were installed in the reactor to assist in cooling and temperature control. The photoreactor was coated internally with aluminum foil to increase its efficiency as according to Khan; Tahir [39].

### Bench reactor cost analysis

A cost analysis for the assembly and operation of the reactor was also carried out. The costs were divided into 3 types: Project, materials, and operational. In the project costs, technical drawings were outlined, such as

general views and perspectives and the values associated with the construction of the reactor structure and the installation of lamps and electrical parts. The material costs were considered expenses with lamps, electrical ballasts, coolers, and electrical material such as wires and switches. At the same time, the operational cost was calculated based on the kW-h price of US\$ 0.166 for B3 units of the classification from the Companhia Energética de Pernambuco/Brazil (CELPE), which includes the Federal University of Pernambuco, where the research was developed [40]. Thus, it was taken into account the operational time of the reactor and the power of the lamps and coolers installed.

### Degradation of the drugs using AOPs

To perform the preliminary tests (in triplicate), beakers containing 50 mL of the aqueous mixture of drugs with initial concentrations of 15 mg L<sup>-1</sup> were subjected to treatments for 60 min. In this step, a concentration of hydrogen peroxide ([H<sub>2</sub>O<sub>2</sub>]) (Exodus Científica brand) of 100 mg L<sup>-1</sup> was used; an iron concentration ([Fe]) of 1 mg L<sup>-1</sup> (present as de FeSO<sub>4</sub> 7H<sub>2</sub>O, F Maia Brand) and pH between 5 and 6 adjusted using solutions of H<sub>2</sub>SO<sub>4</sub> and NaOH of 1 mol L<sup>-1</sup> for the photolysis and photoperoxidation processes and between 2 and 3 for the photo-Fenton process. The efficiency of the AOP was determined based on the percentage of drug degradation after UV/Vis spectrophotometry analysis.

Based on the preliminary study results for each of the evaluated AOP, the influence of the operational parameters was assessed in more detail. For this purpose, experiments were carried out, varying the H<sub>2</sub>O<sub>2</sub> concentration from 100 to 900 mg L<sup>-1</sup>. Once the best [H<sub>2</sub>O<sub>2</sub>] was determined, it was fixed, and an analogous study was done for [Fe], between 0.5 and 5.0 mg L<sup>-1</sup>. These tests were performed for an exposure period of 60 min for each irradiation (UV-C, UV-A and sunlight) individually.

After defining the influence of the variables [H<sub>2</sub>O<sub>2</sub>] and [Fe], degradation tests were performed to evaluate the effect of the combination of light irradiations on the efficiency of both AOP under study. For this, 50 mL solution of the drug mixture was used.

The types of combinations used took into account the operation of the lamps, in parallel and series, as shown in Figure 2. All tests exposed the working solution to 60 min for parallel experiments and 120 min for the tests in series, 60 min for each irradiation.

After defining the best operational conditions and evaluating the efficiency of each irradiation, individually and in a combined way, the exposure time

of each process was extended to 90, 120, 150, and 180 min. Then, the distance from the light source to the photoreactor was evaluated in two situations: 1) 36 cm distance to the light source (Low Position) and 12 cm to the light source (High Position).

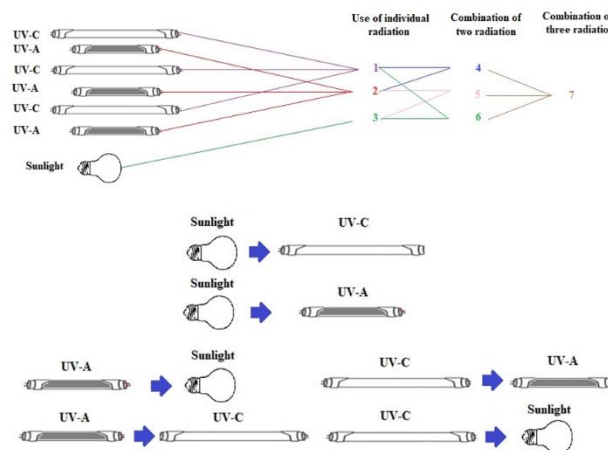


Figure 2. Application of combined irradiation, forms of organization.

### Treatment of the synthetic effluent by AOP

Initially, the synthetic effluent (SE) degradation under study (described in item 2.1) was based on the best experimental conditions optimized for treating the drug aqueous mixture. With the SE being submitted to the photoperoxidation and photo-Fenton AOP. Bearing in mind that the presence of organic compounds and inorganic salts can affect the efficiency of the photo-Fenton process, during the experiments with the SE, the effect of the [Fe] was reevaluated in the same range used for the tests with the aqueous mixture.

The exposure times were 60, 90, 120, 150, and 180 min for both processes, with the study of [Fe] being conducted only for 60 min. Before and after being treated with the AOP, the samples were subjected to a UV-Vis spectrophotometry analysis.

### Kinetic study and modeling

With the best experimental conditions, kinetic monitoring of the photoperoxidation and photo-Fenton AOP was performed, both in aqueous media and in the form of SE. For this purpose, 50 mL of each sample containing 15 mg L<sup>-1</sup> of the pharmaceuticals were irradiated for 180 min, with regular aliquots being analyzed at 5, 10, 15, 20, 30, 45, 60, 75, 90, 120, 150, and 180 min. To not interfere with the analysis result, the aliquots read were returned to the container during the entire process. The experimental data were evaluated for suitability to the pseudo-first-order kinetic models [41,42]. The Chan and Chu model is described

by Eq. (2):

$$c = c_0 \left( 1 - \frac{t}{\rho + \sigma t} \right) \quad (2)$$

where  $c$  is the pharmaceutical concentration ( $\text{mg}\cdot\text{L}^{-1}$ ) after treatment by the AOP at a time  $t$  (min);  $c_0$  is the initial concentration of the pharmaceuticals ( $\text{mg}\cdot\text{L}^{-1}$ ), and the parameters  $1/\sigma$  and  $1/\rho$  symbolize, respectively, the oxidative capacity of the system (dimensionless) and the speed constant of the system ( $\text{min}^{-1}$ ). The values for the parameters  $\sigma$  and  $\rho$  were found based on the linearization of Eq. (2), as expressed in Eq. (3):

$$\frac{t}{\left( 1 - \frac{c}{c_0} \right)} = \rho + \sigma t \quad (3)$$

Another model used to adjust the experimental data was the one proposed by He *et al.* [42], which is based on a simplification of the Langmuir-Hinshelwood model, Eq. (4), to adapt it to a pseudo-first-order equation generating Eq. (5).

$$-\frac{dc}{dt} = \frac{k_r \cdot K \cdot c}{1 + K \cdot c} \quad (4)$$

$$-\frac{dc}{dt} = k_r \cdot K \cdot c = k \cdot c \quad (5)$$

where  $c$  is the pharmaceutical concentration ( $\text{mg}\cdot\text{L}^{-1}$ ) and  $k$  is the pseudo-first-order reaction rate ( $\text{min}^{-1}$ ).

Then, the degradation of the drugs and the formation of by-products were evaluated using a methodology of analysis by high-performance liquid chromatography, using an HPLC/UV (Shimadzu SS-550).

#### Analysis of the drugs lamivudine and zidovudine via HPLC/UV

For this purpose, analytical curves were built in the concentration range from 1 to 30  $\text{mg}\cdot\text{L}^{-1}$  for both drugs, with detection and quantification limits, respectively of 0.36  $\text{mg}\cdot\text{L}^{-1}$  and 1.10  $\text{mg}\cdot\text{L}^{-1}$  for lamivudine and 0.41  $\text{mg}\cdot\text{L}^{-1}$  and 1.25  $\text{mg}\cdot\text{L}^{-1}$  for zidovudine. The chromatographic system consisted of a mobile phase with acetonitrile and water acidified with 0.1% acetic acid (65:35 v/v) and an ultra C18 Column (5  $\mu\text{m}$ ; 4.6 x 250 mm) operating in reverse with isocratic elution.

The equipment is composed of a UV detector, with analysis at 255 nm (zidovudine) and 277 nm (lamivudine). The system flow was fixed at 0.7  $\text{mL}\cdot\text{min}^{-1}$ , with an oven temperature of  $40 \pm 1$   $^{\circ}\text{C}$  and a pressure of 90  $\text{kg}\cdot\text{cm}^{-2}$ . The injection volume used was equal to 5  $\mu\text{L}$ , and the retention time varied between

5.0 min to 5.7 min for lamivudine and 5.8 min to 6.5 min for the zidovudine. To ensure the efficiency of the chromatographic analysis, the samples before and after submission to treatment via AOP were submitted to a preparation step using polymeric cartridges of the Strata X type (Phenomenex - 500  $\text{mg}/6$  mL) to perform a solid-liquid extraction (ESL). The operational mode was the reverse type, following the methodology described by Napoleão *et al.* [43]

#### Kinetic study and modeling

Toxicity tests were performed by applying seeds, using the following species *Lactuca sativa* (lettuce), *Daucus carota* (carrot), and *Solanum lycopersicum* (tomato). These were exposed to solutions with the pharmaceuticals contaminants before and after being treated by the photoperoxidation and photo-Fenton processes. The toxicity assessment followed the methodology described by Santos *et al.* [44].

Distilled water and a boric acid solution at 3% were used as negative and positive controls, respectively. Petri dishes were kept in an environment in the absence of light at  $25 \pm 1$   $^{\circ}\text{C}$  for a period of 120 h. Finally, the quantities of germinated seeds and the root growth were verified and used to calculate the relative growth index (RGI) and the germination index (GI) as according to Equations 6 and 7 [45].

$$RGI = \frac{CRA}{CRC} \quad (6)$$

$$GI = RGI \frac{SGA}{SGC} \quad (7)$$

where  $CRC$  is the total length of the root in the negative control,  $CRA$  is the total length of the root in the sample,  $SGC$  is the number of seeds germinated in the negative control, and  $SGA$  is the number of seeds germinated in the sample.

## RESULTS AND DISCUSSION

#### Bench-top photolytic reactor with combined radiation - Associated costs

As mentioned in the methodology, the costs related to the construction and operation of the reactor were divided into 3 types, with the total cost of the reactor project estimated at US\$120.00, US\$40.00 related to the technical design, US\$60.00 for the construction of the reactor structure and \$20.00 for labor (installation and startup). The costs related to the acquisition of materials for the bench photolytic reactor are shown in Table 2.

The sum of the project and material costs totaled US\$479.92 (Table 2). On the other hand, operating

costs were calculated individually for each lamp present, considering its operation per hour and the relative kWh value in Recife. The values associated with these costs are shown in Table 3.

Analyzing Table 3, the approximate operating

cost, calculated, per hour of operation was US\$0.07649, taking into account all the lamps and the two coolers in operation, that is, in the condition of maximum expenditure.

Table 2. The benchtop photolytic reactor's construction and operating costs with combined radiation

Material	Unitary value (US\$)	Units	Total Value (US\$)
Germicidal ultraviolet tubular lamp (UV-C) - Osram Puritec - 30 W	23.85	3	71.55
Black light fluorescent lamp (UV-A) - Starlux - 20 W	13.69	3	41,07
Sunlight lamp - Osram - 300 W	84.81	1	84.81
Electric ballast for fluorescent lamp 20 W	9.00	3	27.00
Electric ballast for fluorescent lamp 32W	13.14	3	39.42
Electric material	26.32	1	26.32
Wood to build the reactor - plywood, glue, screw, others	41.20	1	41.20
Cooler Fan - Dark Force	8.10	2	16.20
Utilities	12.35	1	12.35
<b>Total Material Costs</b>			<b>359,92</b>

\* Values for January 2019.

Table 3. Operating costs for the benchtop photolytic reactor with combined radiation from March 2019 to April 2020

Item	Individual power (W·h)	Units	Power (kW·h)	Individual cost (US\$/h)
Germicidal ultraviolet tubular lamp (UV-C) - Osram Puritec - 30 W	30	3	0.09	0.015
Black light fluorescent lamp (UV-A) - Starlux - 20 W	20	3	0.060	0.010
Sunlight lamp - Osram - 300 W	300	1	0.3	0.051
Cooler Fan - Dark Force	1,44	2	0.00288	0.00049
Germicidal ultraviolet tubular lamp (UV-C) - Osram Puritec - 30 W	30	3	0.09	0.015
<b>Total</b>				<b>0.07649</b>

### Drugs treatment using AOPs - aqueous mixture

The preliminary tests indicated no degradation of the aqueous mixture of the drugs under study when using the photolysis process, applying the irradiations individually. A similar result was observed when using the AOP with UV-A and sunlight irradiations separately. On the other hand, the photoperoxidation and photo-Fenton processes associated with UV-C irradiation showed photodegradation results of  $17.76 \pm 0.21\%$  and  $8.27 \pm 0.05\%$ , respectively, after 60 min of treatment.

Thus, studies on the concentrations of hydrogen peroxide [ $\text{H}_2\text{O}_2$ ] and iron [Fe] were conducted to increase the degradation capacity of AOPs using UV-C irradiation. The data obtained for the isolated study of these variables are shown in Figure 3.

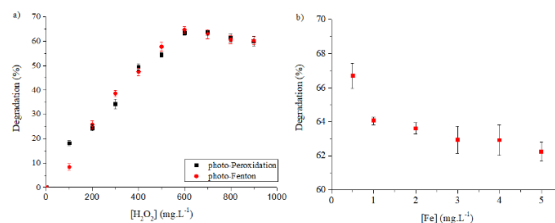


Figure 3. Influence of  $\text{H}_2\text{O}_2$  and Fe concentrations on the degradation of the aqueous mixture of the drugs lamivudine and zidovudine by the photoperoxidation and photo-Fenton processes with 60 min of treatment, the study of the variation of a) [ $\text{H}_2\text{O}_2$ ] ( $[\text{Fe}] = 0,5 \text{ mg}\cdot\text{L}^{-1}$ ) and b) [ $\text{Fe}$ ] ( $[\text{H}_2\text{O}_2] = 600 \text{ mg}\cdot\text{L}^{-1}$ ).

From Figure 3a, it is observed that for [ $\text{H}_2\text{O}_2$ ] above  $600 \text{ mg}\cdot\text{L}^{-1}$ , both studied processes lost

efficiency. This happens due to the non-selectivity of the  $\text{H}_2\text{O}_2$  as a reagent and that when in excess, this oxidant can react in parallel with the hydroxyl radicals present in the solution. Thus, the formation of other radicals occurs, such as superoxide's, which are much weaker than hydroxyl; that is, they present lower potential reduction patterns [45,46]. Thus, it can be said that among the analyzed  $[\text{H}_2\text{O}_2]$ ,  $600 \text{ mg L}^{-1}$  is the limiting factor for both evaluated processes.

When evaluating Figure 3b, the increase in iron concentration does not improve the efficiency of the photo-Fenton process for degradation of the aqueous mixture of drugs 3TC and AZT. This figure clearly shows that  $[\text{Fe}] 0.5 \text{ mg L}^{-1}$  led to further degradation. This indicates that the increase in iron in this process can act similarly to the excess of the oxidizing agent. Thus, there is an excessive release of hydroxyl radicals leading to the formation of other less desirable radicals, such as superoxide [47,48,49].

Then, the effect of applying the combined irradiation for both processes was evaluated. For these tests, degradation values in the range of 55 to 60% were verified only for combinations involving the presence of UV-C radiation, either in parallel or in series. So that there were no improvements in the yield of advanced oxidative processes for degradation of the mixture of drugs under study when applying the combined radiation. Thus, UV-C radiation individually was considered in all subsequent tests. Having determined the radiation to be employed, the effect of the distance from the irradiation source of the photocatalytic reactor to the mixture of drugs was evaluated. The results of this analysis are shown in Table 4.

Table 4. Effects of time and distance to light on the degradation of the aqueous mixture of lamivudine and zidovudine ( $15 \text{ mg}\cdot\text{L}^{-1}$ )

Time (min)	Photoperoxidation		Photo-Fenton	
	Degradation (%)			
	Low position	High position	Low position	High position
60	62.73	78.40	66.69	83.43
90	78.46	84.82	78.88	85.59
120	86.70	88.63	86.71	86.55
150	88.56	89.66	86.97	88.18
180	90.13	90.53	87.58	89.32

\*Low position - 36 cm of distance to the light source; High position - 12 cm of distance to the light source.

Table 4 shows that the HIGH position favors the yield of both studied AOP during the first 90 min of the

process. However, after 180 min of treatment, there is no significant difference between the results obtained for the two positions, HIGH and LOW, with the degradation stabilizing in the range of 87 to 90%.

This behavior is explained by the design of photolytic reactors, aiming to ensure that all light emitted during the process remains inside the reactor. Therefore, the distance from the irradiation source (lamp) can be ignored. For this, reflective surfaces ensure that the real distance traveled by the light inside the reactor is greater than its physical dimensions [50]. In the present study, this observation was guaranteed by coating the reactor with aluminum foil.

Given the above and considering that the two positions studied stabilized in the same range of degradation in both processes, the amount of light absorbed by the organic substrate (drugs under the study) is similar, according to Crittenden *et al.* [50]. Thus, regardless of the position of the system in the reactor, there is no difference between the situations studied after stabilizing the process. This allows the use of the HIGH position as a standard for subsequent steps. Then, the efficiency of the photoperoxidation and photo-Fenton processes was evaluated to degrade the synthetic effluent.

#### Drugs treatment using AOPs - synthetic effluent

The treatment of the mixture of drugs in a medium consisting of synthetic effluent was carried out using the best experimental/operational conditions found for the aqueous mixture for both AOP. Therefore,  $600 \text{ mg L}^{-1}$  of  $[\text{H}_2\text{O}_2]$  and  $0.5 \text{ mg L}^{-1}$  of  $[\text{Fe}]$  were used, with the reactor fixed in the high position and the application of UV-C irradiation alone. The results obtained for these tests are shown in Table 5.

Table 5. Degradation of the synthetic effluent of the drugs lamivudine and zidovudine ( $15 \text{ mg}\cdot\text{L}^{-1}$  each) during 180 min of treatment under the photoperoxidation and photo-Fenton processes

Time (min)	Photoperoxidation	Photo-Fenton
	Degradation (%)	
60	64.96	81.49
90	71.25	83.09
120	84.57	84.42
150	86.06	84.99
180	88.69	85.79

Observing Table 5, it is clear that the mixture of drugs 3TC and AZT in synthetic effluent is more

to the photo-Fenton process in the first 90 min of treatment, with a difference of 11.84% in degradation when compared to the photoperoxidation process. However, both processes stabilize in the same range of degradation, between 85.79 and 88.69%. This fact was observed after 180 min of treatment, with no significant difference between both efficiencies.

The effect of  $[Fe]$  was reevaluated for the synthetic effluent, considering that the presence of inorganic salts and organic compounds in the studied matrix can impact the production of hydroxyl radicals according to Gil; Galeano; Vicente, [25]. The results for this analysis are shown in Figure 4.

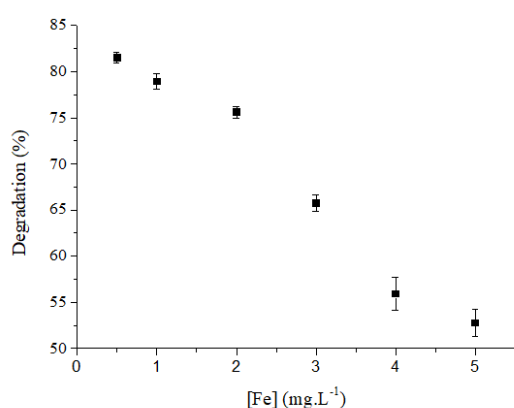


Figure 4. Influence of  $[Fe]$  on the degradation of a synthetic effluent containing lamivudine and zidovudine by the photo-Fenton process with 60 min of treatment

From Figure 4, it is evident that just like in the aqueous medium, the  $[Fe]$  that leads to the highest degradation efficiency was  $0.5 \text{ mg L}^{-1}$ . It is also possible to observe a more pronounced drop in the efficiency of the photo-Fenton by increasing the  $[Fe]$  in the treatment of the synthetic effluent. This fact must be related to the sum of the effects of excess iron with the action of inorganic salts and organic compounds, decreasing the production of hydroxyl radicals.

### Kinetic study

Proving the efficiency of AOP for degradation of the mixture of drugs in both matrices studied, the reaction kinetics of these processes was evaluated. The kinetic study employed the following experimental conditions, for both processes  $[H_2O_2]$  of  $600 \text{ mg L}^{-1}$ ,  $[Fe]$  of  $0.5 \text{ mg L}^{-1}$ , drug concentration of  $15 \text{ mg L}^{-1}$ , isolated application of UV-C irradiation, and the reactor in the HIGH operating position, with the kinetic monitoring performed for 180 min. From the data obtained in this study, the pseudo-first-order kinetic models developed by Chan and Chu [41] and

He *et al.* [42] and the adequacy between them and the experimental data were evaluated. These results are shown in Figure 5.

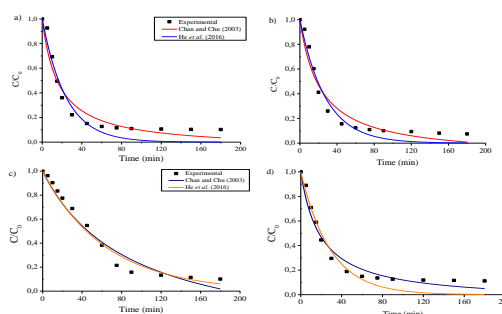


Figure 5. Adjustment to the models proposed by Chan and Chu [41] and He *et al.* [42] for the processes of a) photoperoxidation and b) photo-Fenton in aqueous medium and c) photoperoxidation and d) photo-Fenton in synthetic effluent. Conditions:  $[H_2O_2] = 600 \text{ mg L}^{-1}$ ,  $[Fe] = 0,5 \text{ mg L}^{-1}$ , drug concentration =  $15 \text{ mg L}^{-1}$ .

From Figure 5, it is observed that the degradation of the drugs in aqueous and synthetic media occurs more accentuated in the first 60 min of the process, stabilizing after 180 min, for both AOPs. The data of the obtained kinetic parameters are shown in Table 6.

Analyzing Table 6, it is observed that both models fit satisfactorily to the experimental data since the linear regression coefficients ( $R^2$ ) are greater than 0.93. When comparing the models to each other, it can be seen that the model by Chan and Chu [41] presents a better fit in three of the four cases presented, with the model by He *et al.* [42] adapting better only to photoperoxidation in synthetic effluent.

There is also a higher rate of degradation ( $\text{min}^{-1}$ ) for the photo-Fenton process in both matrices studied. This fact is evidenced by the greatest degradations obtained in the first 90 min of this treatment. On the other hand, there is no significant difference in the oxidative capacity between the studied processes, considering that both stabilize in a similar range of degradation % after 180 min of treatment.

Another way to demonstrate that the kinetic models of Chan and Chu [41] and He *et al.* [42] satisfactorily represent the degradation processes of the drugs lamivudine and zidovudine with the studied AOPs is to analyze the residual fraction of the drug mixture as a function of time and compare the data obtained experimentally with those predicted by the models, as shown in Figure 6.

The comparison between the experimental data

Table 6. Parameters for the kinetic models of Chan and Chu [41] and He *et al.* [42] for the degradation of the mixture of the drugs lamivudine and zidovudine by the photoperoxidation and photo-Fenton processes in aqueous and synthetic media

Process	Medium	Degradation (%) after 180 min	Chan and Chu [41] model			He <i>et al.</i> [42] model	
			$1/\rho$ (min <sup>-1</sup> )	$1/\sigma$	$R^2$	$K$ (min <sup>-1</sup> )	$R^2$
Photoperoxidation	aqueous	92.5	0.077	1.007	0.95	0.043	0.93
Photo-Fenton		89.8	0.088	0.972	0.95	0.052	0.94
Photoperoxidation	synthetic	89.9	0.022	1.090	0.94	0.016	0.97
Photo-Fenton		88.8	0.050	1.029	0.98	0.035	0.97

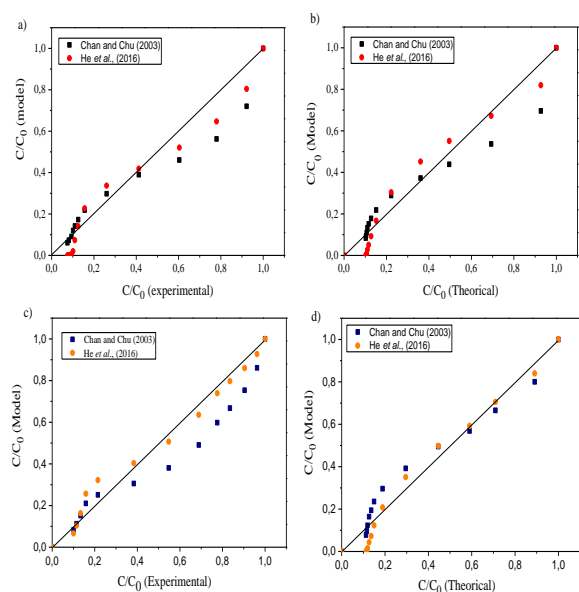


Figure 6. Comparison of the values of experimental residual concentration and the ones predicted by the models of Chan and Chu [41] and He *et al.* [42] for the processes of a) photoperoxidation and b) photo-Fenton in aqueous medium and c) photoperoxidation and d) photo-Fenton in synthetic effluent. Conditions:  $[H_2O_2] = 600 \text{ mg}\cdot\text{L}^{-1}$ ,  $[Fe] = 0,5 \text{ mg}\cdot\text{L}^{-1}$ , drug concentration =  $15 \text{ mg}\cdot\text{L}^{-1}$ .

and the models shown in Figure 6 confirms that the pseudo-first-order kinetic models proposed by Chan and Chu [41] and He *et al.* [42] satisfactorily describe the experimental results found in the treatment of drugs by AOPs in both aqueous media and in the synthetic effluent. Bearing in mind that the closer the experimental values are to the first bisector shown in the graphs, the better their help to the proposed models. This indicates that the trend of degradation for the lamivudine and zidovudine drugs follows the expected behavior for the treatment of pharmaceuticals via AOPs, that is, a fast first step (60 min) responsible for the degradation of 90.31% of lamivudine and 85.31% of zidovudine under the photoperoxidation process and 87.67% of lamivudine and 85.93% of zidovudine under the photo-Fenton process, followed by a slow step, which for this study

stabilized at 180 min.

The samples were then evaluated on the HPLC to verify the degradation of both drugs under AOP treatment in the two matrices applied, aqueous mixtures and synthetic effluent. The chromatograms for these analyzes are shown in Figure 7.

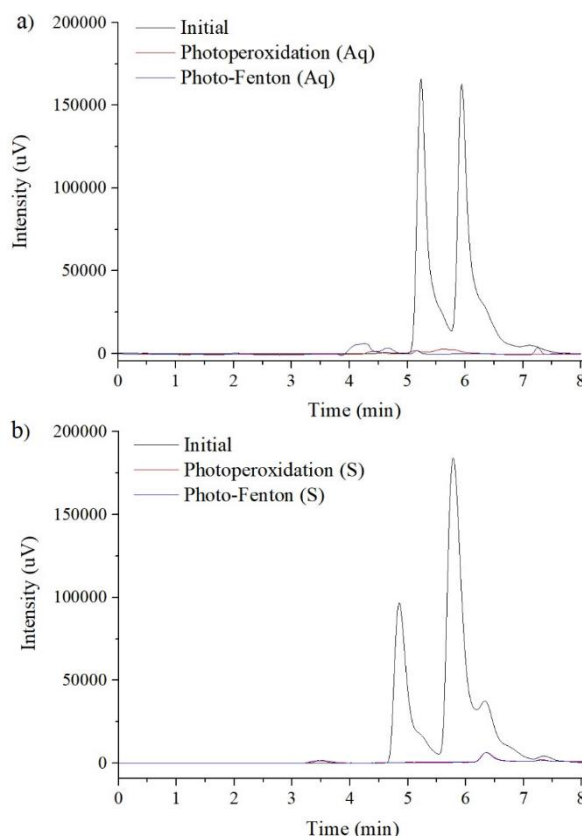


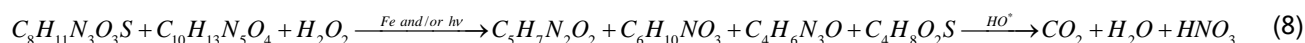
Figure 7. Chromatograms before and after applying the photoperoxidation and photo-Fenton processes for a) the aqueous solution of lamivudine and zidovudine and b) synthetic effluent.

From Figure 7, it was verified that both treatments (photoperoxidation and photo-Fenton) completely degrade the studied drugs on both matrices. However, it is possible to observe the presence and formation of three small peaks in the

retention times of 4.0 to 4.4 min, 4.5 to 4.7 min, and from 7.1 to 7.4 min after the photo-Fenton treatment. While for the synthetic effluent analysis, two small peaks were identified, at the retention times of 3.2 to 3.8 min, for the photoperoxidation processes and from 6.3 to 6.6 min for both AOP processes.

After evaluating the degradation efficiency for the two pharmaceuticals studied, lamivudine and zidovudine, in both applied matrices, a residual peroxide analysis was carried out following the methodology described by Santana *et al.* [51], with results ranging from 30 mg L<sup>-1</sup> to 60 mg L<sup>-1</sup> for all treatment processes applied.

Although a high degradation efficiency was



## Toxicity

The toxicity tests carried out with seeds of the species *Lactuca sativa* (lettuce), *Daucus carota* (carrot), and *Solanum lycopersicum* (tomato) demonstrated that the application of the positive control resulted in the absence of germination. Data related to germination and root growth for negative control and test solutions (before and after treatment) are shown in Figure 8.

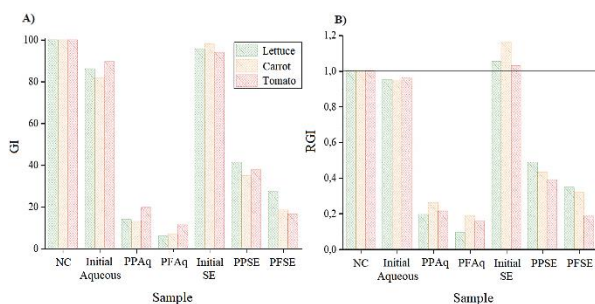


Figure 8. A) Germination index (GI) and B) Relative growth index (ICR) for the seeds of *Lactuca sativa* (lettuce), *Daucus carota* (carrot), and *Solanum lycopersicum* (tomato). \*NC - Negative control; PPAq - Photoperoxidation aqueous; PFAq - Photo-Fenton aqueous; PPSE - Photoperoxidation synthetic effluent; PFSE - Photo-Fenton synthetic effluent.

Figures 8a and b show that the values of GI and RGI obtained for the tests in aqueous and synthetic media show some differences. The values obtained in the latter are higher than their equivalent in aqueous media for all samples analyzed. This behavior can be explained by the richness of nutrients in the prepared synthetic effluent, especially nitrogen, such as potassium nitrate, ammonium phosphate, and urea, an important element of the plant growth cycle in most

obtained for the drug mixture under study, it is known that by treating organic pollutants via AOPs, by-products can be formed during the treatment. Thus, based on literature data [52,53], it is possible to propose the degradation kinetics for the mixture of drugs (Lamivudine - C<sub>8</sub>H<sub>11</sub>N<sub>3</sub>O<sub>3</sub>S and Zidovudine - C<sub>10</sub>H<sub>13</sub>N<sub>5</sub>O<sub>4</sub>) under study, with its probable intermediates, as can be seen in Equation 8.

The presence of by-products and intermediates is an important factor that can affect and influence the toxicity effect of solutions under AOP treatments to different types of organisms. Thus, the application of more detailed assays to evaluate this possible toxicity is required when analyzing the availability of AOPs.

terrestrial ecosystems [54,55].

The RGI values obtained for the photoperoxidation and photo-Fenton processes in both media studied were lower than 0.8 (less than 80% of the relative values for the negative control), indicating inhibition of seed growth according to Young *et al.* [45]. Such behavior was observed for the three seeds studied but not in the initial solutions, which indicated that the intermediates and product formed during the degradation processes might present greater toxicity than the original/initial pharmaceuticals contaminants. This is not unusual behavior. Hillis *et al.* [56] and Papaioannou *et al.* [35] also evaluated the toxicity of pharmaceuticals contaminants against seeds, not finding significant changes in germination and root growth of different species when in contact with solutions without treatment. These results show the need to improve the use of AOPs to obtain a further degraded and non-toxic final solution. Furthermore, it is of fundamental importance to test different organisms, as mentioned by Wang and Wang [57], as some may be more sensitive to certain types of pollutants and by-products formed.

## CONCLUSION

The use of AOP to degrade a mixture of the drugs lamivudine and zidovudine presented the best results in the exclusive presence of UV-C radiation. The combined radiation was not significant for increasing under the optimized operational parameters, the degradation efficiency. After 180 min of treatment, degradations of 90.53% and 89.32%, respectively, for the photoperoxidation and photo-Fenton processes in aqueous medium and 88.69% and 85.79% for the same



processes in synthetic effluent were obtained. The models proposed by Chan and Chu [41] and He *et al.* [42] adjusted appropriately to the concentration data for drugs mixtures,  $R^2$  values greater than 0.93, also, for both matrices, the photo-Fenton process had a higher rate of degradation, with greater decays in the first 90 min of treatment when compared to the photoperoxidation. From ecotoxicity studies with seeds, growth inhibition was verified for the solutions submitted to both processes and matrices, indicating an inhibition of the root growth of the evaluated species. This result also indicates that the intermediates formed during the degradation processes, which were confirmed by the HPLC analysis, may be more toxic than the initial solutions, a behavior similar to that found by some other works in the literature. The results obtained in this work show the efficacy and applicability of the AOPs to degrade a mixture of pharmaceuticals commonly used to control the acquired immunodeficiency syndrome (AIDS), with a satisfactory performance under both matrices applied. But new research is still required to further determine this application, especially in guaranteeing that the final products and by-products formed during those processes are safe and non-toxic to the environment.

### Acknowledgment

To CAPES, FADE/UFPE, NUQAAPE/FACEPE (APQ-0346-1.06/14 process) and to Laboratório Farmacêutico de Pernambuco (Pharmaceutical Laboratory of Pernambuco - LAFEPE).

### REFERENCES

- [1] K. Balakrishna, A. Rath, Y. Praveenkumarreddy, K.S. Guruge, B. Subedi, *Ecotoxicol. Environ. Saf.* 137 (2017) 113-120.
- [2] T. Mackulak, S. Cernanský, M. Fehér, L. Birosová, M. Gál, *Curr. Opin. Environ. Sci. Health* 9 (2019) 40-48.
- [3] H. Zhou, T. Ying, X. Wang, J. Liu, *Sci. Rep.* 6 (2016) 1-10.
- [4] S. Ncube, L.M. Madikizela, L. Chimula, M.M. Nindi, *Water Res.* 145 (2018) 231-247.
- [5] J. Rwagitinywa, A. Sommet, A. Palmaro, J.L. Montastruc, M. Lapeyre-Mestre, *Health Policy* 122 (2018) 237-242.
- [6] World Health Organization (WHO) - Model List of Essential Medicines 21st List (2019). p. 19.
- [7] G. Kumari, R.K. Singh, *HIV AIDS Review* 11 (2012) 5-14.
- [8] D. Russo, A. Siciliano, M. Guida, R. Andreozzi, N.M. Reis, G.L. Puma, R. Marotta, *J. Hazard. Mater.* 349 (2018) 195-204.
- [9] L.M. Madikizela, S. Ncube, L. Chimuka, *J. Environ. Manage.* 253 (2020) 1-11.
- [10] C. Schoeman, M. Dlamini, O.J. Okonkwo, *Emerging Contam.* 3 (2017) 95-106.
- [11] T.T. Mosekiemang, M.A. Stander, A. Villiers, *Chemosphere* 220 (2019) 983-992.
- [12] K.O. K'oreje, M. Okoth, H.V. Langenhove, K. Demeestere, *J. Environ. Manage.* 254 (2020) 109752.
- [13] L. Vergeynst, A. Haeck, P.D. Wispelaere, H.V. Langenhove, K. Demeestere, *Chemosphere* 119 (2015) 52-58.
- [14] J. Funke, C. Prasse, T.A. Ternes, *Water Res.* 98 (2016) 75-83.
- [15] L. Boulard, G. Dierkes, T. Ternes, *J. Chromatogr. A* 1535 (2018) 27-43.
- [16] A. Szymonik, J. Lach, K. Malinska, *Ecol. Chem. Eng.* 24 (2017) 65-85.
- [17] K. Manoli, L.M. Morrison, M.W. Sumarah, G. Nakhla, A.K. Ray, V.K. Sharma, *Water Res.* 148 (2019) 272-280.
- [18] A. Mirzaei, Z. Chen, F. Haghghat, L. Yerushalmi, *Chemosphere* 174 (2017) 665-688.
- [19] S. Ahuja, in *Advances in Water Purification Techniques: Meeting the needs of developed and developing countries*, Elsevier Inc. 1<sup>st</sup> Ed, Netherlands (2019). p. 135-156.
- [20] J. Rodríguez-Chueca, S.V.D. Giustina, J. Rocha, T. Fernandes, C. Pablos, A. Encinas, D. Barcelo, S. Rodríguez-Mozaz, C. M. Manaia, J. Marugán, *Sci. Total Environ.* 652 (2019) 1051-1061.
- [21] G. Lofrano, R. Pedrazzani, G. Libralato, M. Carotenuto, *Curr. Org. Chem.* 21 (2017) 1-14.
- [22] K. Kowalska, G. Maniakova, M. Carotenuto, O. Sacco, V. Vaiano, G. Lofrano, L. Rizzo, *Chemosphere* 238 (2020) 1-8.
- [23] D. Kanakaraju, B.D. Glass, M. Oelgemoller, *J. Environ. Manage.* 219 (2018) 189-207.
- [24] S. Ameta, R. Ameta, in *Advanced Oxidation Processes for Wastewater Treatment*, Academic Press 1st Ed., Elsevier Inc. London (2018) p. 13-46.
- [25] A. Gil, L.A. Galeano, M.A. Vicente, in *Applications of Advanced Oxidation Processes (AOPs) in Drinking Water Treatment*, Vol. 67. Springer. Cham, Switzerland (2019). p. 53-68.
- [26] L. Ling, Y. Liu, D. Pan, W. Lyu, X. Xu, X. Xiang, M. Lyu, L. Zhu, *Chem. Eng. J.* 381 (2020) 122607.
- [27] Y. Yang, Y. Cao, J. Jiang, L. Xinglin, J. Ma, S. Pang, J. Li, Y. Liu, Y. Zhou, C. Guan, *Water Res.* 149 (2019) 543-552.
- [28] W. Qiu, M. Zheng, J. Sun, Y. Tian, M. Fang, Y. Fang, T. Zhang, C. Zheng, *Sci. Total Environ.* 651 (2019) 1457-1468.
- [29] L. Ioannou-Ttofa, S. Raj, H. Prakash, D. Fatta-Kassinos, *Chem. Eng. J.* 355 (2019) 91-102.
- [30] C. Prasse, M.P. Schlusener, R. Schulz, T.A. Ternes, *Environ. Sci. Technol.* 44 (2010) 1728-1735.
- [31] M.I. Stefan, in *Advanced Oxidation Processes for Wastewater Treatment - Fundamentals and Applications*, IWA Publishing 1<sup>st</sup> Ed., London (2018) p. 39.
- [32] Z. Khuzwayo, E.M.N. Chirwa, S. Afr. J. Chem. Eng. 23 (2017) 17-25.
- [33] D.B. Miklos, C. Remy, M. Jekel, K.G. Linden, J.E. Drewes, U. Hubner, *Water Res.* 139 (2018) 118-131.
- [34] A. Sharma, J. Ahmad, S.J.S. Flora, *Environ. Res.* 167 (2018) 223-233.
- [35] D. Papaioannou, P.H. Koukoulakis, M. Papageorgiou, D.A. Lambropoulou, I.K. Kalavrouziotis, *Chemosphere* 238 (2020) 1-6.
- [36] A.L.A. Lucena, D.C. Napoleão, H.V.C. da Silva, R.M.R. Santana, B.G. Ribeiro, M.M.M.B. Duarte, *CeN.* 42 (2020) e9
- [37] A. Takdastan, A.H. Mahvi, E.C. Lima, M. Shirmardi, A.A. Babaei, G. Goudarzi, A. Neisi, M.H. Farsani, M. Vosoughi, *Water Sci. Technol.* 74 (2016) 2349-2363.

- [38] A.G.N. Wamba, K.N. Sylvere, E.C. Lima, J.G. Kayem, P.S. Thue, T.M.H. Costa, A.B. Quevedo, E.V. Benvenuti, F.M. Machado, J. Taiwan Inst. Chem. Eng. 102 (2019) 321-329.
- [39] A.A. Khan, M. Tahir, J. CO<sub>2</sub> Util. 29 (2019) 205-239.
- [40] Companhia Energética de Pernambuco - CELPE. Tabela de Tarifas de Energia Elétrica. Grupo B. Resolução homologatória Nº 2535 de 25 de abril de 2019. Vigência: 29/04/2019 a 28/04/2020, 2019.
- [41] K.H. Chan, W. Chu, Chemosphere 51 (2003) 305-311.
- [42] Y. He, N.B. Sutton, H.H.H. Rijnaarts, A.A.M. Langenhoff, Appl. Catal. B 182 (2016) 132-141.
- [43] D.C. Napoleão, L.E.M.C Zaidan, J.M. Rodríguez-Díaz, R.M.R. Santana, M.C.B.S.M. Montenegro, A.N. Araújo, M. Benachour, V.L. Silva, Afinidad. 75 (2018) 23-31.
- [44] M.M.M. Santos, M.M.M.B. Duarte, G.E. Nascimento, N.B.G.D. Souza, O.R.S. Rocha, Environ. Technol. 40 (2019) 1494-1507.
- [45] B.J. Young, N.I. Riera, M.E. Beily, P.A. Bres, D.C. Crespo, A.E. Ronco, Ecotoxicol. Environ. Saf. 76 (2012) 182-186.
- [46] K.E.A. Ibrahim, D.J. Solpan, Environ. Chem. Eng. 7 (2019) 102820.
- [47] N. López-Vinent, A. Cruz-Alcalde, L.E. Romero, M.E. Chávez, P. Marco, J. Giménez, S. Esplugas, J. Hazard. Mater. 380 (2019) 120882.
- [48] E.C. Lumbaque, B.A. Silva, F.C. Bock, G.A. Helfer, M.F. Ferrão, C. Sirtori, J. Hazard. Mater. 378 (2019) 1-9.
- [49] Y. Lan, L. Barthe, A. Azais, C. Causserand, Sep. Purif. Technol. 231 (2020) 1-10.
- [50] J.C. Crittenden, R.R. Trussel, D.W. Hand, K.J. Howe, G. Tchobanoglous, in MWH's Water Treatment: Principles and Design. 3<sup>rd</sup> Ed., John Wiley & Sons, Inc. New Jersey (2012) p. 509-532.
- [51] R.M.R. Santana, D.C. Napoleão, S.G.S. Júnior, R.K.M. Gomes, N.F.S. Moraes, L.E.M.C. Zaidan, D.R.M. Elihimas, G.E. Nascimento, M.M.M.B. Duarte, Chem. 75 (2021) p. 2305-2316.
- [52] G. Bedse, V. Kumar, S. Singh, J. Pharm. Biomed Anal. 49 (2009) 55-63.
- [53] M. Kurmi, A. Sahu, S. Singh, J. Pharm. Biomed. Anal. 134 (2017) 372-384.
- [54] X. Xie, Q. Zhou, Z. He, Y. Bao, Environ. Toxicol. Chem. 29 (2010) 922-928.
- [55] D. Sun, V. Mullerová, M.M. Ardestani, J. Frouz, Soil Tillage Res. 195 (2019) 1-9.
- [56] D.G. Hillis, J. Fletcher, K.R. Solomon, P.K. Sibley, Arch. Environ. Contam. Toxicol. 60 (2011) 220-232.
- [57] J. Wang, S. Wang, J. Clean. Prod. 315 (2021) 128202.

ALEX LEANDRO ANDRADE  
DE LUCENA  
RAYANY MAGALI DA ROCHA  
SANTANA  
MARCOS ANDRÉ SOARES  
DE OLIVEIRA  
LUCIANO COSTA ALMEIDA  
MARTA MARIA MENEZES  
BEZERRA DUARTE  
DANIELLA CARLA  
NAPOLEÃO

Chemical Engineering  
Department Federal University of  
Pernambuco, Recife, Brazil

NAUČNI RAD

## UTICAJ KOMBINOVANOG ZRAČENJA NA UKLANJANJE LAMIVUDINA I ZIDOVUDINA NAPREDNIM OKSIDACIONIM PROCESIMA

*Prisustvo farmaceutskih zagađivača u prirodi je ekološki problem koji izaziva sve veću zabrinutost. Zbog toga je neophodno proceniti tretmane koji mogu da razgrađuju ove zagađivače, kao što su napredni oksidacioni procesi (AOP). U ovom radu, smeša lekova lamivudina i zidovudine je tretirana u vodenoj sredini i sintetičkim rastvorima fotoperoksidacijom i foto-Fentonovim procesom. U ovu svrhu je korišćen stoni reaktor (UV-C, UV-A i zračenje sunčevom svetlošću). Efikasnost AOP tretmana je procenjena UV spektrofotometrijom. Testovi su uključivali primenu zračenja pojedinačno i kombinovano. Najbolji radni uslovi bili su [H<sub>2</sub>O<sub>2</sub>] od 600 mg/l i [Fe] od 0,5 mg/l, za obe matrice, sa degradacijom fotoperoksidacijom i foto-Fentonovim procesom, redom, od 90,53% i 89,32% u vodenim medijima. odnosno 88,69% i 85,79% u sintetičkim rastvorima. Istraživanja kinetike su potvrdila dva modela pseudo-prvog reda sa R<sup>2</sup> > 0,93. Testovi toksičnosti, koji su uključivali primenu semena zelene salate, šargarepe i paradajza, pokazali su inhibiciju za sva tri semena kada su podvrgnuta rastvorima nakon tretmana, za obe matrice. Ovu činjenicu potvrđuje HPLC analiza, u kojoj je verifikovano formiranje malih pikova, koji ukazuju na formiranje sporednih proizvoda. Dakle, može se potvrditi da su procesi foto-Fentona i fotoperoksidacije efikasni u degradaciji smeše lekova kada se primenjuje UV-C zračenje.*

*Ključne reči: hromatografija, lekovi, kinetičko modelovanje, sintetički efluent, toksičnost.*

BRUNA PRATTO <sup>1</sup>  
 MARTHA SUZANA  
 RODRIGUES DOS SANTOS-  
 ROCHA <sup>2</sup>  
 GUSTAVO BATISTA <sup>1</sup>  
 INTI DORACI CAVALCANTI-  
 MONTAÑO <sup>3</sup>  
 CARLOS ALBERTO  
 GALEANO SUAREZ <sup>3</sup>  
 ANTONIO JOSÉ  
 GONÇALVES CRUZ <sup>1</sup>  
 RUY DE SOUSA JÚNIOR <sup>1</sup>

<sup>1</sup> Chemical Engineering, Federal  
 University of São Carlos, São  
 Carlos, SP, Brazil

<sup>2</sup> Federal Institute of Alagoas,  
 Penedo, AL, Brazil

<sup>3</sup> Chemistry Institute, Federal  
 University of Goiás, Goiânia,  
 GO, Brazil

SCIENTIFIC PAPER

UDC 66.094.941:60:66

## RATIONAL FEEDING STRATEGIES OF SUBSTRATE AND ENZYMES TO ENZYMATIC HYDROLYSIS BIOREACTORS

### Article Highlights

- Rational feeding strategies of substrate and enzyme using pretreated sugarcane straw
- Enzyme pulses keeping at least 70% of the initial reaction rate improved process economy
- Unproductivity adsorption of enzymes was the main reason for hydrolysis yield reduction
- Soybean protein boosted the glucose production to 190 g/L and the yield to 94%
- Substrate feeding profiles are useful in the application of automatic solid feeders

### Abstract

*Bioreactors operating in fed-batch mode improve the enzymatic hydrolysis productivity at high biomass loadings. The present work aimed to apply rational feeding strategies of substrates (pretreated sugarcane straw) and enzymes (CellicCtec2<sup>®</sup>) to achieve sugar titers at industrial levels. The instantaneous substrate concentration was kept constant at 5% (w/v) along the fed-batch. The enzyme dosage inside the bioreactor was adjusted so that the reaction rate was not less than a pre-defined value (a percentage of the initial reaction rate -  $r_{min}$ ). When  $r$  reached values below  $r_{min}$ , enzyme pulses were applied to return the reaction rate to its initial value ( $r_0$ ). The optimized feeding policy indicated a reaction rate maintained at a minimum of 70% of  $r_0$ , based on the trade-off between glucose productivity and enzyme saving. Initially, it was possible to process a 21% (w/v) solid load, achieving 160 g/L of glucose concentration and 80% of glucose yield. It was verified that non-productive enzyme adsorption was the main reason for some reduction of hydrolysis yield regarding the theoretical cellulose-to-glucose conversion. An increment of 30 g/L in the final glucose concentration was achieved when a lignin-blocking additive (soybean protein) was used in the enzymatic hydrolysis.*

*Keywords: enzymatic hydrolysis, fed-batch operation, rational feeding strategies, sugarcane straw, unproductive lignin-enzyme bonds.*

Although the production of lignocellulosic-based ethanol has reached considerable technical maturity, it still faces bottlenecks regarding its feasibility, primarily due to the high enzyme costs and the low sugar levels obtained in the hydrolysis bioreactor [1,2]. In addition,

the ethanol titer in the conventional sugarcane mill reaches approximately 80 g/L in the fermentation stage [3,4], which is hardly obtained in the isolated second-generation ethanol process. Thus, an efficient enzymatic hydrolysis process is imperative for implementing lignocellulosic biorefineries [5].

One way to obtain elevated sugar concentrations is to process high biomass loadings (> 15% w/v dry mass for most pretreated materials) in the bioreactor [6]. However, in this approach, soluble sugars and phenolic compounds (generated in the biomass pretreatment process) rapidly accumulate in the reaction medium, causing enzyme inhibition in the early stages of hydrolysis [7]. Besides, high solid contents lead to high

Correspondence: R. de Sousa Júnior, Chemical Engineering Department, Federal University of São Carlos, Rod. Washington Luís-Km 235, CEP: 13565-905, São Carlos, SP, Brazil.  
 E-mail: ruy@ufscar.br  
 Paper received: 2 December, 2020  
 Paper revised: 30 June, 2021  
 Paper accepted: 25 August, 2021

<https://doi.org/10.2298/CICEQ201202030P>

apparent viscosity of slurries, resulting in heat and mass transfer limitations and increased power consumption associated with the medium agitation [8–10]. These issues represent negative impacts on hydrolysis yield, and the use of fed-batch operation offers an alternative approach to circumvent these problems.

Fed-batch hydrolysis has the advantage of processing a final high solid load at a controlled rate, maintaining low solids level inside the bioreactor at a time throughout the operation process. Thus, it is possible to get high sugar levels without compromising the hydrolysis yield and demanding less from the mixing system [8,10–12].

In addition to the benefits of substrate feeding, enzyme feed splitting can enhance enzymatic reaction performance by sustaining a high reaction rate throughout the process. On the other hand, one-batch enzyme addition subjects the enzymes to activity loss from the onset of the reaction [2].

Sugiharto *et al.* [13] evaluated different enzyme feeding strategies in the hydrolysis of empty fruit bunch. It was observed that proportional enzyme feeding (to substrate addition) increased the enzymatic digestibility and the glucose concentration, respectively, up to 26% and 12%, compared to the whole enzyme added at the beginning of the hydrolysis process. Corrêa *et al.* [8], employing steam-exploded sugarcane bagasse as substrate, also observed that enzyme addition along the hydrolysis time increased the glucose concentration by 10% and the energy efficiency (mass of glucose produced per energy consumed) by 25%, compared to all enzyme content added at the reaction onset.

Although the fed-batch mode presents better performance than simple batch, it is essential to define feeding profiles based on rational criteria. For instance, Modenbach and Nokes [6] raised some crucial questions regarding the proper fed-batch operation: at what point in the reaction time should subsequent substrate additions be applied to maintain a high conversion rate? Should enzymes be added in a single application, supplement the original application, or proportionally to the substrate?

Typically, the feeding strategies of substrate and enzyme are arbitrarily performed without considering reaction kinetics and parameters that affect it [11,12,14–16]. On the other hand, using rational feeding strategies of substrates and enzymes can improve product productivity, yield, and concentration.

Unrean *et al.* [17] developed a model of simultaneous saccharification and fermentation (SSF)

process considering the metabolic network of *S. cerevisiae* and kinetics of both enzymatic hydrolysis and fermentation to define optimal feeding profiles of sugarcane bagasse and cells on ethanol production. Through the feeding profiles, ethanol production with a titer up to 65 g/L and a high yield of 85% of theoretical yield (related to the total sugar available in pretreated bagasse) were accomplished. Besides, the ethanol titer and productivity were increased by 47% and 41%, respectively, compared to the batch process.

Cavalcanti-Montaño *et al.* [18] simulated and validated substrate and enzyme feeding strategies in the hydrolysis of alkali-pretreated sugarcane bagasse. The first policy adopted a substrate feeding profile and enzyme pulses based on the reaction kinetics. The second one defined only a substrate feeding profile, using the classic theory of optimal control [19]. The implemented strategies provided a final glucose concentration of up to 160 g/L by processing 23% w/v of solids with 8.2 FPU/g cellulose (*Accellerase*<sup>®</sup> 1500).

In this light, the objective of this work was to study the enzymatic hydrolysis of sugarcane straw in fed-batch mode, using rational substrate and enzyme feeding strategies to improve the process efficiency by increasing the final product concentration or decreasing the enzyme consumption in the hydrolysis process. Moreover, the definition of optimal substrate feeding profiles for different lignocellulosic materials is beneficial for applying automatic biomass feeders since they need pre-defined profiles to track (open loop process operation approach).

## MATERIALS AND METHODS

### Simulations of feeding profiles of substrate and enzyme to the enzymatic reactor

#### *Mathematical modeling of fed-batch enzymatic reactor*

The following hypotheses and simplifications were considered for the modeling of the fed-batch bioreactor:

a) Bioreactor operates in semi-continuous mode: initially, the bioreactor is loaded with a certain amount of biomass, and substrate additions are performed until the fed-batch process is completed. At the end of the feeding phase, the bioreactor starts operating in batch mode until the hydrolysis reaction ceases;

b) Pseudo-homogeneous reaction system: the reaction is heterogeneous - insoluble substrate; soluble enzyme - however, as the insoluble substrate load is low ~5% w/v, it can be assumed a homogeneous reaction medium. This concentration was chosen because it is below the threshold level (< 10% w/v) to prevent a too high viscosity and severe mixing problem in the medium [17].

- c) Substrates are uniformly accessible;  
 d) A single catalyst represents enzyme complex;  
 e) Enzyme is subjected to competitive inhibition by glucose;

f) Hemicellulose and lignin contents in the treated sugarcane straw are low and, therefore, disregarded since most were solubilized after hydrothermal + alkaline pretreatment (see Table 1).

A pseudo-homogeneous Michaelis-Menten (MM) kinetic model with inhibition by the product was considered. The kinetic parameters ( $K_m = 9.65 \pm 1.51$  g/L,  $K_i = 0.8 \pm 0.08$  g/L, and  $V_m = 0.214 \pm 0.003$  g/(L·min)) were obtained from previous work from hydrolyzed sugarcane straw assays in agitated flasks [20]. In the present study, the mathematical model will be used for experiments in bench-scale bioreactors and, therefore, a fine-tuning of the parameters was performed. After a manual fitting, the found values were:  $K_m = 9.65$  g/L,  $K_i = 1.85$  g/L, and  $V_m = 0.208$  g/(L·min). Figure A.1 (available from the author upon request) shows the very good fitting of the model to the experimental data in a way that the approach is validated.

Eqs. (1) to (4) describe the enzymatic reaction in fed-batch mode. Eq. (1) represents the mass balance for the substrate, Eq. (2) the mass balance for the product, Eq. (3) the total mass balance, and Eq. (4) the reaction rate of the enzymatic hydrolysis:

$$\frac{dC_s}{dt} = \frac{F_{s, fed} \cdot C_{s, fed}}{V} - r - \frac{F_{s, fed} \cdot C_s}{V} \quad (1)$$

$$\frac{dC_G}{dt} = r - \frac{F_{s, fed} \cdot C_G}{V} \quad (2)$$

$$\frac{dV}{dt} = F_{s, fed} \quad (3)$$

$$r = \frac{k \cdot C_E \cdot C_s}{K_m \cdot \left(1 + \frac{C_G}{K_i}\right) + C_s} \quad (4)$$

where  $F_{s, fed}$  (L/min) indicates the fed substrate flow,  $C_{s, fed}$  (g/L) is the concentration of substrate fed in terms of potential glucose,  $C_s$  (g/L) is the substrate concentration in the bioreactor in terms of potential glucose;  $C_G$  (g/L) is the concentration of glucose in the bioreactor,  $V$  (L) is the reaction volume at a given time,  $r$  (g/(L·min)) is the reaction rate,  $C_E$  (g/L) is the enzyme concentration required in the reaction medium,  $K_m$  (g/L) is the Michaelis-Menten constant,  $K_i$  (g/L) is the competitive inhibition constant by glucose, and  $k$  (1/min) is the specific reaction rate.

### Definition of substrate and enzyme feeding profiles

The substrate and enzyme feeding strategies are described in Eqs. (5) to (7):

$$e_{fed} = \frac{C_E \cdot V \cdot 230}{1.19} - e_{accumulated} \quad (5)$$

$$C_E = \frac{r_0 \cdot \left[ K_m \cdot \left(1 + \frac{C_G}{K_i}\right) \right] + C_{s,0}}{k \cdot C_{s,0}} \quad (6)$$

$$F_{s, fed} = \frac{r \cdot V}{C_{s, fed} - C_{s,0}} \quad (7)$$

where  $r_0$  (g/(L·min)) corresponds to the initial reaction rate and  $e_{fed}$  (FPU) refers to the amount of the enzyme to be added to the medium to maintain the reaction rate ( $r$ ) in a value not less than a pre-defined percentage of  $r_0$  ( $r_{min}$ ). When  $r$  reaches values below  $r_{min}$ , pulses of the enzyme are applied to return the reaction rate to its initial value ( $r_0$ ). Enzyme pulses can enhance the performance of enzymatic reaction by sustaining high reaction rates throughout the process. Therefore, different percentages (from 50% to 100%) of  $r_0$  were minimally kept ( $r_{min}$ ) in the bioreactor and the fed-batch phase. The choice of  $r_{min}$  was based on the trade-off between using lower amounts of enzyme and not significantly impacting the decrease in the glucose productivity to the reference ideal condition (100% of  $r_0$  - the enzyme fed continuously into the bioreactor). The  $e_{accumulated}$  (FPU) is the enzyme concentration already fed at a given reaction time.  $C_{s,0}$  refers to the substrate concentration at the start of the enzymatic hydrolysis.  $C_E$  must be multiplied by the reactor volume ( $V$ ) and the enzymatic activity (230 FPU/mL) and divided by the enzyme density (1.19 g/mL) to obtain  $e_{fed}$  in FPU units.

Eq. (7) shows the substrate feeding flow rate,  $F_{s, fed}$  (g/L). It is calculated according to the substrate consumption rate,  $r$  (keeping  $dC_s/dt \neq 0$ , i.e., the substrate is replaced as consumed). Processing a high biomass load is the way to obtain elevated sugar concentrations.

For computer simulations, Eqs. (1) to (7) were implemented in the software Matlab® R2017a.

### Experimental validation

#### Substrate and enzyme

Sugarcane straw used in this work was provided by Ipiranga Agroindustrial S.A. mill (Descalvado, SP, Brazil). The biomass was dried at room temperature until 10% moisture content. Afterward, it was milled in a

Wiley-type mill (SP-30, Splabor, Presidente Prudente, SP, Brazil) to a particle size of 10 mesh (2 mm). A cellulase complex, *CellicCTec2*<sup>®</sup>, donated by Novozymes Latin America (Araucária, PR, Brazil), with 230 FPU/mL [21], was employed in the hydrolysis experiments.

#### *Alkaline treatment of hydrothermally pretreated sugarcane straw*

Samples of sugarcane straw pretreated with liquid hot water (195 °C/10 min), described elsewhere [22,23], were alkaline treated using a proportion of 1:20 of dry pretreated sugarcane straw per NaOH solution (4% w/v). The suspension was added to 2-L Erlenmeyer flasks and autoclaved for 30 minutes at 121 °C and 1 atm. After the operation, the remaining solid fraction was washed with tap water (room temperature) until neutral pH was reached. Compositional analysis of sugarcane straw before and after alkaline treatment was carried out to determine the cellulose, hemicellulose, and lignin content [24].

#### *Enzymatic hydrolysis of sugarcane straw: application of substrate and enzyme feeding strategies*

The validation experiment regarding the substrate and enzyme feeding strategies was conducted in 400-mL bench-scale reactors (in triplicate) with a 50-mL fed-batch initial volume. The reactors were operated at 50 °C, 250 rpm, and pH 5.0 (50 mM citrate buffer). The biomass and the enzyme were added into the bioreactor during the fed-batch process according to the feeding profiles obtained by the simulations described in the “*Definition of substrate and enzyme feeding profiles*” section.

The reactor was initially loaded with a solids content of 5%  $w_{\text{dry biomass}}/v$  (corresponding to 47.8 g/L of potential glucose concentration) and 38.5 FPU of *CellicCTec2*<sup>®</sup> (corresponding to an initial concentration of 18 FPU/g<sub>cellulose</sub>) to avoid a high initial viscosity of the reaction medium. The substrate was manually fed every 0.5 h to keep the insoluble solids concentration constant at 5% w/v, processing a total (final) of 73 g biomass (final). Seven pulses of the enzyme were added over time, with 1450 FPU used. At the end of the reaction, the accumulated amounts of substrate and enzymes were equivalent to 21% w/v biomass and 22 FPU/g<sub>cellulose</sub>, respectively.

#### *Glucose quantification*

The hydrolysis was monitored in terms of glucose released along the reaction process. Glucose concentration was determined by HPLC (LC-10AD, Shimadzu, Tokyo, Japan), equipped with a refractive index detector (RID-10A, Shimadzu) and an Aminex 194

HPX-87H column (Bio-Rad, Hercules, CA, USA) operated at 65 °C using 5 mM H<sub>2</sub>SO<sub>4</sub> as a mobile phase (0.6 mL/min). Glucose yield (%) and productivity (g/(L·min)) were determined according to Eqs. (8) and (9), respectively. MG refers to the total mass of glucose released, and MC is the total mass of cellulose added into the bioreactor; 0.9 is the stoichiometric factor of glucose to equivalent cellulose.

$$\text{Glucose yield (\%)} = 0.9 \cdot \frac{M_G}{M_C} \cdot 100 \quad (8)$$

$$\text{Productivity (g / (L \cdot \text{min}))} = \frac{C_G}{t} \quad (9)$$

#### *Measurement of crystallinity index*

The crystallinity index of the biomass at the end of the reaction was analyzed by a Shimadzu XRD-6000 X-ray diffractometer (XRD-6000, Shimadzu, Tokyo, Japan), with Cu-K $\alpha$  radiation ( $\lambda = 1.54 \text{ \AA}$ ) generated at 30 kV and 30 mA. Scans were obtained in the  $2\theta$  range of 5–40° at a scan rate of 2°·min<sup>-1</sup>. The crystallinity index (*CrI*) was calculated from the ratio between the area of the crystalline peak ( $I_{002} - I_{AM}$ ) and the total area ( $I_{002}$ ) of the crystalline peak 002, after subtraction of the background signal measured without cellulose. OriginPro 8 software was used for diffractogram peak fitting, assuming Gaussian functions for each peak [25]. *CrI* values were calculated according to Eq. (10):

$$\text{CrI (\%)} = \left( 1 - \frac{I_{AM}}{I_{002}} \right) \cdot 100 \quad (10)$$

where  $I_{002}$  represents the crystalline peak intensity of the 002 crystal plane at  $2\theta = 22.8^\circ$ ; and  $I_{AM}$  is the minimum area between the 002 and the 101 crystalline peaks corresponding to the amorphous phase at  $2\theta = 18^\circ$ .

#### *Verification test of unproductive enzyme-lignin bonds*

Isolated soy protein (90% protein, Bremil, Brazil) was added to the hydrolysis reaction to verify whether there were any enzymes bounded unproductively. The assay was carried out under the conditions already described, except that soybean protein (8% w/w) was added at the beginning of the reaction. This additive was chosen in the present study because it is one of the lowest-cost blocking agents of unproductive enzyme bonds [26].

## RESULTS AND DISCUSSION

Hydrothermally pretreated sugarcane straw was submitted to alkaline treatment to remove the major content of lignin. Table 1 shows the chemical compositions of sugarcane straw before and after alka-

line treatment with NaOH.

It is worth noting that the alkaline treatment preserves a major part of the cellulose while removing

significant lignin amounts from the sugarcane straw hydrothermally pretreated. The treated biomass was then used to validate the most suitable feeding strategy simulations.

*Table 1. Chemical composition of sugarcane straw before and after alkaline delignification and the percentage of removal of the components*

Component (%)	Before alkaline delignification*	After alkaline delignification*	Removal after alkaline delignification*
	(Hydrothermally pretreated sugarcane straw)	(Hydrothermally pretreated sugarcane straw, treated with 4% w/v NaOH)	
Cellulose	54.7 ± 0.3	86.2 ± 0.3	7.65 ± 0.01
Hemicellulose	8.21 ± 0.05	2.89 ± 0.01	79.37 ± 0.01
Lignin	26.7 ± 0.9	7.5 ± 0.9	83.5 ± 0.1
Ash	6.7 ± 0.1	2.1 ± 0.5	81.6 ± 0.2
Total	96.3 ± 0.9	98.6 ± 1.1	-
Solid recovery <sup>a</sup>	-	58.6 ± 0.2	-

<sup>a</sup> Solid recovery =  $(m_{\text{final}}/m_{\text{initial}}) \times 100$ , where  $m_{\text{final}}$  (g) is the amount of dry biomass after treatment and  $m_{\text{initial}}$  (g) is the amount of dry biomass before treatment;

\* Values reported are average ± standard deviation of three replications

### Simulations for different feeding strategies of substrate and enzymes to the enzymatic hydrolysis bioreactor

Figure 1 shows the results of computational simulations when different percentages (from 50 to 100 %) of the initial reaction rate ( $r_0$ ) were minimally kept in the bioreactor and the fed-batch phase.

The glucose concentration profiles are depicted in Figure 1a. At the end of enzymatic hydrolysis, the glucose concentration reached 202 g/L, representing an ideal cellulose-to-glucose conversion of 100%. The interruption of the substrate feeding can be seen through the discontinuity in the glucose formation curves (at approximately 150 g/L of glucose for the different simulation cases), that is, by a rapid increase in the glucose concentration due to the instantaneous reduction of the dilution effect associated with biomass addition. Figure 1b illustrates the volume inside of the bioreactor for different feeding strategies assessed.

Figure 1c shows the reaction rate over time. The sudden increases in the reaction rates refer to the enzyme pulses given to return the reaction rate to its maximum (initial) value ( $r_0$ ). According to Figure 1d, continuous enzyme feeding is required during the fed-batch phase to keep the reaction rate at the maximum value (100% of  $r_0$ ). For the other conditions, the enzyme addition was only carried out when the reaction rate dropped to less than a pre-defined percentage of  $r_0$  ( $r_{\text{min}}$ ), resulting in pulse additions of the enzyme to return the reaction rate to its initial value ( $r_0$ ). The ideal

portion of  $r_0$  to be minimally kept in the bioreactor was based on a compromise solution by using the enzyme dosage as lower as possible without significantly reducing the glucose productivity.

Table 2 shows the values of glucose productivity and accumulated enzyme into the bioreactor, both respective to each minimum percentage of  $r_0$  that should be maintained during the fed-batch phase. First, the glucose productivity was determined considering 90% of the theoretical yield. Then, the reduction in productivity and enzyme consumption was calculated concerning the reference condition (100% of  $r_0$  - enzyme fed continuously in the bioreactor).

By sustaining the reaction rate above 80% of  $r_0$  (condition 3), the enzyme consumption and the glucose productivity were reduced by 24% and 9.7%, respectively. On the contrary, for condition 4, where the reaction rate is kept above 70% of  $r_0$ , it could be experienced 65% of enzyme savings with only 15.3% of productivity reduction. Besides, the decrease in the amount of enzyme added into the bioreactor is almost 3-fold higher than under condition 3.

In condition 5 ( $r$  kept above 60% of  $r_0$ ), the amount of enzyme added was higher than in condition 4. As enzyme additions were getting less frequent, adding a larger amount of enzyme was necessary to return the reaction rate to its initial value. For condition 6 ( $r$  kept above 50% of  $r_0$ ), there is almost 90% of enzyme savings.

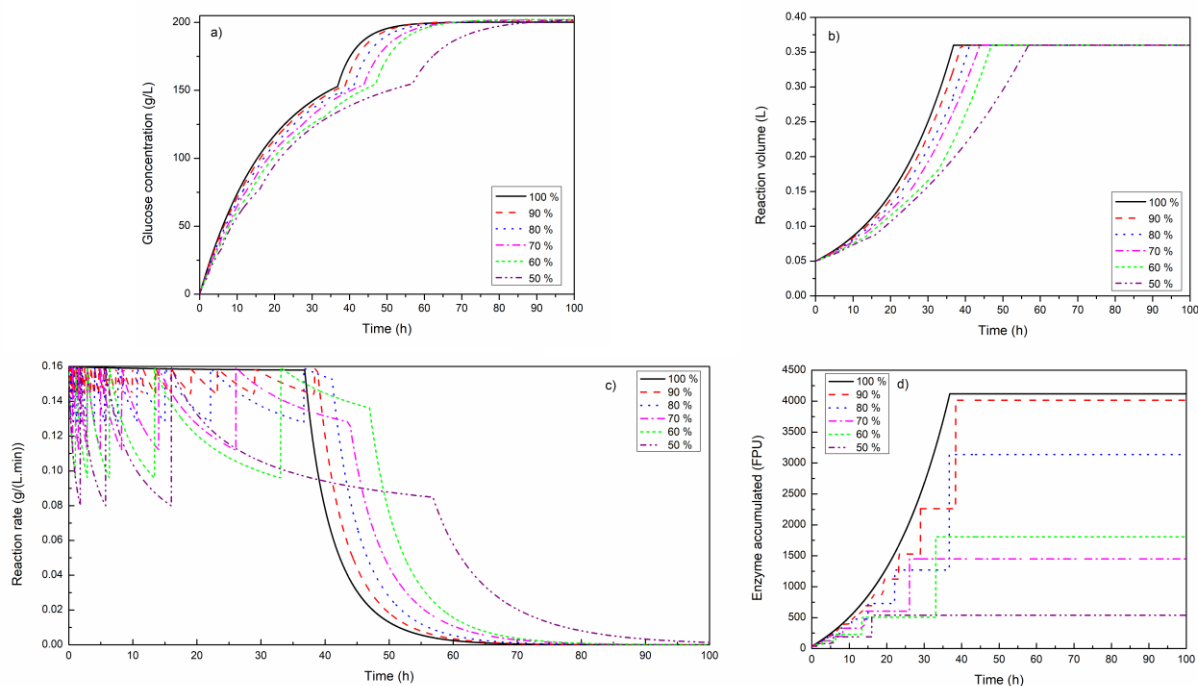


Figure 1. Simulations for different feeding strategies in the fed-batch bioreactor, keeping  $r$  at a minimum of pre-defined value (values from 50 to 100 % of  $r_0$ ): (a) glucose concentration; (b) volume; (c) reaction rate; (d) enzyme accumulated in the bioreactor.

Table 2. Different feeding strategies on productivities and enzyme consumption to achieve 90% cellulose-to-glucose conversion

Condition	Minimal $r$ (% $r_0$ )	Productivity (g/(L min))	Decrease in productivity*	$e_{accumulated}$ (FPU)	Decrease in $e_{accumulated}$ *
1	100	0.072	-	4118	-
2	90	0.069	4.2	4016	2.5
3	80	0.065	9.7	3137	23.8
4	70	0.061	15.3	1450	64.8
5	60	0.058	19.4	1807	43.9
6	50	0.046	36.1	540	86.9

\* Decrease in relation to the reference condition ( $r$  maintained equal to  $r_0$  throughout the fed-batch phase).

However, the productivity is reduced by 36%. The considerable drop in the use of enzyme was due to the reaction volume reaching the maximum capacity of the reactor before the next enzyme pulse (see Figures 1 (b) and (c)).

The values presented in Table 2 indicated that the strategy of maintaining the reaction rate at a minimum of 70% of  $r_0$  is the most suitable since there was a critical enzyme saving without causing a significant drop in productivity to the reference ideal condition (100% of  $r_0$  - enzyme fed continuously into the bioreactor). Figure 2 presents the profiles for the simulations considering 70% of  $r_0$  to be minimally

maintained over the fed-batch time.

The substrate concentration was kept constant until the maximum reactor capacity was reached (at 44 h, Figure 2a). After that, the substrate supply ceased, and the reactor started to operate in batch mode.

Figure 2b shows the enzyme additions and the enzyme accumulated along with the reaction. Seven pulses of enzymes were fed, totaling 1450 FPU of the enzyme accumulated inside the bioreactor. The enzyme addition was performed whenever the reaction rate reached 70% of  $r_0$  (approx. 0.112 g/(L min)) (Figure 2c).



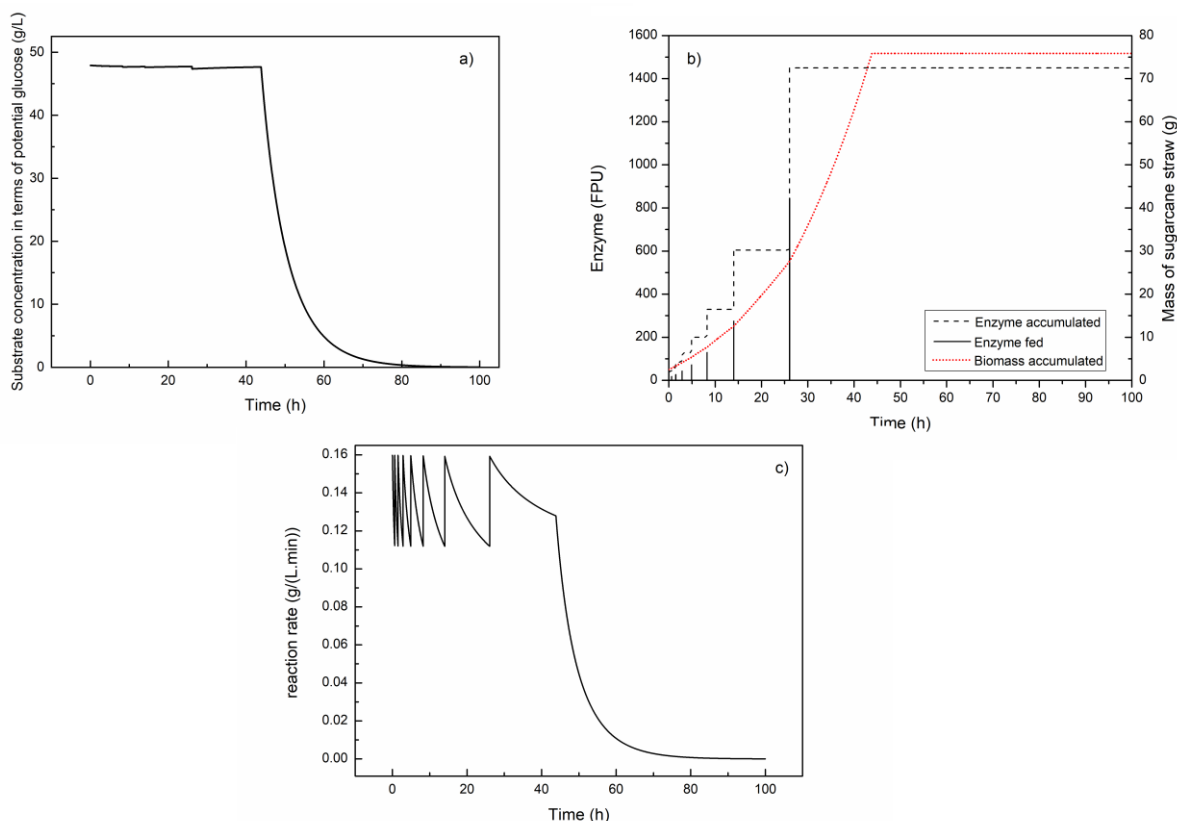


Figure 2. Simulations for fed-batch bioreactor with  $r$  maintained at a minimum of 70% of  $r_0$ : (a) substrate concentration; (b) enzyme fed, enzyme accumulated and biomass accumulated in the bioreactor; (c) reaction rate.

It can be observed in Figure 2b that the enzyme dosage was larger after each pulse. As glucose is being produced, the effects of enzyme inhibition become more significant [27,28]. Thus, higher enzyme amounts are needed for the reaction rate return to  $r_0$ . Figure 2b also shows the biomass accumulated during the reaction. It is observed that the mass of sugarcane straw remains constant after 44 h, indicating, once again, the end of the fed-batch phase.

Morales-Rodríguez *et al.* [29] optimized the fed-batch operation of a cellulose hydrolysis process. Three different feedback (PI) control strategies were developed and evaluated using the principles model of the hydrolysis process: the first one had insoluble solids as the control variable, handling the feed flow rate of the substrate; the second strategy additionally had the cellulose conversion as the control variable, adjusting the feed flowrate of enzyme for cellulose conversion; and the last one also considered the cellobiose conversion as the control variable, manipulating the enzyme feeding for cellobiose conversion. The third control strategy provided promising results regarding the hydrolysis performance with a substantial reduction in the amount of enzyme used in the process. Furthermore, as in the present study, Morales-Rodríguez *et al.* [29] also gave paramount importance

to the economy in the enzyme consumption when applying a rational fed-batch strategy.

Hodge *et al.* [30] developed an optimization strategy for cellulose hydrolysis for solid percentages higher than 15%. In addition, a feeding substrate profile was developed (based on optimal control theory) to maintain the insoluble solids concentration at a manageable level. When this strategy was used, the 80% cellulose conversion and 140 g/L of glucose were achieved, close to the predicted values for the discussed strategies, i.e., the glucose concentration reaching 202 g/L, for the ideal cellulose-to-glucose conversion of 100%.

### Experimental validation

Figure 3 shows the values of glucose concentration obtained along the experimental hydrolysis reaction time and in the simulation, for  $r$  maintained at a minimum of 70% of  $r_0$ .

From 144 h of reaction, no glucose release is observed. At this point, the hydrolysis reaction achieved 80% of yield and 160 g/L of glucose concentration. The titer obtained is adequate for large-scale processes since up to 81.8 g/L of ethanol could be generated in the fermentation stage. It is worth

mentioning that the increment of glucose concentration due to the hydrolysis reaction was not expressive after 84 h, indicating that the enzymatic hydrolysis could be ended at this time but still obtain a high glucose level (~ 140 g/L). Some further increase in concentration is mainly related to liquid fraction evaporation.

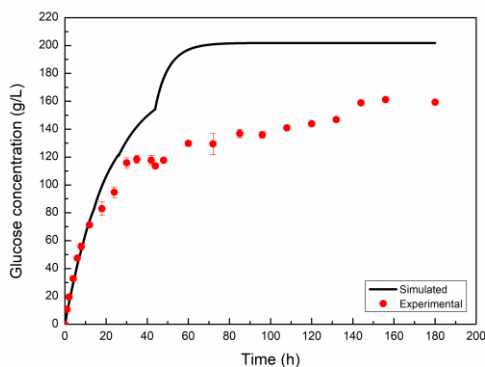


Figure 3. Experimental (\*) and simulated (—) data of released glucose in the enzymatic hydrolysis of sugarcane straw for  $r$  maintained at a minimum of 70% of  $r_0$  over reaction time.

The glucose yield obtained with the fed-batch enzymatic hydrolysis of sugarcane straw was higher than that of other authors for sugarcane bagasse. For example, Godoy *et al.* [12] attained 127 g/L of glucose concentration and 66.2% of glucose yield after 144 h of the fed-batch hydrolysis using the alkali-pretreated sugarcane bagasse (initial substrate content of 10% w/v followed by three additions of 5% (w/v) each). By processing the alkali-pretreated sugarcane bagasse in the fed-batch mode (initial load of 12% (w/v) and three more additions of 7% (w/v)), Gao *et al.* [15] obtained 129.50 g/L of glucose concentration with 60% of yield after 120 h of reaction.

The present results indicated that the rational substrate and enzyme feeding strategies enhanced the process efficiency compared to the arbitrarily feeding substrate (as adopted in the works mentioned above). Besides, in this work, lower solids content (5% w/v) was kept during the reaction process, implying a lower power requirement to agitate the system. Corrêa *et al.* [8] and Santos-Rocha *et al.* [10] verified that smoother feeding is more suitable for the formed glucose content and the required energy consumption.

The detachment of the experimental data to the simulation model (100% glucose yield) can be linked to the unpredicted phenomena by the kinetic model considered, such as an unproductive binding between enzymes and lignin, the remaining (crystalline) cellulose resistance to hydrolysis, and the internal diffusive effects. Regardless of the physical and

chemical phenomena that caused the hydrolysis yield reduction, the reaction reached equilibrium at 80% of conversion. Decreasing yield at high solids concentration is generally called solids-effect [31].

### Factors affecting enzymatic hydrolysis of lignocelluloses

The already mentioned phenomena were investigated to understand the factors associated with the incomplete cellulose-to-glucose conversion, such as:

1. Substrate depolymerization: cellulose recalcitrance is increased during the reaction. Fractions of the amorphous cellulose are depolymerized in the early stages of the reaction, leaving more crystalline parts in the final stages [32];

2. Deactivation of the enzymes: cellulases can become inactive due to unproductive adsorption onto lignin. Cellulases have a high affinity not only for cellulose but also for lignin. In the case of cellulose, they are usually released into the liquid fraction once the cellulose chains are hydrolyzed. In contrast, cellulases adsorbed onto lignin do not naturally desorb from it, a mechanism usually designated as non-productive binding [33].

One way to verify the effect of substrate depolymerization was to analyze the residual solid after the enzymatic hydrolysis reaction by XRD. Figure 4 shows the XRD diffractogram for the treated sugarcane straw after 156 h of fed-batch enzymatic hydrolysis. It shows the typical peaks of cellulose with a  $CrI$  of approximately 75%. This value is similar to the value found by de Aguiar *et al.* [34] for the alkali-pretreated sugarcane straw submitted to the enzymatic hydrolysis for 96 h.

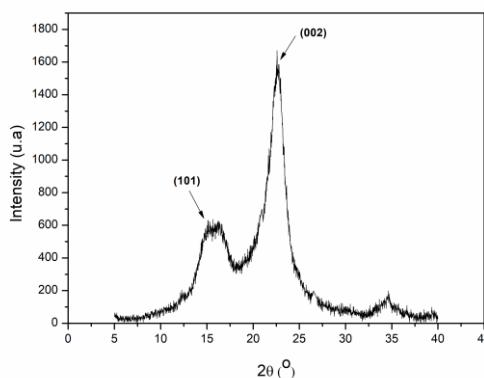


Figure 4. X-ray diffractograms of residual sugarcane straw after 156 h of fed-batch enzymatic hydrolysis of sugarcane straw maintaining  $r$  at a minimum of 70% of  $r_0$ .

Li *et al.* [35] verified a strong negative correlation

between reducing sugar yield and crystalline cellulose when enzyme loading was not a limiting factor ( $> 140 \text{ FPU/g}_{\text{cellulose}}$ ). However, at low enzyme loads ( $< 28 \text{ FPU/g}_{\text{cellulose}}$ ), there was no direct correlation between *CrI* and cellulose digestibility. In the present study, an enzyme loading of  $22 \text{ FPU/g}_{\text{cellulose}}$  was used, which limits, according to the criteria of Li *et al.* [35], the evaluation of crystallinity effect on hydrolysis efficiency. It is consensus that the decreased *CrI* values could facilitate the cellulose-to-sugars conversion. However, some studies [36,37] show that crystallinity is not a dominant factor for reducing cellulose digestibility.

Kristensen *et al.* [31] evaluated the effect of high-solids loading on the enzymatic hydrolysis of filter paper. There was a strong correlation between decreasing the adsorption of cellulases and conversion, indicating that the inhibition of the adsorption of the enzyme onto substrate was the main cause of the hydrolysis yield reduction.

Lignin-blocking agents can be added to the reaction medium to block the exposed lignin surface and verify the presence of the enzyme-lignin bonds [38]. These agents, in general, also disintegrate the hemicellulose-lignin bond, making the cellulose more accessible to the enzymatic attack [39]. Several additives, such as non-ionic surfactants (Tween 20 and 80), polyethylene glycol (PEG), and non-enzymatic proteins (bovine serum albumin, soybean protein, peptone), have been evaluated to avoid the unproductive enzymes bonds [26,39]. Here, the isolated soybean protein (ISP) was chosen due to the justification mentioned in the “*Verification test of unproductive enzyme-lignin bonds*” section.

Figure 5 shows the effect of soybean protein supplementing on the glucose concentration released

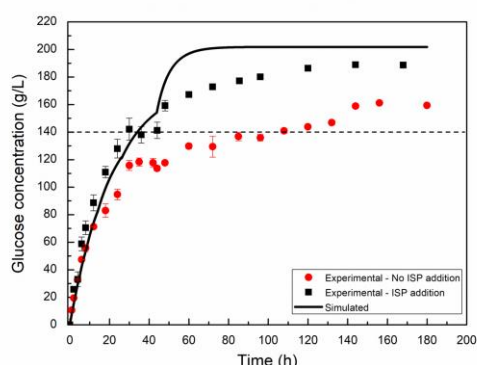


Figure 5. Effect of the soybean protein addition (■) on the enzymatic hydrolysis of sugarcane straw in the same conditions of enzymatic hydrolysis without ISP addition (●), compared to simulated data (—).

along the reaction course, compared with the assay

with no addition of the blocking agent (data from Figure 3).

The ISP additive increased glucose concentration from approximately 160 to 190 g/L, resulting in a gain of around 19% in cellulose-to-glucose conversion. The dashed line reveals that, in 48 h of reaction, the glucose amount released by the ISP-added assay was virtually the same as that obtained in 140 h of hydrolysis in the assay with no ISP addition. This behavior supports that enzymes were inactive (due to non-productive bonds), resulting in a slower reaction rate. A similar improvement was found by Brondi *et al.* [26] using 8% w/v of soybean protein in the enzymatic hydrolysis of steam-exploded sugarcane bagasse: the glucose amount released was increased by 25% after 96 h of reaction. Despite the great improvement obtained with the use of the additive, some detachment between experimental and simulated data persists, mainly between 40 and 60 h. It is justified because, experimentally, the effect of reducing the dilution at the end of the substrate feed (i.e., at the end of the fed-batch phase) was not so expressive.

Based on the observations above-mentioned, the main reason for the decrease of hydrolysis yield is the enzyme deactivation caused by the unproductive bonds. It is worth highlighting that the objective of using soybean protein, at this moment, was only for investigation purposes (verification of the presence of lignin-enzyme bonds) rather than process improvement. However, an optimized additive concentration can be obtained to establish the economic feasibility of its use on an industrial scale.

## CONCLUSION

Rational feeding strategies of substrate and enzymes were investigated to improve the enzymatic hydrolysis of pretreated sugarcane straw. With the feeding strategy adopted (reaction rate maintained at a minimum of 70% of  $r_0$ ), it was possible to process a total of 21% w/v biomass load (always keeping approximately 5% w/v of insoluble solids in the reaction medium at a time), achieving 80% of glucose yield and 160 g/L of glucose concentration. The hydrolysis yield decrease was mainly associated with unproductive enzyme adsorption. On the other hand, the lignin-blocking agent boosted the glucose production to 190 g/L, making it an alternative process enhancer for biorefinery applications. Moreover, the feeding profiles obtained here are beneficial from bioreactors engineering, such as, for example, in the application of an automatic substrate feeder.

## Acknowledgment

The authors would like to thank CNPq (National Council for Scientific and Technological Development, Brazil, Processes #312903/2018-9, and #140761/2017-9), and FAPESP (São Paulo State Research Funding Agency, Brazil, Process #2016/10636-8) for the financial support.

This study was also financed in part by the Coordenação de Aperfeiçoamento de Pessoal de Nível Superior - Brasil (CAPES) - Finance Code 001.

## REFERENCES

- [1] H. Shokrkar, S. Ebrahimi, M. Zamani, *Cellulose*. 25 (2018) 6279-6304.
- [2] A.S. da Silva, R.P. Espinheira, R.S.S. Teixeira, M.F. de Souza, V. Ferreira-Leitão, E.P.S. Bon, *Biotechnol. Biofuels*. 13 (2020) 58.
- [3] K.C.S. Rodrigues, J.L.S. Sonego, A. Bernardo, M.P.A. Ribeiro, A.J.G. Cruz, A.C. Badino, *Ind. Eng. Chem. Res.* 57 (2018) 10823-10831.
- [4] R.D. Pereira, A.C. Badino, A.J.G. Cruz, *Energy & Fuels*. 34 (2020) 4670-4677.
- [5] B. Pratto, M.S.R. dos Santos-Rocha, A.A. Longati, R. de Sousa Júnior, A.J.G. Cruz, *Bioresour. Technol.* 297 (2020) 122494.
- [6] A.A. Modenbach, S.E. Nokes, *Biomass and Bioenergy*. 56 (2013) 526-544.
- [7] D.B. Hodge, M.N. Karim, D.J. Schell, J.D. McMillan, *Bioresour. Technol.* 99 (2008) 8940-8948.
- [8] L.J. Corrêa, A.C. Badino, A.J.G. Cruz, *Bioprocess Biosyst. Eng.* 39 (2016) 825-833.
- [9] D.H. Fockink, M.B. Urio, J.H. Sánchez, L.P. Ramos, *Energy & Fuels*. 31 (2017) 6211-6220.
- [10] M.S.R. Santos-Rocha, B. Pratto, L. Jacob, A. Colli, R. Maria, R. Garcia, A. José, G. Cruz, *Ind. Crop. Prod.* 125 (2018) 293-302.
- [11] Y.H. Jung, H.M. Park, D.H. Kim, J. Yang, K.H. Kim, *Appl. Biochem. Biotechnol.* 182 (2017) 1108-1120.
- [12] C.M. de Godoy, D.L. Machado, A.C. da Costa, *Fuel*. 253 (2019) 392-399.
- [13] Y.E.C. Sugiharto, A. Harimawan, M.T.A.P. Kresnowati, R. Purwadi, R. Mariyana, Andry, H.N. Fitriana, H.F. Hosen, *Bioresour. Technol.* 207 (2016) 175-179.
- [14] M.R. Mukasekuru, P. Kaneza, H. Sun, F.F. Sun, J. He, P. Zheng, *Ind. Crops Prod.* 146 (2020) 112156.
- [15] Y. Gao, J. Xu, Z. Yuan, Y. Zhang, Y. Liu, C. Liang, *Bioresour. Technol.* 167 (2014) 41-45.
- [16] C. Xu, J. Zhang, Y. Zhang, Y. Guo, H. Xu, J. Xu, Z. Wang, *Bioresour. Technol.* 292 (2019) 121993.
- [17] P. Unrean, S. Khajeeram, K. Laoteng, *Appl. Microbiol. Biotechnol.* 100 (2016) 2459-2470.
- [18] I.D. Cavalcanti-Montaño, C.A.G. Suarez, U.F. Rodríguez-Zúñiga, R. de Lima Camargo Giordano, R. de Campos Giordano, R. de Sousa Júnior, *Bioenergy Res.* 6 (2013) 776-785.
- [19] W.F. Ramirez, *Process control and identification*, Academic Press, Boston, 1994.
- [20] B. Pratto, R.B.A. de Souza, R. Sousa, A.J.G. da Cruz, *Appl. Biochem. Biotechnol.* 178 (2016) 1430-1444.
- [21] T. Ghose, *Pure Appl. Chem.* 59 (1987) 257-268.
- [22] G. Batista, R.B.A. de Souza, B. Pratto, M.S.R. Santos-Rocha, A.J.G. da Cruz, *Bioresour. Technol.* 275 (2019) 321-327.
- [23] M.S.R. Santos-Rocha, B. Pratto, R. de Sousa, R.M.R.G. Almeida, A.J.G. Cruz, *Bioresour. Technol.* 228 (2017) 176-185.
- [24] A. Sluiter, B. Hames, R. Ruiz, C. Scarlata, J. Sluiter, D. Templeton, D. Crocker, *Determination of structural carbohydrates and lignin in biomass. Technical Report NREL/TP-510-42618.*, (2008).
- [25] S. Park, J.O. Baker, M.E. Himmel, P.A. Parilla, D.K. Johnson, *Biotechnol. Biofuels*. 3 (2010) 10.
- [26] M.G. Brondi, V.M. Vasconcellos, R.C. Giordano, C.S. Farinas, *Appl. Biochem. Biotechnol.* (2018) 1-13.
- [27] F. Xu, H. Ding, *Appl. Catal. A Gen.* 317 (2007) 70-81.
- [28] R. Sousa, M.L. Carvalho, R.L.C. Giordano, R.C. Giordano, *Brazilian J. Chem. Eng.* 28 (2011) 545-564.
- [29] R. Morales-Rodriguez, A.S. Meyer, K. V. Gernaey, G. Sin, *Bioresour. Technol.* 102 (2011) 1174-1184.
- [30] D.B. Hodge, M.N. Karim, D.J. Schell, J.D. McMillan, *Appl. Biochem. Biotechnol.* 152 (2009) 88-107.
- [31] J.B. Kristensen, C. Felby, H. Jørgensen, *Biotechnol. Biofuels*. 2 (2009) 11.
- [32] X. Zhao, L. Zhang, D. Liu, *Biofuels Bioprod. Biorefining*. 6 (2012) 465-482.
- [33] D. Gomes, J. Cunha, E. Zanuso, J. Teixeira, L. Domingues, *Polysaccharides*. 2 (2021) 287-310.
- [34] J. de Aguiar, T.J. Bondancia, P.I.C. Claro, L.H.C. Mattoso, C.S. Farinas, J.M. Marconcini, *ACS Sustain. Chem. Eng.* 8 (2020) 2287-2299.
- [35] L. Li, W. Zhou, H. Wu, Y. Yu, F. Liu, D. Zhu, *BioResources*. 9 (2014) 3993-4005.
- [36] S.C. Pereira, L. Maehara, C.M.M. Machado, C.S. Farinas, *Renew. Energy*. 87 (2016) 607-617.
- [37] C. Rezende, M. de Lima, P. Maziero, E. DeAzevedo, W. Garcia, I. Polikarpov, *Biotechnol. Biofuels*. 4 (2011) 54.
- [38] J.K. Ko, E. Ximenes, Y. Kim, M.R. Ladisch, *Biotechnol. Bioeng.* 112 (2015) 447-456.
- [39] C. Florencio, A.C. Badino, C.S. Farinas, *Bioresour. Technol.* 221 (2016) 172-180.

BRUNA PRATTO <sup>1</sup>  
MARTHA SUZANA  
RODRIGUES DOS SANTOS-  
ROCHA <sup>2</sup>

GUSTAVO BATISTA <sup>1</sup>  
INTI DORACI CAVALCANTI-  
MONTAÑO <sup>3</sup>

CARLOS ALBERTO  
GALEANO SUAREZ <sup>3</sup>

ANTONIO JOSÉ  
GONÇALVES CRUZ <sup>1</sup>

RUY DE SOUSA JÚNIOR <sup>1</sup>

<sup>1</sup> Chemical Engineering, Federal  
University of São Carlos, São  
Carlos, SP, Brazil

<sup>2</sup> Federal Institute of Alagoas,  
Penedo, AL, Brazil

<sup>3</sup> Chemistry Institute, Federal  
University of Goiás, Goiânia, GO,  
Brazil

## RACIONALNE STRATEGIJE DOLIVANJA SUPSTRATA I ENZIMA U BIOREAKTORE ZA ENZIMSKU HIDROLIZU

*Bioreaktori sa dolivanjem poboljšavaju produktivnost enzimske hidrolize pri visokim koncentracijama biomase. Ovaj rad je imao za cilj da primeni racionalne strategije dolivanja supstrata (prethodno obradene slame šećerne trske) i enzima (CellicCtec2®) za postizanje prinosa šećera na industrijskim nivoima. Trenutna koncentracija supstrata je održavana konstantnom na 5% (m/v) tokom dolivanja. Doziranje enzima u bioreaktor je podešeno tako da brzina reakcije nije manja od unapred definisane vrednosti (procenat početne brzine reakcije -  $r_{min}$ ). Kada  $r$  dostigne vrednosti ispod  $r_{min}$ , dodavan je enzim da bi se brzina reakcije vratila na početnu vrednost ( $r_0$ ). Optimizovana politika dolivanja je pokazala da se brzina reakcije održava na minimum 70% od  $r_0$ , na osnovu kompromisa između produktivnosti glukoze i uštede enzima. U početku je bilo moguće obraditi 21% (m/v) čvrstog supstrata, postizući koncentraciju glukoze od 160 g/l i prinos glukoze od 80%. Verifikovano je da je neproduktivna adsorpcija enzima glavni razlog za izvesno smanjenje prinosa hidrolize u odnosu na teorijski stepen konverzije celuloze u glukozu. Povećanje konačne koncentracije glukoze od 30 g/l postignuto je kada je u enzimskoj hidrolizi korišćen aditiv koji blokira lignin (protein soje).*

*Ključne reči: enzimska hidroliza, operacija dolivanja, racionalne strategije dolivanja, slama od šećerne trske, neproduktivne veze lignin-enzim.*

NAUČNI RAD



ABULHASSAN ALI  
 KHURAM MAQSOOD  
 AYMN ABDULRAHMAN  
 AHMAD S. ALSAADI  
 ABDULLAH BIN MAHFOUZ

Department of Chemical  
 Engineering, University of Jeddah,  
 Jeddah, Saudi Arabia

SCIENTIFIC PAPER

UDC 678.7:66:66.095.21

## OPTIMAL DISSOLUTION AND VISCOELASTIC BEHAVIOR OF POLYAMIDE-66 IN FORMIC ACID FOR MEMBRANE FABRICATION

### Article Highlights

- High-performance polymeric membrane fabrication
- Response surface methodology based techniques for the modeling and optimization
- RSM modeling is employed to evaluate linear, quadratic, and interactive effects
- Process parameters optimized to minimize viscosity

### Abstract

*High-performance polymeric membrane technology is rapidly developing worldwide with the introduction of new materials and processes. Considerable research efforts are being made to establish a polymer membrane that can be used for ultrafiltration (UF) or nanofiltration (NF) applications. The development of modified polyamide-66 polymer and its compatibility in wastewater are essential elements in the quest for advances and improvements in membrane technology. The optimized conditions for membrane synthesis are critical in making it commercially viable. Response Surface Methodology (RSM) was used to find the optimum dissolution of polyamide-66 in formic acid. A model was developed and validated with experimental data, and it showed good agreement with  $R^2$  0.9984. The optimized condition for minimizing viscosity was determined. For minimum viscosity (3.64 cp), the optimum temperature and wt. % were 20 °C and 0.6, respectively.*

*Keywords: optimization, polyamide-66, polymeric membrane, RSM, viscosity.*

Aliphatic polyamide (PA, nylon) films are one of the most popular materials for membrane synthesis due to their permeability qualities for ultrafiltration (UF) and nanofiltration (NF) applications [1]. Different kinds of nylon, including nylon 66, show excellent permeability characteristics to smaller urea, water, and sodium chloride molecules. In contrast, higher molecular weight molecules and the non-ionized and less polar species display less diffusion through nylon films [2].

Polyamide thin-film composite (TFC) membranes dominate the RO membrane market. It consists of polyester web, a microporous interlayer, and an ultra-

thin barrier layer [3]. Aromatic polyamide is the most common material used in barrier layers. The process is done mainly via interfacial polymerization of 1,3-phenylenediamine and the tri-acid chloride of benzene [4]. Enhanced resistance to chemical attack and structural stability allows it to tolerate impurities, last longer, and clean more efficiently [5, 6]. Different studies are available in the literature for preparing polyamide 6. Peng *et al.* [7] produced semi-aromatic modified PA6 through a green and efficient in situ polymerization method. They used caprolactam, purified terephthalic acid (PTA) without adding a conventional polymerization initiator. As a result of the polymerization process, the possible path is that a random distribution of PTA might occur in the copolymer once the amide is exchanged.[7]. In another study, Polyamide 6-based copolymer with a molecular structure comparable to polyamide 6 was prepared using amide exchange [8]. Polyamide spiral wound membranes dominate the RO/Nanofiltration (NF) market with a 91 percent share because of its higher

Correspondence: A. Ali, Department of Chemical Engineering, University of Jeddah, Jeddah, Saudi Arabia.

E-mail: aquddusi@uj.edu.sa

Paper received: 20 March, 2021

Paper revised: 25 August, 2021

Paper accepted: 9 September, 2021

<https://doi.org/10.2298/CICEQ210320032A>

salt rejection ability and net pressure as the driving force [9]. However, in another study [10], compared to alcohol/salts, the dissolution of PA solution in different organic and acid solvents differs from solvent to solvent, which profoundly influences the PA dope solution viscosity [11]. Concerning the dissolved state of the PA in acid solvents, the PA molecular chain reveals polyelectrolyte nature in an aqueous acid solution and an aqueous concentrated sulfuric acid solution due to the protonation of the polymer amide group, which strongly interacts with the polymer chains [12].

The casting solution is one of the essential factors for the high-performance membrane. The membrane structure and skin properties mainly depend upon the type of solvent, the viscosity of the solution, and the concentration of the polymer [13]. Nevertheless, polyamide glassy nature and crystalline structure are resistant to many polar, dipolar, and nonpolar solvents. However, multiple researchers reported that the dissolved state of polyamide in the alkyl solvents cooperated with inorganic salts such as methanol with LiCl, CaCl<sub>2</sub>, SnCl<sub>4</sub>, and TiCl<sub>4</sub>, respectively, can be used to enhance properties [12].

Idris and Ahmed [14] highlighted that the polymer and viscosity concentration are the main parameters that influence the structure and performance of the membranes. They also highlight the effect of viscosity and concentration on the membrane's performance, along with the fact that too high or too low viscosities significantly impact the performance of the membrane. The present study includes an optimization study of the experimental data available in the literature [15]. Research studies have been conducted to determine the best techniques for determining maximum and minimum response for attributes [16, 17]. It is possible to determine the optimum parameter values using various optimization methods. Using the VIKOR method, complex systems with many criteria may be optimized efficiently. This approach is based on rating and picking from a collection of presented options [18]. A second method TOPSIS is based on the idea that the selected choice should be the one that comes closest to the ideal solution and remains far from the negative-ideal option.

In contrast, the mathematics-based Promethee may solve issues involving several criteria and have various applications in picking acceptable alternatives, prioritizing tasks, and predicting [19]. The present study's data is optimized using Response Surface Methodology (RSM), a relatively advanced and more reliable technique. RSM is a practical and valuable tool for evaluating the relationship between process input and response for experimental design. Multiple runs

are usually done by varying the values of parameters [20]. Once the data is collected, statistical analysis is conducted to find the inaccuracies in the measured data. The interaction between the factors is also considered for studying the multiple factors and individual factors' impact [21]. This study finds the two main factors, i.e., concentration and temperature, to optimize viscosity, leading to an excellent membrane fabrication for water application.

## MATERIALS AND METHODS

The input parameters studied in this work are polyamide-66 polymer weight percent (wt. %) and temperature. In addition, the effect of polyamide-66 concentration and temperature on the viscosity of the solution was examined. Face-centered central composite design (CCD) was used to evaluate parameters. The face-centered CCD consists of six face-centered, eight corner points, and six center points. The input values of the parameters are provided in Table 1. The experimental data are taken from the research presented by Alghoraibi [15]. Polyamide-66 (PA66) polymer (Mw 262,35 g/mol) was received from Sigma Aldrich Co. Statistically, the analysis of RSM was used to form an empirical relationship between the temperature, concentration, and viscosity (response).

The RSM is considered authentic and consistent in the research investigation. The most important part of this technique is examining the effect of the least and most significant factors on the final response. The capability of RSM to analyze multiple inputs to produce a single output makes it very attractive for researchers in modeling and optimization. The present work includes developing an empirical model to predict the change in viscosity of polyamide-66 mixture with the change in wt.% and temperature. In the next step, an optimization was conducted using a developed model. The work was started by creating a second-order polynomial equation to show the relationship between parameters and output. The general correlation is given in Eq. (1):

$$\text{Response} = \beta_0 + \sum_{i=1}^p \beta_i X_i + \sum_{i=1}^p \beta_{ii} X_i^2 + \sum_{i=1}^{p-1} \sum_{j=1}^p \beta_{ij} X_i X_j \quad (1)$$

where  $\beta_0$  is a constant, the coefficients  $\beta_1, \beta_2, \dots, \beta_p$  and  $\beta_{11}, \beta_{22}, \dots, \beta_{pp}$  are the linear and quadratic terms, respectively while  $\beta_{12}, \beta_{13}, \dots, \beta_{p1}$  are the interacting terms.

## RESULTS AND DISCUSSION

Considering that the reaction is dependent on a single component, it is essential and rational to find out



the influence of both parameters concurrently [22]. The results of the design of experiment (DoE) with face-centered CCD method using the Polyamide-66 wt. % and the temperature (°C) as the input factors and the corresponding response, viscosity, are provided in Table 1.

Table 1. DoE according to face-centered CCD

Sr. No	Temperature (°C)	(wt. %)	Viscosity
	A	B	cp
1	30	0	0.84
2	30	1.5	6.65
3	30	1.5	6.57
4	30	3	12.8
5	10	0	1.0
6	50	0	0.5
7	30	1.5	6.4
8	30	1.5	6.5
9	10	1.5	9.9
10	10	3	17.6
11	50	1.5	4.6
12	30	1.5	6.45
13	50	3	8.5

An empirical relationship using RSM is developed and tested between polyamide-66 wt. %

Table 2. ANOVA results for the viscosity

Source	Sum of Squares	Degree of freedom	Mean Squares	F values	p values
Model	278.82	5	55.76	853.09	< 0.0001
A	37	1	37	566.06	< 0.0001
B	222.77	1	222.77	3408.02	< 0.0001
A <sup>2</sup>	0.49	1	0.49	7.43	0.0295
B <sup>2</sup>	3.16E-04	1	3.16E-04	4.83E-03	0.9465
AB	18.49	1	18.49	282.86	< 0.0001
Residual	0.46	7	0.065	-	-
Lack of Fit	0.42	3	0.14	14.34	0.0132
Pure Error	0.039	4	9.73E-03	-	-
Cor Total	279.28	12	-	-	-

$$\text{Viscosity} = -0.0795A + 6.226B + 0.001048A^2 - 0.00475B^2 - 0.0176AB + 1.9439 \quad (2)$$

The  $R^2$ -values for the original and reduced model are compared in Table 4. Both models show high-efficiency prediction as to the  $R^2$ -value is almost approaching 1. However, after backward elimination (reduced model), the model shows an enhancement

and temperature, considering the mixture's viscosity as output in the form of a quadratic polynomial. The development of an empirical equation was followed by optimization using the analysis of variance (ANOVA). The results provide a relationship among the parameters, their interactions, and the squares of the inputs (Table 2). The model is highly significant as the table has an overall  $F$ -value of 853.09 for the viscosity and a low probability value ( $p$ -value = <0.0001), considering that the resulting  $p$ -value is less than 0.05 [23,24]. These results highlight that prediction and optimization are possible using the developed model. The results in Table 2 also show that the developed model has five significant terms, namely  $A$ ,  $B$ ,  $A^2$ ,  $B^2$ , and  $AB$ . Eq. 2 represents the developed model.

The model can be improved by removing non-significant terms using the backward elimination process. The terms with minimal effect can be omitted without affecting the required ones in the developed model.  $R^2$  values and the ANOVA table were further used to compare and examine the model. This comparison can help enhance the model efficiency. The new and reduced model is further processed using a backward elimination process; the ANOVA values are provided in Table 3. With a  $p$ -value less than 0.05, it is clear from this table that the  $F$ -value for the reduced model is greater than the  $F$ -value for the original model. These results show the improvements in the analysis by using the reduced model.

in Adeq. Precision value. The new amount of Adeq. Precision is 116 compared to the previous value of 99.25, which means the new model is improved. In this way, the final viscosity model that may be utilized for further analysis, prediction, and optimization has been presented by Eq. 3.

Table 3. ANOVA results of viscosity by using the reduced model

Source	Sum of Squares	Degree of freedom	Mean Squares	F values	p values
Model	278.82	4	69.71	1217.86	< 0.0001
A	37	1	37	646.48	< 0.0001
B	222.77	1	222.77	3892.19	< 0.0001
A <sup>2</sup>	0.56	1	0.56	9.73	0.0142
AB	18.49	1	18.49	323.05	< 0.0001
Residual	0.46	8	0.057	-	-
Lack of Fit	0.42	4	0.1	10.76	0.0204
Pure Error	0.039	4	9.73E-03	-	-
Cor Total	279.28	12	-	-	-

Table 4. R-squared values the model

Terms	Before backward elimination	After backward elimination
R <sup>2</sup> (overall)	0.998	1
Adjusted R <sup>2</sup>	0.997	1
Predicted R <sup>2</sup>	0.988	0.99
Adeq. Precision	99.25	116

$$\text{Viscosity} = -0.07895A + 6.212B + 0.001038A^2 - 0.0716AB + 1.9423 \quad (3)$$

### Adequacy tests of the developed models

It is essential to test the developed model by plotting the residues curves. Points in the residual plot should be near a straight line and not follow a pattern. The residual plot for the viscosity model is presented in Figure 1. It is evident from the figure that there is no sequence exists between the points, and a fall of residual to the straight line confirms the normal distribution of errors reaffirming the least square fit [25]. The graphical representation means that the results are satisfactory, and the model can be used for prediction and optimization.

Further, the externally studentized residual versus predicted plot is presented in Figure 2. No evident and unusual pattern was found. Therefore, an acceptable range of  $\pm 4.5$  has been selected for the good points in this study. The randomly scattered plot within acceptable range exhibited the absence of lurking variables and shows that the model is credible and adequate. The results also confirm the validity of the model and the effectiveness of the randomization process [26]. Generally, negative residual values mean an over prediction, a positive residual point to a low prediction. Any plot closer to the estimated regression line at zero (0) highlights the exactness of model prediction [27]. The data points which do not come in this range are considered unreliable. Figure

2 shows that all the data points fall in the given range.

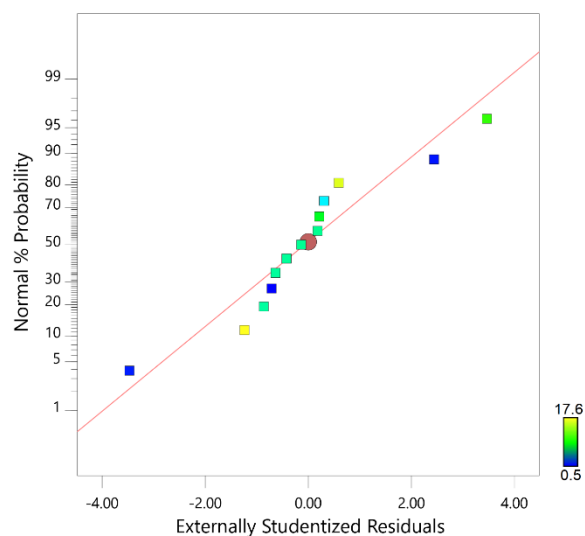


Figure 1. Normal plot of residual.

### Verification tests of the models

The results were verified by selecting a random set of data and then comparing it with results obtained in the model using Eq. (3). Figure 3 shows the results of the comparison. It is evident from the figure that the developed model's predicted results show excellent

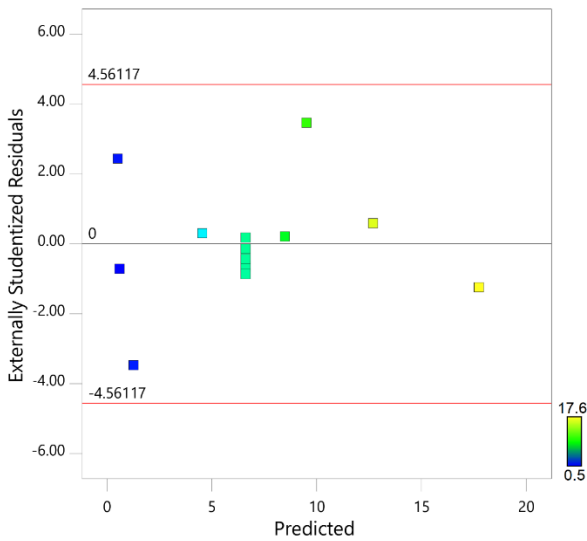


Figure 2. Externally Studentized Residual versus predicted plot for the viscosity model.

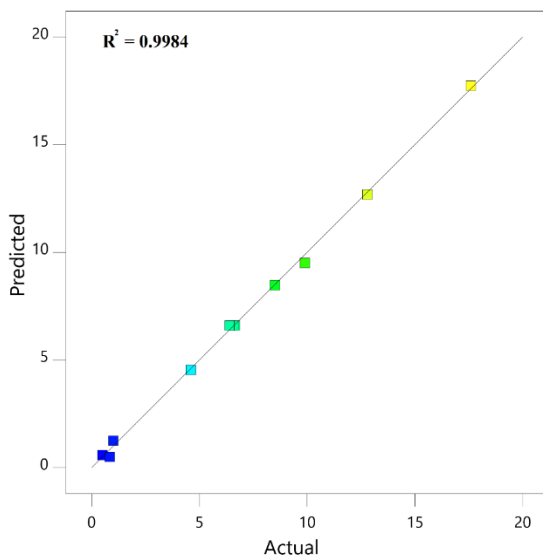


Figure 3. Validation of the model.

agreement with the experimental values with an  $R^2$  of 0.998.

It showed that data points were near the diagonal line and revealed that the observed response showed an excellent analogy to the predicted one. It is clear from the validation that the proposed model can be applied to the present system. To better understand the model results, a contour plot with a 3D surface plot has been drawn in Figure 4. Polyamide 66 wt.%, temperature, and viscosity have been plotted on the surface plot. Figure 4 highlights the fact that lower temperature leads to higher concentration viscous polyamide-66 mixture.

All the data required for fulfilling the primary goal of minimizing viscosity, including optimization cases,

their ranges, their objectives, and factors, are provided in Table 5. The present results were achieved by combining the input parameters using multi-objective optimization. The advantage is that it arranges the input parameters so that the final response provides the best results. The solutions to the optimization case are summarized in Table 5 and Figure 5. Finding the best solution with minimum viscosity with the highest desirability (0.934) is essential. Table 6 shows that in the case of minimum viscosity (3.64 cp), temperature and weight percent, 20 °C and 0.6 were the optimal values.

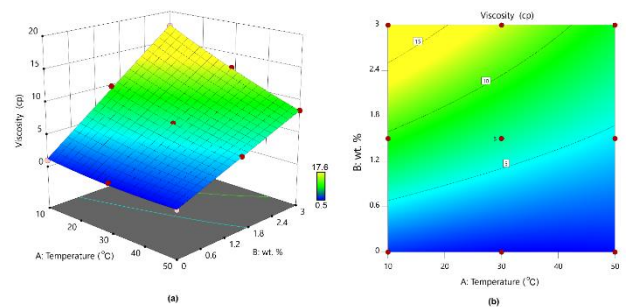


Figure 4. 3D response surface plot (a) and contour plot (b).

Table 5. All the optimization cases, their objectives, factors, and ranges

Name	Goal	Lower		Upper		Importance
		Limit	Weight	Limit	Weight	
Temperature	is in range	10	1	50	1	3
wt. %	is in range	0	1	3	1	3
Viscosity	Minimize	0.5	1	17.6	1	3

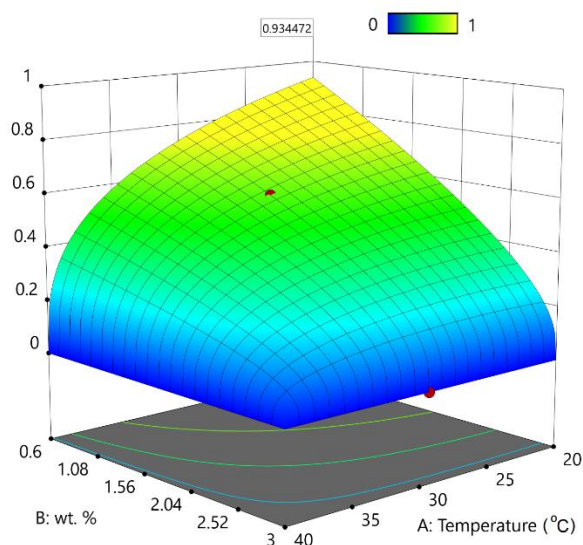


Figure 5. 3D surface plot for the input parameters and desirability.

Table 6. Optimization solutions for minimize viscosity

Number	Temperature (°C)	wt. %	Viscosity (cp)	Desirability
1	20.0	0.60	3.64	0.934
2	20.0	0.712	4.18	0.907
3	23.18	0.60	3.39	0.887

## CONCLUSION

The present study explores the optimization of the viscosity of polyamide-66 dissolutions in formic acid. Using RSM, an empirical model was developed to predict the viscosity by considering input factors such as temperature and concentration. The model was tested and validated, which showed a good agreement with experimental results. The model's error was measured using statistical techniques, which is 0.9984. An optimization scenario was investigated, which included the minimization of viscosity. The optimum temperature (20 °C) and concentration (0.6 wt.%) were calculated with the minimum viscosity value of 3.64 cp.

## Acknowledgment

This work was funded by the University of Jeddah, Saudi Arabia, under grant No. (UJ-37-18-DR). The authors, therefore, acknowledge with thanks the University's technical and financial support.

## REFERENCES

- [1] H.H. Wang, J.T. Jung, J.F. Kim, S. Kim, E. Drioli, Y.M. Lee, *J. Membr. Sci.* 574 (2019) 44-54.
- [2] H.B. Kostenbauder, H.G. Boxenbaum, P.P. Deluca, *J. Pharm. Sci.* 58 (1969) 753-757.
- [3] A. Al Mayyahi, *Membranes* 8 (2018) 68.
- [4] K.P. Lee, T.C. Arnot, D. Mattia, *J. Membr. Sci.* 370 (2011) 1-22.
- [5] B. Tarboush, D. Rana, T. Matsuura, H. Arafat, R. Narbaitz, *J. Membr. Sci.* 325 (2008) 166-175.
- [6] L. Li, S. Zhang, X. Zhang, G. Zheng, *J. Membr. Sci.* 289 (2007) 258-267.
- [7] S. Peng, L. Peng, C. Yi, W. Zhang, X. Wang, *J. Polym. Sci., Part A: Polym. Chem.* 56 (2018) 959-967.
- [8] J. Chen, C. Gong, C. Yang, C. Yi, *J. Mater. Sci.* 56 (2021) 12018-12029.
- [9] T.-S.N. Chung, *Fabrication of Hollow-Fiber Membranes by Phase Inversion, Advanced Membrane Technology and Applications 2008*, pp. 821-839.
- [10] P.R. Saunders, *J. Polym. Sci.* 57 (1962) 131-139.
- [11] M.A. Aroon, A.F. Ismail, M.M. Montazer-Rahmati, T. Matsuura, *Sep. Purif. Technol.* 72 (2010) 194-202.
- [12] P.R. Saunders, *J. Polym. Sci.* 43 (1960) 273-275.
- [13] D. Hou, H. Fan, Q. Jiang, J. Wang, X. Zhang, *Sep. Purif. Technol.* 135 (2014) 211-222.
- [14] A. Idris, I. Ahmed, *J. Appl. Polym. Sci.* 108 (2008) 302-307.
- [15] I. Alghoraibi, *Int. J. Chemtech Res.* 7 (2014) 20-27.
- [16] N. Li, Y. Hu, Y.-Z. Lu, R.J. Zeng, G.-P. Sheng, *Sci. Rep.* 6 (2016) 26115.
- [17] O. Chavalparit, M. Ongwandee, *J. Environ. Sci.* 21 (2009) 1491-1496.
- [18] S. Opricovic, G.-H. Tzeng, *Eur. J. Oper. Res.* 156 (2004) 445-455.
- [19] M. Behzadian, R.B. Kazemzadeh, A. Albadvi, M. Aghdasi, *Eur. J. Oper. Res.* 200 (2010) 198-215.
- [20] G.E. Box, N.R. Draper, *Empirical Model-building and Response Surfaces*, John Wiley & Sons, New York (1987).
- [21] A.I. Khuri, S. Mukhopadhyay, *WIREs Comput. Stat.* 2 (2010) 128-149.
- [22] A. Abdulrahman, A. Ali, A. Alfazazi, *Arab. J. Sci. Eng.* 46 (2021) 6609-6617.
- [23] R. Lin, G. Yin, *Contemp. Clin. Trials* 44 (2015) 33-35.
- [24] S.E.I. Lebouachera, M.A. Ghriga, G.B. Salha, H.E. Hadri, M. Hasanzadeh, N. Drouiche, S. Reynaud, B. Grassl, *J. Polym. Res.* 28 (2021) 135.
- [25] H. Abadikhah, F. Zokaei Ashtiani, A. Fouladitajar, *Desalination Water Treat.* 56 (2015) 2783-2796.
- [26] N. Lashari, T. Ganat, D. Otchere, S. Kalam, I. Ali, *J. Pet. Sci. Eng.* 205 (2021) 108800.
- [27] D. Asante-Sackey, S. Rathilal, L. V. Pillay, E. Kweinor Tetteh, *Processes* 8 (2020) 160.

ABULHASSAN ALI  
KHURAM MAQSOOD  
AYMN ABDULRAHMAN  
AHMAD S. ALSAADI  
ABDULLAH BIN MAHFOUZ

Department of Chemical  
Engineering, University of Jeddah,  
Jeddah, Saudi Arabia

NAUČNI RAD

## OPTIMALNO RASTVARANJE I VISKOELASTIČNO PONAŠANJE POLIAMIDA-66 U MRAVLJOJ KISELINI ZA IZRADU MEMBRANA

*Tehnologija polimernih membrana visokih performansi se brzo razvija širom sveta sa uvođenjem novih materijala i procesa. Ulažu se značajni istraživački napor da se napravi polimerna membrana koja se može koristiti za ultrafiltraciju (UF) ili nanofiltraciju (NF). Razvoj modifikovanog polimera na bazi poliamid-66 i njegova kompatibilnost sa otpadnim vodama su suštinski elementi u potrazi za napretkom i poboljšanjima u membranskoj tehnologiji. Optimizovani uslovi za sintezu membrane su kritični za njenu komercijalnu održivost. Metodologija površine odgovora (RSM) je korišćena da se pronađe optimalno rastvaranje poliamida-66 u mravljoj kiselini. Model je razvijen i validiran eksperimentalnim podacima, koji je pokazao dobro slaganje ( $R^2 = 0,998$ ). Određen je optimizovan uslov za minimiziranje viskoznosti. Za minimalni viskozitet (3,64 cP), optimalna temperatura je 20 °C, a mas. % 0,6.*

*Ključne reči: optimizacija, poliamid-66, polimerna membrana, RSM, viskoznosti.*



MIA RADONJIĆ<sup>1,2,\*</sup>  
JELENA PETROVIĆ<sup>1,2,\*</sup>  
MILENA MILIVOJEVIĆ<sup>3</sup>  
MILENA STEVANOVIĆ<sup>3,4,5</sup>  
JASMINA STOJKOVSKA<sup>1,2</sup>  
BOJANA OBRADOVIĆ<sup>1</sup>

<sup>1</sup> University of Belgrade, Faculty of Technology and Metallurgy, Belgrade, Serbia

<sup>2</sup> Innovation Center of the Faculty of Technology and Metallurgy, Serbia

<sup>3</sup> University of Belgrade, Institute of Molecular Genetics and Genetic Engineering, Belgrade, Serbia

<sup>4</sup> University of Belgrade, Faculty of Biology, Belgrade, Serbia

<sup>5</sup> Serbian Academy of Sciences and Arts, Belgrade, Serbia

\* Authors contributed equally to this work

SCIENTIFIC PAPER

UDC 66.02:616-006.6:51

## CHEMICAL ENGINEERING METHODS IN ANALYSES OF 3D CANCER CELL CULTURES: HYDRODYNAMIC AND MASS TRANSPORT CONSIDERATIONS

### Article Highlights

- Chemical engineering methods provide explanations for experimental findings in 3D cell cultures
- Shear stress levels of  $\sim 70$  mPa may induce cell death in 3D glioma cell cultures
- Perfusion enhanced proliferation of C6 glioma cells in microfibers as compared to static controls
- Perfusion is necessary for the mass transport of molecules with low diffusivities of  $\sim 10^{-19}$  m<sup>2</sup> s<sup>-1</sup>

### Abstract

*A multidisciplinary approach based on experiments and mathematical modeling was used in biomimetic system development for three-dimensional (3D) cultures of cancer cells. Specifically, two cancer cell lines, human embryonic teratocarcinoma NT2/D1 and rat glioma C6, were immobilized in alginate microbeads and microfibers, respectively, and cultured under static and flow conditions in perfusion bioreactors. At the same time, chemical engineering methods were applied to explain the obtained results. The superficial medium velocity of  $80 \mu\text{m s}^{-1}$  induced lower viability of NT2/D1 cells in superficial microbead zones, implying adverse effects of fluid shear stresses estimated as  $\sim 67$  mPa. On the contrary, similar velocity ( $100 \mu\text{m s}^{-1}$ ) enhanced the proliferation of C6 glioma cells within microfibers compared to static controls. An additional study of silver release from nanocomposite Ag/honey/alginate microfibers under perfusion indicated that the medium partially flows through the hydrogel (interstitial velocity of  $\sim 10$  nm s<sup>-1</sup>). Thus, a diffusion-advection-reaction model described the mass transport to immobilized cells within microfibers. Substances with diffusion coefficients of  $\sim 10^{-9}$ - $10^{-11}$  m<sup>2</sup> s<sup>-1</sup> are sufficiently supplied by diffusion only, while those with significantly lower diffusivities ( $\sim 10^{-19}$  m<sup>2</sup> s<sup>-1</sup>) require additional convective transport. The present study demonstrates the selection and contribution of chemical engineering methods in tumor model system development.*

*Keywords: tumor engineering, alginate hydrogel, perfusion bioreactor, mathematical modeling, glioma C6 cell line, embryonic teratocarcinoma NT2/D1 cell line.*

Cancer is the second leading cause of death

worldwide; searching for its cure is one of the most important challenges in the 21<sup>st</sup> century (over 19 million new cases in 2020 [1]). One of the underlying problems is the complex and slow development of new anticancer drugs, which traditionally rely on two-dimensional (2D) cell cultures followed by *in vivo* studies on animals. However, 2D cultures have many limitations, including different cell morphology, polarity, duplication time, and absence of interactions with extracellular components [2]. Thus, 2D cell cultures fail

Correspondence: B. Obradović, University of Belgrade, Faculty of Technology and Metallurgy, Karnegijeva 4, 11000 Belgrade, Serbia.

E-mail: [bojana@tmf.bg.ac.rs](mailto:bojana@tmf.bg.ac.rs)

Paper received: 7 June, 2021

Paper revised: 7 September, 2021

Paper accepted: 17 September, 2021

<https://doi.org/10.2298/CICEQ210607033R>

to adequately simulate the complexity of the tumor microenvironment *in vivo*, which involves three-dimensional (3D) structures and extracellular matrix (ECM), allowing cell-cell and cell-ECM interactions that control tumor growth and progression [3]. These substantial interactions are absent in 2D cell cultures, frequently leading to inconsistencies in the efficacies of anticancer drugs observed *in vitro* compared to the results obtained in clinical trials [4]. On the other hand, animal models in preclinical trials often produce misleading results due to native interspecies differences [5]. Hence, there is an emerging necessity for developing more relevant 3D *in vitro* tumor models, which would mimic the tumor microenvironment and provide a more accurate translation of the results to *in vivo* settings. In addition, reliable 3D *in vitro* tumor models could significantly reduce animal testing and serve as consistent systems for investigations and development of novel anticancer drugs.

However, transitioning from 2D to 3D cell culture models goes hand in hand with the increase in system complexity, which requires multidisciplinary approaches. Applying chemical engineering principles in developing *in vitro* tumor model systems has already shown undeniable potential. Mathematical modeling can analyze and better understand tumor behavior in growth, progression, and invasion [6-8]. Additionally, model-based predictions can be used to evaluate the effects of anticancer drugs [7-9]. One of the approaches in tumor engineering relies on the tissue engineering strategy based on the integrated use of scaffolds for cell attachment and support and biomimetic bioreactors providing efficient mass transport and adequate physical signals [10]. In this approach, chemical engineering principles arise as a powerful tool for insight into the underlying phenomena and overcoming experimental trial-and-error methodology in system optimization [11-14].

This work shows the potential of applying chemical engineering principles to analyze experimental results to gain more accurate insights into the mechanisms occurring in our 3D *in vitro* systems for cancer cell culture. Specifically, two types of cancer cells were cultured in a biomimetic 3D system consisting of alginate hydrogels as cell carriers and perfusion bioreactor. Alginate was chosen due to its biocompatibility, immunogenicity, and non-toxicity [15]. In the presence of multivalent cations, *e.g.*,  $\text{Ca}^{2+}$ , alginate solutions undergo rapid and mild gelation forming hydrogels that can be produced in different shapes (beads, fibers, and films) and sizes (*e.g.* [16,17]). Due to its structural similarity to native ECMs of soft tissues, alginate hydrogels have been widely

used in wound dressings, controlled drug delivery systems, *in vitro* cell cultures, and tissue engineering [15]. In tumor engineering, alginate-based scaffolds in different forms support cell viability and proliferation *in vitro* [18] and cell conversion to more malignant *in vivo*-like phenotypes compared to 2D cultures [19-21]. *In vivo*, alginate-based scaffolds supported tumor growth and blood vessel recruitment [19,20]. Also, this type of cell carrier induced the formation of multicellular tumor spheroids *in vitro* [22-26] that retained high cell viability [22], increased invasion and metastatic potential [23], and higher expression of tumor angiogenesis biomarker [25] than cells in 2D cultures. Furthermore, alginate-based 3D tumor models showed increased resistance to anticancer drugs than monolayer cultures indicating a closer resemblance to the natural tumor environment [20,23,25].

Contrary to the cells grown in the monolayer having unlimited access to the ingredients of the medium, the supply of oxygen and nutrients to the cells in 3D tumor models may become critically limited. Thus, perfusion bioreactors have been occasionally applied to improve mass transport to and from cultivated cells by laminar flow of the medium at physiological velocities directly through a scaffold with cells. The increased cell viability and proliferation under 3D perfusion conditions as opposed to static cultures were reported for several cancer cell lines and cancer spheroid models [27-29]. Furthermore, 3D perfusion systems supported structural maintenance of cancer tissue *in vitro* [30-32]. Several studies reported significantly altered biological responses to anticancer therapies of tumor cultures grown under perfusion conditions compared to standard 2D monolayer cultures, thus suggesting 3D perfusion systems as more relevant *in vitro* models for testing cancer sensitivity to drugs [28,29,32-34]. Still, medium flow in perfusion systems induces hydrodynamic shear stresses on exposed cells and scaffold surfaces, possibly causing negative effects. For example, fluid flow in collagen gels loaded with glioma cells induced compaction of the gels while suppressing the migratory activity of U87 and CNS-1 glioma cell lines proportionally to the shear stress level and duration of shear stress exposure [35]. Shear stresses of magnitudes above 1 Pa induced cell death in monolayers of differentiated human neuroblastoma SH-SY5Y cells characterized by DNA fragmentation [36] and a monolayer of a human hepatocellular liver carcinoma HepG2 cell line [37]. In a study of circulating metastatic breast cancer cells (MDA-MB-231), shear stresses of 0.5 and 2 Pa decreased viability of individual cells and induced disaggregation of cell clusters [38]. Interestingly, based on these results and findings published in the literature, the authors concluded that



shear stress levels inducing death of circulating tumor cells might, at the same time, increase the aggressiveness of the surviving cells by fostering cell capabilities for migration and adhesion to metastatic sites [38]. Thus, in 3D culture systems, the flow rate has to be optimized to provide efficient mass transport at acceptable shear stress levels, which may vary depending on the cell type. Therefore, chemical engineering analysis of hydrodynamic and mass transport conditions is the subject matter, which can provide directions to optimize system parameters (*e.g.*, flow rate, scaffold size, and geometry). In addition, these analyses offer possibilities to identify critical factors (*e.g.*, shear stress, limiting nutrient or active substance) affecting the cells in a 3D culture to correlate the cell microenvironment with the observed effects (*e.g.*, cell viability, metabolic activity, proliferation rate).

In this work, we conducted two independent experiments using two forms of alginate hydrogels and a perfusion bioreactor and applied chemical engineering principles to analyze the obtained results. In addition, a separate experimental study with nanocomposite Ag/honey/alginate microfibers was conducted to determine mass transport mechanisms under perfusion. Then, hydrodynamic shear stresses were determined, and mass transport modeling was applied to elucidate the experimentally observed effects of cultivation conditions on the cultured cancer cells.

## MATERIALS AND METHODS

### Materials

Low viscosity sodium alginate (A3249) was supplied from AppliChem (Germany). Two batches of acacia honey from different suppliers (Azad.o.o., S. Ledinci, Serbia and Venenum Apis, Smedervska Palanka, Serbia) were used for the synthesis of silver nanoparticles (AgNPs). Silver nitrate ( $\text{AgNO}_3$ ) was purchased from Pliva (Zagreb, Croatia). Dulbecco's modified Eagle's medium (DMEM,  $4.5 \text{ g dm}^{-3}$  glucose), fetal bovine serum (FBS), and Penicillin-Streptomycin-Amphotericin B solution (Pen-Strep-Ampho. B) were supplied from Biological Industries (Israel). Calcium chloride dihydrate ( $\text{CaCl}_2 \cdot 2\text{H}_2\text{O}$ ) was provided by Acros Organics (USA). Phosphate-buffered saline (PBS), calcium nitrate tetrahydrate ( $\text{Ca}(\text{NO}_3)_2 \cdot 4\text{H}_2\text{O}$ ), sodium citrate dihydrate ( $\text{Na}_3\text{C}_6\text{H}_5\text{O}_7 \cdot 2\text{H}_2\text{O}$ ), sodium hydroxide (NaOH), L-glutamic acid, Trypsin/EDTA, Trypan Blue solution, and methylthiazolyldiphenyl-tetrazolium bromide (MTT) were all purchased from Sigma-Aldrich (USA). LIVE/DEAD™ Cell Imaging Kit was supplied from Thermo Fisher Scientific (Waltham,

MA, USA).

### Cell lines

The rat glioma cell line C6 (ATCC® CCL-107™) and the human embryonic teratocarcinoma cell line NTERA-2 cl.D1 (also known as NT2/D1; ATCC® CRL-1973™; a kind gift from Prof. Peter W. Andrews, University of Sheffield, UK) were maintained in the culture medium (DMEM supplemented with 10% FBS, 2 mM L-glutamine, and 1% Pen-Strep-Ampho.B). The cultures were incubated at 37 °C in a fully humidified atmosphere with 5%  $\text{CO}_2$  (C6 cells) or 10%  $\text{CO}_2$  (NT2/D1 cells).

When the confluence of about 90% was reached, cells were detached using 0.25% Trypsin /1mM EDTA. In brief, cells in 10 cm Petri dishes were washed with  $5 \text{ cm}^3$  1xPBS, treated with  $1 \text{ cm}^3$  Trypsin /EDTA for 5 min at 37 °C, after which Trypsin /EDTA was neutralized with DMEM.

### Cell immobilization in alginate hydrogels

Two different independent experiments were conducted. In Experiment 1, NT2/D1 cells were immobilized in alginate microbeads, while in Experiment 2, C6 cells were immobilized in alginate microfibers. Alginate microbeads and microfibers were produced as follows: sodium alginate powder was dissolved in distilled water at 2% w/w and 3.5% w/w, respectively, and the obtained solutions were sterilized by boiling for 30 min. Before immobilization, cells were detached using Trypsin/EDTA (as described above) and counted using a hemocytometer.

#### *Immobilization of NT2/D1 cells in alginate microbeads (Experiment 1)*

A suspension of NT2/D1 cells was mixed with 2% w/w sodium alginate solution to obtain final concentrations of 1.3% w/w alginate and  $1 \times 10^6$  cells  $\text{cm}^{-3}$ . Alginate microbeads with the immobilized NT2/D1 cells were produced by electrostatic droplet generation (4.3 kV electrostatic potential, 2.5 cm electrode distance), using a blunt edge needle (28 G, Small Parts Inc., USA), a flow rate of  $25.2 \text{ cm}^3 \text{ h}^{-1}$ , and a gelling solution containing  $\text{Ca}^{2+}$  (0.18 M  $\text{CaCl}_2 \cdot 2\text{H}_2\text{O}$ ), as described previously [39]. The obtained microbeads were left in the gelling solution for 15 min to complete gelling and subsequently washed with the culture medium. The microbeads were further placed into the fresh medium and cultivated for the next 24 h under static conditions in a humidified incubator at 10%  $\text{CO}_2$  and 37 °C.

#### *Immobilization of rat glioma C6 cells in alginate microfibers (Experiment 2)*

A suspension of rat glioma C6 cells was mixed

with 3.5 % w/w sodium alginate solution to obtain final concentrations of 2.8 % w/w alginate and  $8 \times 10^6$  cells  $\text{cm}^{-3}$ . Alginate microfibers with immobilized C6 cells were produced by manual extrusion of the obtained suspension through a blunt edge stainless steel needle (25 G, Small Parts Inc., USA) immersed in the gelling solution containing  $\text{Ca}^{2+}$  (0.18 M  $\text{Ca}(\text{NO}_3)_2 \cdot 4\text{H}_2\text{O}$ ). The resulting microfibers were left in the gelling solution for 15 min to complete gelling. After washing with the culture medium, the microfibers were placed into the fresh medium and cultivated for the next 8 days under static conditions in a humidified incubator at 5%  $\text{CO}_2$  and 37 °C. Specifically, 0.5 g of microfibers were maintained in 15  $\text{cm}^3$  medium, while 40% of the medium was replaced every 4<sup>th</sup> day.

### Cultivation of immobilized cells in perfusion bioreactors

#### *Bioreactor cultivation of microbeads with immobilized NT2/D1 cells*

A perfusion bioreactor system used to cultivate alginate microbeads with immobilized NT2/D1 cells consisted of a chamber, two 3-way stopcocks, a medium reservoir, and a silicone tubing loop as described previously [40]. In the present experimental setup, 0.5 g of wet microbeads with immobilized NT2/D1 cells, 24 h after immobilization, was placed in the bioreactor chamber (0.8 cm inner diameter, 1.5 cm height) formed by a piece of silicone tubing, and the system was filled with 11  $\text{cm}^3$  of the culture medium. Three perfusion systems were set up and placed in the incubator at 37 °C and fully humidified atmosphere with 10%  $\text{CO}_2$ . The flow rate of 0.25  $\text{cm}^3 \text{min}^{-1}$ , which corresponded to the superficial velocity of 80  $\mu\text{m s}^{-1}$ , was provided by a multichannel peristaltic pump (Masterflex, Cole-Parmer, IL, USA) placed outside the incubator. The static culture comprising 3 Petri dishes with 0.5 g of wet microbeads with immobilized NT2/D1 cells in 11  $\text{cm}^3$  of the culture medium, each, served as a control. The experiment lasted for 10 days, and 40% of the culture medium was changed twice a week.

#### *Bioreactor cultivation of microfibers with immobilized C6 cells*

The single-use perfusion bioreactor system “3D Perfuse” (Innovation Center of the Faculty of Technology and Metallurgy, Belgrade, Serbia) was used to cultivate alginate microfibers with immobilized rat glioma C6 cells. The system consisted of a chamber, two 3-way stopcocks, a medium reservoir, and a silicone tubing loop serving for gas exchange [41]. In the present experimental setup, 0.5 g of wet microfibers with the immobilized rat glioma C6 cells, cultured statically for 8 days, was placed in the

bioreactor chamber (0.8 cm inner diameter, 4 cm height) formed by a piece of silicone tubing and the system was filled with 15  $\text{cm}^3$  of the culture medium. Two perfusion systems were set up and placed in the incubator at 37 °C and fully humidified atmosphere with 5%  $\text{CO}_2$ . The flow rate of 0.30  $\text{cm}^3 \text{min}^{-1}$ , which corresponded to the superficial velocity of 100  $\mu\text{m s}^{-1}$ , was provided by a multichannel peristaltic pump (Masterflex, Cole-Parmer, IL, USA) placed outside the incubator. The static culture comprising 2 Petri dishes with 0.5 g of wet microfibers with immobilized C6 cells and 15  $\text{cm}^3$  of the culture medium served as a control. On the 4<sup>th</sup> day of the experiment, 40% of the culture medium was changed, while the experiment lasted for 5 days.

### Production of Ag/honey/alginate microfibers and silver release studies

AgNPs were obtained by chemical reduction of silver ions in aqueous solutions of two batches of honey, as described previously [42]. In brief, honey was dissolved in distilled water at the final concentration of 50% w/w. Then, silver nitrate was added to the solution to achieve the final concentration of silver of 3.9 mM. Next, 1 M NaOH was added dropwise to initiate the reduction of  $\text{Ag}^+$  ions and to increase the pH value to 9. After achieving the desired pH value, the solution was left in the dark for 4 days and at room temperature. Next, the solution was mixed with the aqueous solution of sodium alginate to achieve final concentrations of 2.8% w/w alginate, 30% w/w honey, and 2.34 mM silver. The composite microfibers were produced by manual extrusion of the obtained solution into the gelling solution, containing  $\text{Ca}^{2+}$  (0.73 M  $\text{Ca}(\text{NO}_3)_2 \cdot 4\text{H}_2\text{O}$ ), through a blunt edge stainless steel needle (22 G, Small Parts Inc., USA) and were left in the gelling solution for 30 min to complete gelling. Finally, composite silver/honey/alginate microfibers were placed in distilled water and kept in the dark at 4 °C.

Silver release studies were performed in the same “3D Perfuse” perfusion system comprising 0.5 g of nanocomposite microfibers and 15  $\text{cm}^3$  of the culture medium in each recirculation loop. Three bioreactor systems for each time point were kept in the incubator at 37 °C and fully humidified atmosphere with 5%  $\text{CO}_2$  and continuously perfused at the flow rate of 0.25  $\text{cm}^3 \text{min}^{-1}$  corresponding to the superficial velocity of 80  $\mu\text{m s}^{-1}$ . The experiments lasted for 1, 2, 5, and 7 days, at which time points the medium was analyzed for silver concentration.

### Analytical methods

#### *Optical microscopy*

The average microbead diameter was determined using a DM IL LED Inverted Microscope (Leica Micro-

systems, Germany) from measurements of at least 20 microbeads using the Leica Application Suite V4.3.0 software. Images of LIVE/DEAD assays were taken by an Olympus BX51 Fluorescence Microscope (Olympus, Japan). An optical microscope Olympus Vanox (Olympus, Japan), was used for cell counting. The optical microscope Motic BA210 (Motic, China) connected to software for image analysis (Motic Images Plus 2.0) was used to measure microfiber diameters. The average microfiber diameter was determined from at least 10 measurements.

#### *Determination of cell density and viability*

A portion of microbeads/microfibers (0.2 - 0.3 g) was dissolved in 2% w/v sodium citrate solution at the hydrogel to a solution mass ratio of 1:5 to determine the number of viable cells in alginate hydrogels. Then, 100  $\mu\text{l}$  of the obtained cell suspension was mixed with 100  $\mu\text{l}$  of Trypan Blue solution, and the cells were counted after 5 min using a hemocytometer and an optical microscope. Finally, cell viability was calculated using the ratio of the number of unstained (viable) cells and the total cell count.

#### *Live/Dead Staining*

Cell viability in Experiment 1 was assessed by using a LIVE/DEAD™ Cell Imaging Kit (R37601, Thermo Fisher Scientific, USA) and staining according to the manufacturer's protocol. The kit discriminates live cells (green fluorescence) from dead cells (red fluorescence). Cells were visualized using an Olympus BX51 fluorescence microscope, a FITC filter for green fluorescence, and a Texas Red filter for a red fluorescence and analyzed using Cytovision 3.1 software (Applied Imaging Corporation, USA). All images were captured by using a 20x objective. In brief, 2-3 microbeads with immobilized NT2/D1 cells were transferred into a tube with 50  $\mu\text{l}$  of the culture medium and mixed with the equal volume of the Live Green/Dead Red solution. The samples were incubated for 20 min at room temperature and then transferred to microscope slides and immediately imaged.

#### *MTT assay*

The MTT assay was used at the end of Experiment 2 to assess cell viability within the microfibers. In brief, the MTT reagent was dissolved in PBS and then diluted to 0.5 mg  $\text{cm}^{-3}$  with the culture medium. Next, 0.1 g of microfibers was incubated with 1  $\text{cm}^3$  of the MTT solution in a 24 well plate, and the images of microfibers were taken after 15 h using an optical microscope.

#### *UV-vis spectroscopy*

UV-visible spectroscopy (model UV-3100, Mapada, China) was used to investigate the presence of AgNPs in the colloid solution and in the obtained nanocomposite microfibers as described previously [42].

#### *Silver concentration*

The initial silver concentration in microfibers was determined upon microfiber (0.1 g) dissolution in 2% w/v sodium citrate solution (3  $\text{cm}^3$ ), followed by the addition of 10  $\text{cm}^3$  of  $\text{NH}_4\text{OH}$  solution (25%). The culture medium samples were mixed with 25%  $\text{NH}_4\text{OH}$  in the volume ratio of 2:1 to oxidize potentially released AgNPs and dissolve precipitated AgCl. At the same time, perfusion loops and Petri dishes were rinsed with the same alkaline solution. Finally, silver concentration in all obtained solution samples was determined by atomic absorption spectroscopy (AAS) using an Agilent Technologies 240FS AA spectrophotometer (Agilent Technologies, USA).

## RESULTS AND DISCUSSION

### **Cultivation of alginate microbeads with immobilized NT2/D1 cells**

Microbeads with immobilized NT2/D1 cells were obtained by electrostatic extrusion of the cell suspension in sodium alginate ( $1 \times 10^6$  cells  $\text{cm}^{-3}$  and 1.3% w/w sodium alginate). The average diameter of the resulting microbeads was  $310 \pm 20$   $\mu\text{m}$ , while the immobilized cell concentration was  $2.3 \times 10^6$  cells  $\text{cm}^{-3}$ . The increase in the cell concentration after immobilization could be explained by the syneresis of alginate gel during gelation, as reported previously for the production of nanocomposite Ag/alginate microbeads [43,44].

NT2/D1 cells immobilized in alginate microbeads were cultivated under continuous perfusion at the flow rate of 0.25  $\text{cm}^3 \text{min}^{-1}$  (superficial velocity of 80  $\mu\text{m s}^{-1}$ ) for 10 days. At the end of the experiment, the microbead diameter slightly increased in the bioreactor ( $360 \pm 30$   $\mu\text{m}$ ) and the static culture ( $370 \pm 30$   $\mu\text{m}$ ). However, it was impossible to accurately determine the cell concentration within microbeads due to the adverse effects of the alginate dissolution process by the citrate solution. Yet, to get an insight into the cell viability, the microbeads were stained with the LIVE/DEAD Cell Imaging Kit, which revealed higher cell viability in the static culture (Fig. 1a) than the bioreactor culture (Fig. 1b). Furthermore, the immobilized cells were metabolically active in the core of microbeads in the bioreactor while inactive in the superficial microbead zone. These results indicate that mass transport in the

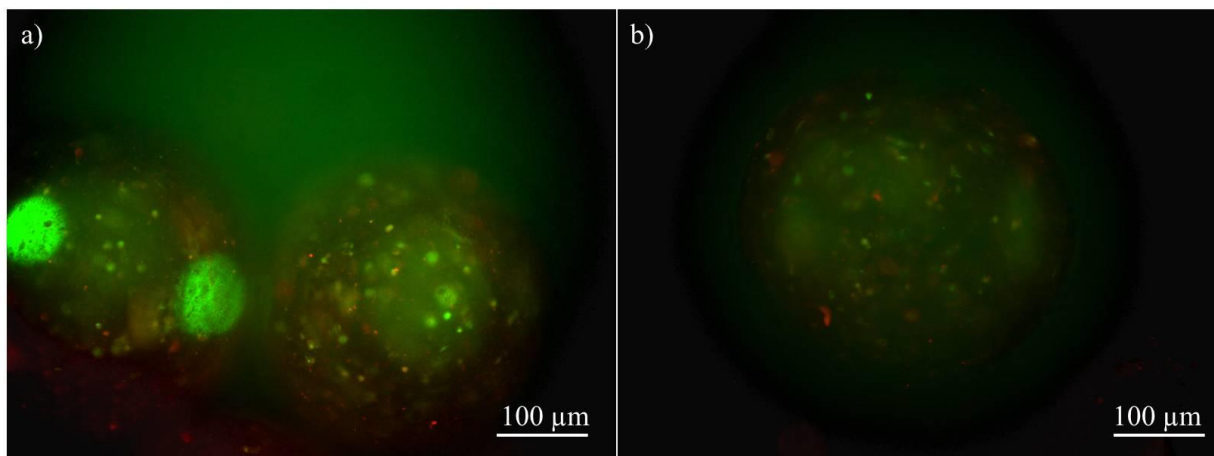


Figure 1. Fluorescence microscopy LIVE/DEAD Cell Imaging of NT2/D1 cells in microbeads after 10-day cultivation under a) static conditions; b) continuous perfusion in the perfusion bioreactor (scale bar: 100  $\mu\text{m}$ ); live cells (green), dead cells (red).

static culture and, therefore, in the bioreactor culture was sufficient to support cell viability. On the other hand, the adverse effects in the microbead superficial zones in the bioreactor culture could be thus attributed to shear stresses generated by the medium flow through the packed bed, which negatively influenced the cells.

#### Calculation of hydrodynamic shear stresses in the bioreactor with the packed bed of alginate microbeads

The well-known Carman - Kozeny equation was used to calculate the pressure drop per bed height ( $\Delta P/H$ ) to quantify the effects of shear stresses in the perfusion bioreactor. This equation was recommended for laminar flow in packed beds in a circular channel [45] and was applied for the packed bed of alginate microbeads as:

$$-\frac{\Delta P}{H} = 180 \frac{(1-\varepsilon)^2}{\varepsilon^3} \frac{\mu}{d_p^2} U \quad (1)$$

where  $\varepsilon$  is the packed bed porosity,  $\mu$  is the fluid viscosity,  $d_p$  is the particle diameter, and  $U$  is the superficial liquid velocity. The particle diameter value of 335  $\mu\text{m}$  was used, corresponding to the average microbead diameter in the bioreactor culture at the beginning end of the present experiment. The bed porosity was calculated as 0.27, considering the microbead mass (0.5 g) and the chamber volume. The viscosity of the cell medium was adopted as  $9.4 \times 10^4 \text{ Pa}\cdot\text{s}$  [46]. At the experimental superficial medium velocity of  $80 \mu\text{m s}^{-1}$ , the pressure drop was calculated as  $3266 \text{ Pa m}^{-1}$  by applying Eq. (1). This value was further used for calculation of the shear stress ( $\tau$ ) to which the microbeads were exposed as [45]:

$$\tau = \frac{\varepsilon}{S_v(1-\varepsilon)} \left( -\frac{\Delta P}{H} \right) \quad (2)$$

where  $S_v$  is the specific surface area of the particle. For the adopted microbead diameter,  $S_v$  was calculated as  $1.8 \times 10^4 \text{ m}^2 \text{ m}^{-3}$ , yielding the shear stress value of 67 mPa.

Cancer cells can be exposed to shear stresses generated by the blood flow, which affects circulating tumor cells, and the interstitial fluid flow in the ECM, influencing the cells of a growing tumor [47]. Qazi *et al.* [35] calculated the shear stress in brain tumors as 9 - 68 mPa based on the experimentally measured fluid velocities previously reported. Moreover, in the same work, it was shown that the shear stress of 55 mPa applied for 4 h practically diminished the migratory activity of the glioma cell line U87 and highly suppressed that of the CNS-1 glioma cell line. Still, it did not affect the U251 glioma cell line. At the same time, the adverse effects of the applied shear stress on the cell viability were not observed [35]. However, the calculated shear stress value in the present study is on the upper limit of the reported physiological range. Furthermore, it was constantly applied for 10 days, so it could be assumed that observed cell death in microbead superficial zones is caused by the applied shear stress.

#### Cultivation of alginate microfibers with immobilized rat glioma C6 cells

Microfibers ( $440 \pm 40 \mu\text{m}$  in diameter) with immobilized rat glioma C6 cells were obtained by manual extrusion of the cell suspension in sodium alginate. The cell concentration was  $2.5 \times 10^6 \text{ cells cm}^{-3}$  24 h after immobilization, significantly lower than the initial concentration in the suspension due to the cell loss in the foam formed during the mixing and extrusion

of the suspension. The obtained microfibers were then cultured in culture dishes under static conditions for 8 days, after which period the cell concentration was determined as  $1.5 \times 10^6$  cells  $\text{cm}^{-3}$ . The decrease in cell concentration might be caused by microfiber swelling to the average diameter of  $540 \pm 50$   $\mu\text{m}$  or might be the result of some adverse effects of cultivation conditions.

The microfibers were cultured in perfusion bioreactors for the next 5 days, parallel with static cultures that served as a control. The microfiber diameters did not further change significantly as compared to the starting value, being  $570 \pm 120$   $\mu\text{m}$  and  $520 \pm 100$   $\mu\text{m}$  under perfusion and static conditions, respectively. On the contrary, cell counting at the end of the experiment has shown that the applied flow rate of  $0.30$   $\text{cm}^3$   $\text{min}^{-1}$  (superficial velocity of  $100$   $\mu\text{m}$   $\text{s}^{-1}$ ) enhanced cell proliferation yielding the cell concentration of  $8.8 \times 10^6$  cells  $\text{cm}^{-3}$ . On the other hand, the cell concentration in microfibers cultivated under static conditions just slightly increased to  $1.7 \times 10^6$  cells  $\text{cm}^{-3}$  compared to the initial cell concentration (*i.e.*,  $1.5 \times 10^6$  cells  $\text{cm}^{-3}$ ). It should be noted that cell viability was  $\sim 100\%$  in both cultures. The MTT assay applied directly to the microfibers further

confirmed high cell viability and metabolic activity (Fig. 2).

Although the cells stayed viable and metabolically active in both cultures (Fig. 2), cell proliferation was enhanced only under continuous medium flow, which in this case induced positive effects on the cells. It should be noted that the direct comparison of these results with Experiment 1 is not possible due to differences in the cell type, hydrogel form, and medium flow rate. However, a comparison of the results obtained in the static and bioreactor cultures in Experiment 2 implies that the static culture was mass transfer limited regarding some nutrient or bioactive molecule. Therefore, two hypotheses for limiting substances were tested, namely: i) oxygen, as usually considered, a rate-limiting factor for the proliferation of cancer cells (*e.g.*, [48,49]), and ii) a larger bioactive molecule (*e.g.*, proteins, hormones, or growth factors) present in FBS that could trigger the cell proliferation if efficiently supplied (as under perfusion). In the second case, transferrin was selected as a model molecule due to its significant role in the metabolism of cancer cells as a transporter of iron, possibly facilitating cell proliferation [50].

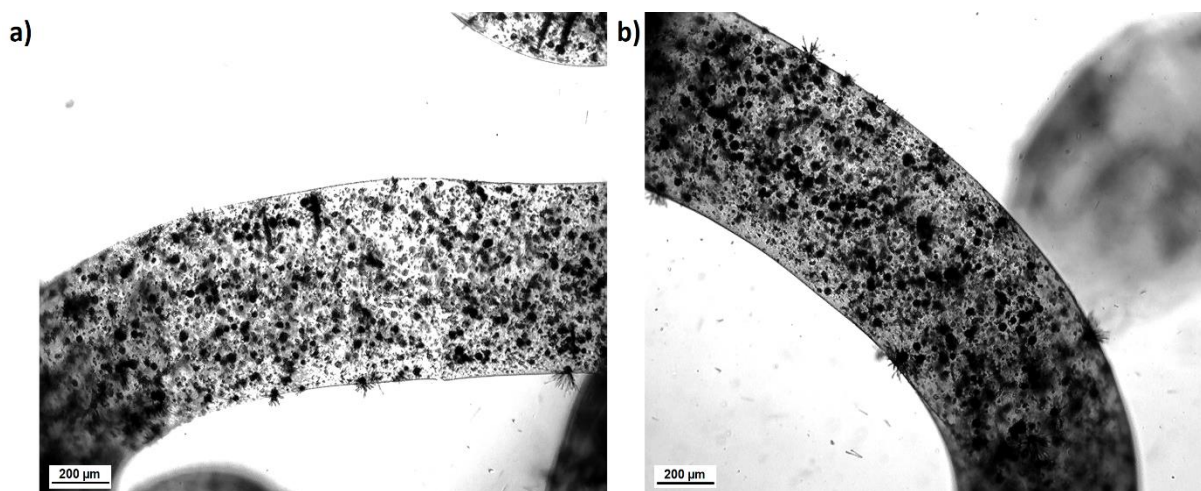


Figure 2. Optical micrographs of MTT-stained microfibers cultivated for 13 days in total: a) under static conditions; b) under static conditions for 8 days followed by 5 days under continuous perfusion (scale bar:  $200$   $\mu\text{m}$ ). Dark dots indicate purple formazan crystals formed by enzymatic reduction of the tetrazolium dye MTT in viable cells.

### Mathematical modeling of mass transport in the fibrous bed bioreactor

#### Mass transport without consumption

Mathematical modeling of mass transport in the fibrous bed bioreactor was founded on the assumption that the internal transport through the microfibers is rate-limiting and that the external mass transfer resistance to the microfiber surfaces is negligible. In addition, based on the observation of the effects of the medium flow on NT2/D1 cells within alginate

microbeads in Experiment 1 and the previous modeling studies of the silver release from the nanocomposite Ag/alginate microbeads [44], it was assumed that a small fraction of the medium flow is passing through the microfibers, thus increasing the internal mass transport rate compared to diffusion only, present in the static culture. Therefore, the experiments were performed with Ag/honey/alginate microfibers to determine silver

release mechanisms and the interstitial flow through the microfibers under continuous perfusion. The same approach was conducted in the previous silver release study from the packed bed of Ag/alginate microbeads [44]. In brief, the produced Ag/honey/alginate microfibers using two batches of honey had statistically similar diameters (average  $670 \pm 140 \mu\text{m}$ ) and silver concentrations (average  $2.9 \pm 0.4 \text{ mM}$ ) as determined by AAS. At the same time, the presence of AgNPs was confirmed by UV-vis spectroscopy (Fig. 1S, Supplementary material). Furthermore, over 7 days under perfusion at the superficial velocity of  $80 \mu\text{m s}^{-1}$ , silver release deviated from Fick's law of diffusion and was modeled by a diffusion-advection equation. Specifically, the nanocomposite microfiber bed was modeled as a compact hydrogel cylinder, 3 cm in length (based on experimental measurements of the bed height). It was assumed that the AgNP oxidation is faster than the mass transport of silver species through the hydrogel so that the change of silver concentration,  $c_s$ , in the cylindrical hydrogel over time is described by the diffusion-advection equation in the axial direction,  $x$ :

$$\frac{\partial c_s}{\partial t} = D_s \left( \frac{\partial^2 c_s}{\partial x^2} \right) - u \frac{\partial c_s}{\partial x} \quad (3)$$

where  $D_s$  is the apparent silver diffusion coefficient (of AgNPs,  $\text{Ag}^+$  and formed  $\text{AgCl}_x^{(x-1)-}$  species) in the alginate hydrogel adopted as  $2.1 \times 10^{-15} \text{ m}^2 \text{ s}^{-1}$  [51] and  $u$  is the medium velocity through the hydrogel. Silver concentration in the medium,  $c_{sm}$ , at each time point is calculated then as:

$$c_{sm} = \frac{V(c_{s0} - \langle c_s \rangle)}{V_m} \quad (4)$$

where  $c_{s0}$  is the initial silver concentration in microfibers ( $2.9 \times 10^{-3} \text{ mol dm}^{-3}$  as the average measured concentration),  $\langle c_s \rangle$  is the average silver concentration in the hydrogel,  $V$  is the hydrogel volume (calculated as  $0.49 \text{ cm}^3$  based on the microfiber mass and the alginate density of  $1020 \text{ kg m}^{-3}$  [51]), and  $V_m$  is the medium volume ( $15 \text{ cm}^3$ ). A negligible silver concentration in the medium compared to that in the hydrogel was assumed so that the inlet silver concentration was set to 0. The Neumann boundary condition was set at the outlet boundary. The modeling approach is summarized in the Supplementary material. The numerical solution of the model equations yielded the predictions that agreed well with the experimentally measured silver concentrations in the culture medium (Fig. 3). It should be noted that large error bars at later days of silver release are due to higher AgCl deposition in the system at these times, inducing scattering of experimentally measured data. The medium interstitial velocity through the hydrogel was predicted to be  $10.2 \text{ nm s}^{-1}$ , which agrees with the previously determined value of

$4.6 \text{ nm s}^{-1}$  through Ag/alginate microbeads in a packed bed [44].

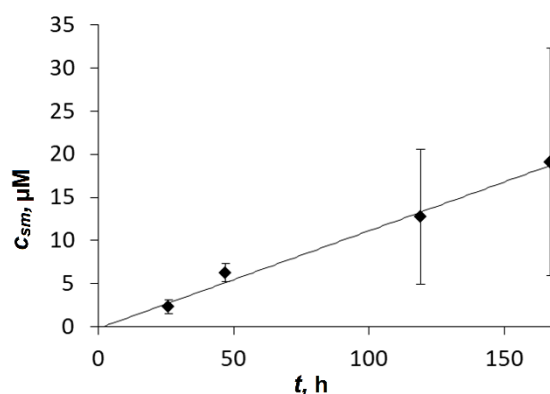


Figure 3. Released silver concentration from Ag/honey/alginate microfibers ( $c_{sm}$ ) as a function of time ( $t$ ) under perfusion: experimental data (symbols) and modeling results (lines) (data represent the average of  $n=3$ ).

#### Mass transport in the cell culture with the consumption term

Based on the obtained modeling results of silver release from packed beds of Ag/honey/alginate microfibers under perfusion, mass transport models were set to describe the transport of active substances within a single microfiber under cell culture conditions. Specifically, a model based on diffusion, advection, and reaction was set up to determine the concentration levels of different substances throughout a single microfiber under perfusion conditions. In contrast, a diffusion-reaction model was formulated to describe mass transport within a microfiber under static conditions. In both cases, the following assumptions were made:

1. the cylindrical geometry of the microfiber;
2. the constant microfiber diameter;
3. the constant consumption rate of the modeled substance per cell (zero-order chemical reaction);
4. the constant concentration of the modeled substance in the medium and thus at the microfiber surface;
5. mass transport only along the radial direction.

Therefore, the mass transport within a microfiber in the bioreactor culture was described by the diffusion-advection-reaction equation:

$$\frac{\partial c}{\partial t} = \frac{D}{r} \frac{\partial}{\partial r} \left( r \frac{\partial c}{\partial r} \right) - u \frac{\partial c}{\partial r} - \rho q \quad (5)$$

where  $D$  is the diffusion coefficient of the modeled substance,  $r$  is the radial coordinate from the microfiber center,  $q$  is the consumption rate of the substance per cell,  $\rho$  is the cell concentration per the microfiber volume, and  $u$  is the interstitial medium velocity within the microfiber in the radial direction.

The same equation describes the mass transport within a microfiber under static conditions with the omitted advective term:

$$\frac{\partial c}{\partial t} = \frac{D}{r} \frac{\partial}{\partial r} \left( r \frac{\partial c}{\partial r} \right) - \rho q \quad (6)$$

#### Initial and boundary conditions

Initial conditions depended on the modeled substance. In the case of oxygen, the initial concentration at time  $t = 0$  is uniform throughout the entire microfiber and is equal to the medium concentration,  $c_m$ :

$$t = 0 \quad 0 \leq r \leq R \quad c = c_m \quad (7)$$

where  $R$  is the microfiber radius. In the case of transferrin or other limiting substance present in the cell medium, the initial concentration in the microfiber is equal to zero that is:

$$t = 0 \quad 0 \leq r \leq R \quad c = 0 \quad (8)$$

The symmetry boundary condition was set along the microfiber axis that is:

$$r = 0 \quad \frac{dc}{dr} = 0 \quad (9)$$

At the outer microfiber boundary, a constant concentration equal to that in the medium ( $c_m$ ) was assumed:

$$r = R \quad c = c_m \quad (10)$$

#### Numerical solution

Partial differential equations (5) and (6) were solved numerically. The second concentration derivative was solved using the centered finite difference method, while for the first concentration derivative, the forward finite difference and backward finite difference methods were used.

#### Model parameters

The microfiber diameter was set to 540  $\mu\text{m}$ , which is the average value of all measured microfiber diameters before and after the static and bioreactor cultures.

The interstitial velocity of the culture medium within the microfiber under perfusion conditions ( $u$ ) was adopted as 10.2  $\text{nm s}^{-1}$  based on the experimental and mathematical modeling studies of silver release from nanocomposite Ag/alginate microfibers. The cell density in microfibers was set to the initial value of  $1.5 \times 10^6 \text{ cells cm}^{-3}$ .

#### Modeling of oxygen transport

The oxygen diffusion coefficient was set to  $D = 1.79 \times 10^{-9} \text{ m}^2 \text{ s}^{-1}$  as reported in the literature for the 3 wt.% alginate hydrogel [52], while a oxygen

concentration in the culture medium was adopted as  $0.18 \text{ mol m}^{-3}$  [53]. The oxygen consumption rate per cell for the C6 rat glioma cell line was reported to be  $12 \times 10^{-18} \text{ mol cell}^{-1} \text{ s}^{-1}$  [54].

Oxygen concentration profiles upon reaching a steady-state in both cultures are plotted as a function of the normalized radial distance concerning the microfiber radius (Fig. 4).

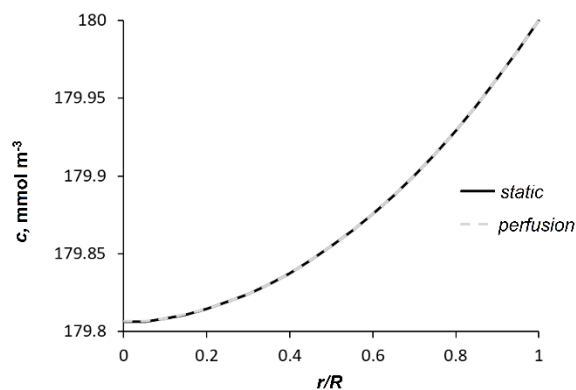


Figure 4. Oxygen concentration ( $c$ ) profiles as functions of the normalized radial distance within a microfiber ( $r/R$ ) upon reaching the steady-state under static and continuous perfusion conditions at the initial cell density of  $1.5 \times 10^6 \text{ cells cm}^{-3}$  ( $R$  is the microfiber radius;  $r/R=0$  designates the microfiber central axis, while  $r/R=1$  designates the microfiber outer surface).

In both cultures, the steady-state is reached almost immediately (after 73 s and 63 s in the static and bioreactor cultures, respectively) with the oxygen concentration in the center of the microfiber of 99.9% with respect to that in the culture medium. Thus, the modeling results imply efficient mass transport under both culture conditions, with diffusion being sufficient to fulfill the oxygen needs of the cells immobilized in alginate microfibers at the investigated density without any hypoxic regions. We have further modeled oxygen diffusion within microfibers with the final experimental cell density of  $8.8 \times 10^6 \text{ cells cm}^{-3}$  reached in the bioreactor culture only, and still transport by diffusion would be sufficient without visible effects of additional advective transport. In this case, the steady-state would be reached after 82 s in static and 78 s in bioreactor cultures, with the oxygen concentration in the microfiber center of 99.4% with regard to that in the medium in both cultures.

Thus, it could be assumed that static conditions could efficiently support the supply of gases and small molecules with diffusion coefficients of  $\sim 10^{-9} \text{ m}^2 \text{ s}^{-1}$  to the cells immobilized in alginate microfibers at the investigated cell density range up to  $\sim 9 \times 10^6 \text{ cells cm}^{-3}$ . Furthermore, the effects of advective mass transport, in this case, are negligible. Hence, the reason for

increased cell proliferation under medium flow conditions could be sought in the transport of a larger molecule.

### Modeling of transferrin transport

FBS is a complex natural product containing many various nutritional and bioactive components, including numerous types of proteins. Albumin is the most abundant protein in bovine serum, comprising 60–67% of total proteins, while transferrin is found at a fairly constant concentration ranging from 1.37 to 3.72 mg cm<sup>-3</sup> [55]. Transferrin was reported to play a significant role in the metabolism of cancer cells [50]. Moreover, the transferrin receptor 1 was found to participate in the regulation of glioma cell physiology, where the resulting iron accumulation and reactive oxygen species (ROS) formation facilitate the proliferation of these cells [50]. Therefore, we have assumed that the mass transport of transferrin may be an important parameter in 3D glioma cell cultures.

Transferrin serves as a transporter of iron to cells and, after internalization, is exocytosed back to the medium. The overall consumption rate of transferrin per cell was reported to be 2.6×10<sup>-22</sup> mol cell<sup>-1</sup> s<sup>-1</sup> [56]. Furthermore, the diffusion coefficient of transferrin in agarose gels was reported as 5.3×10<sup>-11</sup> m<sup>2</sup> s<sup>-1</sup> [57]. Finally, taking into account an average transferrin concentration in FBS of 2.5 mg cm<sup>-3</sup> diluted 10-fold in the culture medium, the transferrin medium concentration was adopted for modeling purposes as  $c_m = 3.1 \times 10^{-3}$  mol m<sup>-3</sup>.

Numerical solution of Eqs. (5) and (6) yielded the steady-state in static and bioreactor cultures after 36.2 and 35.7 min, respectively, reaching the transferrin concentration in the microfiber center of 99.98% with respect to that in the culture medium. Figure 5 shows transferrin concentration profiles in microfibers after 10 min in both cultures to illustrate slight differences in the transport rates before reaching the steady-state.

Based on the obtained results, it can be concluded that similarly as in the case of oxygen, the static conditions provide efficient transport of transferrin. Thus, the impact of advection on mass transport rates is negligible. Still, it should be noted that the transferrin molecule could interact with COO-groups [58], which are also present in alginate polymer chains. Therefore, these groups may be hindering the transferrin diffusion through the alginate hydrogel yielding a lower diffusion coefficient than the value used for mathematical modeling in this study. Moreover, alginate was used in a study of the controlled release of lactoferrin [59], a molecule with a similar sequence and

structure as transferrin, and coordinates iron identically [60]. In specific, when lactoferrin was adsorbed onto calcium phosphate nanoparticles further covered with chitosan and alginate layers, the *in vitro* release in PBS lasted over 10 h [59], implying a significantly lower release rate with the apparent diffusion coefficient of about 10<sup>-19</sup>–10<sup>-20</sup> m<sup>2</sup> s<sup>-1</sup>.

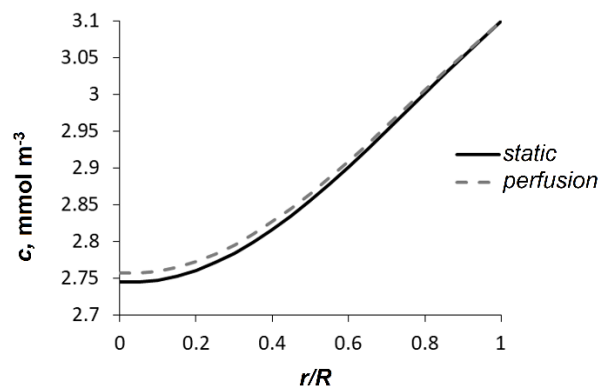


Figure 5. Predicted transferrin concentration ( $c$ ) profiles as functions of the normalized radial distance within a microfiber ( $r/R$ ) after 10 min under static and continuous perfusion conditions ( $R$  is the microfiber radius;  $r/R=0$  designates the microfiber central axis, while  $r/R=1$  designates the microfiber outer surface).

Therefore, we have checked the effects of a decreased diffusion coefficient in the investigated cultures in the next step. Figure 6 shows the modeling results of transferrin transport with the diffusion coefficient of  $D = 1 \times 10^{-19}$  m<sup>2</sup> s<sup>-1</sup>. In this case, advection is the dominant mass transport mechanism in the bioreactor culture. The transferrin concentration within the alginate microfiber in static cultures stayed approximately constant over 5 days due to the approximately equal diffusion and consumption rates (Fig. 6b). On the contrary, the transferrin concentrations in the microfiber in the bioreactor culture almost reached that existing in the medium after 7 h (Fig 6a). The obtained results suggest that the transferrin supply in static cultures may have been insufficient, leading to slow proliferation. In contrast, the advective transport compensated for slow diffusion in the bioreactor cultures. However, it is also possible that the transferrin apparent diffusion coefficient is between the values used in the present study and that a different substance with similar transport properties influenced the cell proliferation in our experiment. The modeling results indicate that substances with lower diffusion coefficients ( $D \sim 10^{-19}$  m<sup>2</sup> s<sup>-1</sup>) are transported very slowly under static conditions so that the convective mass transfer is necessary for efficient delivery.



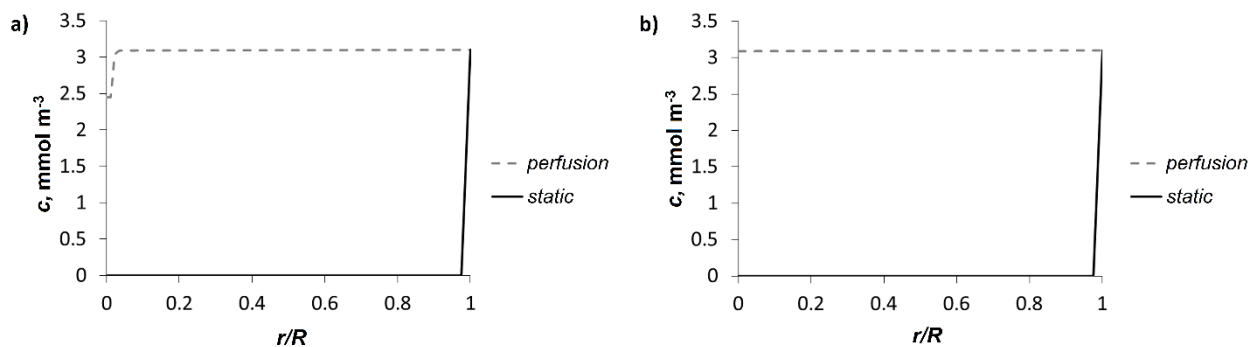


Figure 6. Predicted transferrin concentration ( $c$ ) profiles with a decreased diffusion coefficient of  $D = 1 \times 10^{-19} \text{ m}^2 \text{ s}^{-1}$  as functions of the normalized radial distance within a microfiber ( $r/R$ ) under static and continuous perfusion conditions: a) after 7 hours; b) after 5 days of cultivation ( $R$  is the microfiber radius;  $r/R=0$  designates the microfiber central axis, while  $r/R=1$  designates the microfiber outer surface).

## CONCLUSION

In this work, two independent 3D cultures of different cancer cells were preliminary experimentally investigated while chemical engineering methods were used to analyze and interpret the obtained results. In Experiment 1, continuous superficial velocity of  $80 \mu\text{m s}^{-1}$  was indicated as unfavorable for survival of cancer cells NT2/D1 in alginate microbead superficial zones. Application of the Carman-Kozeny equation yielded the shear stress of 67 mPa, equal to the upper reported physiological level. In Experiment 2, the superficial velocity of  $100 \mu\text{m s}^{-1}$  enhanced the proliferation of glioma cancer cells C6 immobilized in alginate microfibers compared to the static control culture. A simple mass transport model within microfibers indicated that the substances with diffusivities of  $\sim 10^{-9}$ - $10^{-11} \text{ m}^2 \text{ s}^{-1}$  are sufficiently supplied by diffusion only. In contrast, for the substances with significantly lower diffusivities ( $\sim 10^{-19} \text{ m}^2 \text{ s}^{-1}$ ), convective transport is necessary for the efficient provision to the immobilized cells. Although the results of Experiments 1 and 2 could not be directly compared, applying chemical engineering methods provided an estimation of certain culture parameters (*i.e.*, hydrodynamic shear stress level and mass transport mechanisms and rates) that could have induced the observed results indicating future directions for the culture system optimization.

## Acknowledgment

This work was supported by funding from the European Union's Horizon 2020 research and innovation program under grant agreement no. 952033 and by the Ministry of Education, Science and Technological Development RS (Contracts No. 451-03-9/2021-14/200135, 451-03-9/2021-14/200287, and 451-03-9/2021-14/200042). We thank Prof. Peter W. Andrews (University of Sheffield, UK) for NT2/D1 cells.

## REFERENCES

- [1] H. Sung, J. Ferlay, R.L. Siegel, M. Laversanne, I. Soerjomataram, A. Jemal, F. Bray, *Ca-Cancer J. Clin.* 71 (2021) 209-249.
- [2] M. Kapalczyńska, T. Kolenda, W. Przybyła, M. Zajączkowska, A. Teresiak, V. Filas, M. Ibbs, R. Bliźniak, Ł. Łuczewski, K. Lamperska, *Arch. Med. Sci.* 14 (2018) 910-919.
- [3] H. Ungefroren, S. Sebens, D. Seidl, H. Lehnert, R. Hass, *Cell Commun. Signaling* 9 (2011) 1-8.
- [4] J.A. Hickman, R. Graeser, R. de Hoogt, S. Vidic, C. Brito, M. Gutekunst, H. van der Kuip, *Biotechnol. J.* 9 (2014) 1115-1128.
- [5] A. Nyga, U. Cheema, M. Loizidou, *J. Cell Commun. Signaling* 5 (2011) 239-248.
- [6] M.D. Szeto, G. Chakraborty, J. Hadley, R. Rockne, M. Muzi, E.C. Alvord, K.A. Krohn, A.M. Spence, K.R. Swanson, *Cancer Res.* 69 (2009) 4502-4509.
- [7] N. Filipovic, T. Djukic, I. Saveljic, P. Milenkovic, G. Jovicic, M. Djuric, *Comput. Methods Programs Biomed.* 115 (2014) 162-170.
- [8] P. Caccavale, M.V. De Bonis, G. Marino, G. Ruocco, *Int. Commun. Heat Mass Transfer* 117 (2020) 104781.
- [9] T. Chen, N.F. Kirkby, R. Jena, *Comput. Methods Programs Biomed.* 108 (2012) 973-983.
- [10] D. Karami, N. Richbourg, V. Sikavitsas, *Cancer Lett. (N. Y., NY, U. S.)* 449 (2019) 178-185.
- [11] D. Massai, G. Isu, D. Madeddu, G. Cerino, A. Falco, C. Frati, D. Gallo, M.A. Deriu, G. Falvo D'Urso Labate, F. Quaini, A. Audenino, U. Morbiducci, *PLoS One* 11 (2016) e0154610.
- [12] J.E. Trachtenberg, M. Santoro, C. Williams III, C.M. Piard, B.T. Smith, J.K. Placone, B.A. Menegaz, E.R. Molina, S.-E. Lamhamedi-Cherradi, J.A. Ludwig, V.I. Sikavitsas, J.P. Fisher, A.G. Mikos, *ACS Biomater. Sci. Eng.* 4 (2018) 347-356.
- [13] C.M. Novak, E.N. Horst, C.C. Taylor, C.Z. Liu, G. Mehta, *Biotechnol. Bioeng.* 116 (2019) 3084-3097.
- [14] V.S. Shirure, S.F. Lam, B. Shergill, Y.E. Chu, N.R. Ng, S.C. George, *Lab Chip* 20 (2020) 3036-3050.
- [15] K.Y. Lee, D.J. Mooney, *Prog. Polym. Sci.* 37 (2012) 106-126.
- [16] K.I. Draget, G. Skjåk-Bræk, O. Smidsrød, *Int. J. Biol. Macromol.* 21 (1997) 47-55.
- [17] P. Sánchez, R.M. Hernández, J.L. Pedraz, G. Orive, in

- Immobilization of Enzymes and Cells, Humana Press, Totowa, NJ (2013) 313-325.
- [18] B.R. Lee, K.H. Lee, E. Kang, D.S. Kim, S.H. Lee, *Biomicrofluidics* 5 (2011) 022208.
- [19] F.M. Kievit, S.J. Florczyk, M.C. Leung, O. Veiseh, J.O. Park, M.L. Disis, M. Zhang, *Biomaterials* 31 (2010) 5903-5910.
- [20] M. Leung, F.M. Kievit, S.J. Florczyk, O. Veiseh, J. Wu, J.O. Park, M. Zhang, *Pharm. Res.* 27 (2010) 1939-1948.
- [21] S.J. Florczyk, G. Liu, F.M. Kievit, A.M. Lewis, J.D. Wu, M. Zhang, *Adv. Healthcare Mater.* 1 (2012) 590-599.
- [22] Q. Wang, S. Li, Y. Xie, W. Yu, Y. Xiong, X. Ma, Q. Yuan, *Hepato. Res.* 35 (2006) 96-103.
- [23] M.L. Tang, X.J. Bai, Y. Li, X.J. Dai, F. Yang, *Curr. Med. Sci.* 38 (2018) 809-817.
- [24] C. Liu, D.L. Mejia, B. Chiang, K.E. Luker, G.D. Luker, *Acta Biomater.* 75 (2018) 213-225.
- [25] N. Chaicharoenaudomrung, P. Kunhorm, W. Promjantuek, N. Heebkaew, N. Rujanapun, P. Noisa, *J. Cell. Physiol.* 234 (2019) 20085-20097.
- [26] K. Xu, K. Ganapathy, T. Andl, Z. Wang, J.A. Copland, R. Chakrabarti, S.J. Florczyk, *Biomaterials* 217 (2019) 119311.
- [27] L.E. Marshall, K.F. Goliwas, L.M. Miller, A.D. Penman, A.R. Frost, J.L. Berry, *J. Tissue Eng. Regener. Med.* 11 (2017) 1242-1250.
- [28] M. Santoro, S.E. Lamhamedi-Cherradi, B.A. Menegaz, J.A. Ludwig, A.G. Mikos, *Proc. Natl. Acad. Sci. U. S. A.* 112 (2015) 10304-10309.
- [29] X. Wan, Z. Li, H. Ye, Z. Cui, *Biotechnol. Lett.* 38 (2016) 1389-1395.
- [30] M.G. Muraro, S. Muenst, V. Mele, L. Quagliata, G. Iezzi, A. Tzankov, W.P. Weber, G.C. Spagnoli, S.D. Soysal, *Oncolimmunology* 6 (2017) e1331798.
- [31] X. Wan, S. Ball, F. Willenbrock, S. Yeh, N. Vlahov, D. Koennig, M. Green, G. Brown, S. Jeyaretna, Z. Li, Z. Cui, H. Ye, E. O'Neill, *Sci. Rep.* 7 (2017) 1-13.
- [32] C. Manfredonia, M.G. Muraro, C. Hirt, V. Mele, V. Governa, A. Papadimitropoulos, S. Däster, S.D. Soysal, R.A. Drosner, R. Mechera, D. Oertli, R. Rosso, M. Bolli, A. Zettl, L.M. Terracciano, G.C. Spagnoli, I. Martin, G. Iezzi, *Adv. Biosyst.* 3 (2019) 1800300.
- [33] C. Hirt, A. Papadimitropoulos, M.G. Muraro, V. Mele, E. Panopoulos, E. Cremonesi, R. Ivanek, E. Schultz-Thater, R. Drosner, C. Mengus, M. Hebeber, D. Oertli, G. Iezzi, P. Zajac, S. Eppenberger-Castori, L. Tornillo, L. Terracciano, I. Martin, G.C. Spagnoli, *Biomaterials* 62 (2015) 138-146.
- [34] F. Foglietta, G.C. Spagnoli, M.G. Muraro, M. Ballestri, A. Guerrini, C. Ferroni, A. Aluigi, G. Sotgiu, G. Varchi, *Int. J. Nanomed.* 13 (2018) 4847-4867.
- [35] H. Qazi, Z.-D. Shi, J.M. Tarbell, *PloS One* 6 (2011) e20348.
- [36] D.H. Tryoso, D.A. Good, *J. Physiol.* 515.2 (1999) 355-365.
- [37] L. Ziko, S. Riad, M. Amer, R. Zdero, H. Bougherara, A. Amleh, *Biomed. Res. Int.* 2015 (2015), ID 430569.
- [38] A. Marrella, A. Fedi, G. Varani, I. Vaccari, M. Fato, G. Firpo, P. Guida, N. Aceto, S. Scaglione, *PLoS One* 16 (2021) e0245536.
- [39] J. Stojkowska, B. Bugarski, B. Obradovic, *J. Mater. Sci.: Mater. Med.* 21 (2010) 2869-2879.
- [40] A. Osmokrovic, B. Obradovic, D. Bugarski, B. Bugarski, G. Vunjak-Novakovic, *FME Trans.* 34 (2006) 65-70.
- [41] J. Stojkowska, J. Zvicer, M. Milivojević, I. Petrović, M. Stevanović, B. Obradović, *Hem. Ind.* 74 (2020) 187-196.
- [42] J. Stojkowska, P. Petrovic, I. Jancic, M.T. Milenkovic, B. Obradovic, *Appl. Microbiol. Biotechnol.* 103 (2019) 8529-8543.
- [43] J. Stojkowska, J. Zvicer, Ž. Jovanović, V. Mišković-Stanković, B. Obradović, *J. Serb. Chem. Soc.* 77 (2012) 1709-1722.
- [44] D.D. Kostic, I.S. Malagurski, B.M. Obradovic, *Hem. Ind.* 71 (2017) 383-394.
- [45] R.G. Holdich, *Fundamentals of particle technology*, Midland Information Technology and Publishing, Hathern, Leicestershire (2002) 45-54.
- [46] E. Fröhlich, G. Bonstingl, A. Höfler, C. Meindl, G. Leitinger, T.R. Pieber, E. Roblegg, *Toxicol. In Vitro* 27 (2013) 409-417.
- [47] M.J. Mitchell, M.R. King, *Front. Oncol.* 3 (2013) 44.
- [48] Y. Chen, R. Cairns, I. Papandreou, A. Koong, N.C. Denko, *PloS One* 4 (2009) e7033.
- [49] A. Gomes, L. Guillaume, D.R. Grimes, J. Fehrenbach, V. Lobjois, B. Ducommun, *PloS One* 11 (2016) e0161239.
- [50] Y. Shen, X. Li, D. Dong, B. Zhang, Y. Xue, P. Shang, *Am. J. Cancer Res.* 8 (2018) 916-931.
- [51] D. Kostic, S. Vidovic, B. Obradovic, *J. Nanopart. Res.* 18 (2016) 76-92.
- [52] A.C. Hulst, H.J.H. Hens, R.M. Buitelaar, J. Tramper, *Biotechnol. Tech.* 3 (1989) 199-204.
- [53] T.L. Place, F.E. Domann, A.J. Case, *Free Radical Biol. Med.* 113 (2017) 311-322.
- [54] B.A. Wagner, S. Venkataraman, G.R. Buettner, *Free Radical Biol. Med.* 51 (2011) 700-712.
- [55] X. Hong, Y. Meng, S.N. Kalkanis, *J. Biol. Methods* 3 (2016) e51.
- [56] A. Ciechanover, A.L. Schwartz, A. Dautry-Varsat, H.F. Lodish, *J. Biol. Chem.* 258 (1983) 9681-9689.
- [57] R. Zadro, B. Pokrić, Z. Pučar, *Anal. Biochem.* 117 (1981) 238-244.
- [58] P. Aisen, I. Listowsky, *Annu. Rev. Biochem.* 49 (1980) 357-393.
- [59] J.R. Kanwar, G. Mahidhara, R.K. Kanwar, *Nanomedicine* 7 (2012) 1521-1550.
- [60] J. Wally, S.K. Buchanan, *BioMetals* 20 (2007) 249-262.

MIA RADONJIĆ <sup>1,2,\*</sup>  
JELENA PETROVIĆ <sup>1,2,\*</sup>  
MILENA MILIVOJEVIĆ <sup>3</sup>  
MILENA STEVANOVIĆ <sup>3,4,5</sup>  
JASMINA STOJKOVSKA <sup>1,2</sup>  
BOJANA OBRADOVIĆ <sup>1</sup>

<sup>1</sup> Univerzitet u Beogradu,  
Tehnološko-metalurški fakultet,  
Beograd, Srbija

<sup>2</sup> Inovacioni centar Tehnološko-  
metalurškog fakulteta, Beograd,  
Srbija

<sup>3</sup> Univerzitet u Beogradu, Institut  
za molekularnu genetiku i  
genetičko inženjerstvo, Beograd,  
Srbija

<sup>4</sup> Univerzitet u Beogradu, Biološki  
fakultet, Beograd, Srbija

<sup>5</sup> Srpska akademija nauka i  
umetnosti, Beograd, Srbija

\* Autori su dali podjednak doprinos radu

NAUČNI RAD

## HEMIJSKO-INŽENJERSKE METODE U ANALIZI 3D KULTURA MALIGNIH ČELIJA: RAZMATRANJE HIDRODINAMIKE I PRENOSA MASE

*U ovom radu, primenjen je multidisciplinarni pristup baziran na eksperimentima i matematičkom modelovanju za razvoj trodimenzionalnih (3D) kultura malignih ćelija. Naime, dve ćelijske linije, ćelije embrionalnog humanog teratokarcinoma NT2/D1 i ćelije glioma pacova C6, imobilisane su u alginatne mikročestice odnosno alginatna mikrovlakna, i gajene u statičkim i u uslovima kontinualnog protoka u protočnim bioreaktorima pri čemu su hemijsko-inženjerski principi primenjeni u analizi dobijenih rezultata. Površinska brzina medijuma za gajenje ćelija od  $80 \mu\text{m s}^{-1}$  je dovela do manje vijabilnosti NT2/D1 ćelija u površinskim zonama mikročestica što je ukazalo na negativne efekte hidrodinamičkih smicajnih napona čija je proračunata vrednost iznosila  $\sim 67 \text{ mPa}$ . Sa druge strane, slična vrednost površinske brzine ( $100 \mu\text{m s}^{-1}$ ) je uticala na povećanje proliferacije C6 glioma ćelija unutar mikrovlakana u odnosu na kontrolu u statičkim uslovima. Dodatna studija otpuštanja srebra iz nanokompozitnih Ag/alginatnih mikrovlakana sa medom u uslovima protoka je pokazala da medijum delimično prolazi kroz sama vlakna (intersticijalnom brzinom od  $\sim 10 \text{ nm s}^{-1}$ ). Prema tome, za opisivanje prenosa mase do imobilisanih ćelija unutar mikrovlakana primenjen je model difuzije sa advекcijom i reakcijom. Pokazano je da je difuzija dovoljan mehanizam prenosa za supstance sa koeficijentima difuzije reda veličine  $\sim 10^9\text{-}10^{11} \text{ m}^2 \text{ s}^{-1}$ , dok je za dopremanje supstanci sa značajno manjim vrednostima koeficijenta difuzije ( $\sim 10^{19} \text{ m}^2 \text{ s}^{-1}$ ) potreban dodatni advекtivni transport. Ovaj rad ilustruje način izbora i doprinos hemijsko-inženjerskih metoda u razvoju in vitro modela tumora.*

*Ključne reči: inženjerstvo tumora, alginatni hidrogel, protočni bioreaktor, matematičko modelovanje, C6 ćelijska linija glioma, ćelijska linija embrionalnog humanog teratokarcinoma NT2/D1.*



PREDRAG KOJIĆ <sup>1</sup>  
JOVANA KOJIĆ <sup>2</sup>  
MILADA PEZO <sup>3</sup>  
JELENA KRULJ <sup>2</sup>  
LATO PEZO <sup>4</sup>  
NIKOLA MIRKOV <sup>3</sup>

<sup>1</sup> University of Novi Sad, Faculty of  
Technology Novi Sad, Novi Sad,  
Serbia

<sup>2</sup> University of Novi Sad, Institute of  
Food Technology, Novi Sad, Serbia

<sup>3</sup> University of Belgrade,  
Department of Thermal Engineering  
and Energy, "Vinča" Institute of  
Nuclear Sciences - National Institute  
of the Republic of Serbia

<sup>4</sup> University of Belgrade, Institute of  
General and Physical Chemistry,  
Belgrade, Serbia

SCIENTIFIC PAPER

UDC 532.5:519.6:66.021.2

## NUMERICAL STUDY OF THE HYDRODYNAMICS AND MASS TRANSFER IN THE EXTERNAL LOOP AIRLIFT REACTOR

### Article Highlights

- Numerical study of external-loop airlift reactor (ELAR) was performed
- Hydrodynamics and gas-liquid mass transfer coefficient of the ELAR was studied
- The influence of gas velocity, alcohol types and alcohol concentration were investigated
- A two-phase CFD model applying the Eulerian-Eulerian model was developed
- The coefficient of volumetric mass transfer was determined using CFD and ANN model

### Abstract

*The objective of this study was to investigate the hydrodynamics and the gas-liquid mass transfer coefficient of an external-loop airlift reactor (ELAR). The ELAR was operated in three cases: different inlet velocities of fluids, different alcohols solutions (water, 0.5% methanol, 0.5% ethanol, 0.5% propanol and 0.5% butanol) and different concentration of methanol in solutions (0%, 0.5%, 1%, 2% and 5%). The influence of superficial gas velocity and various diluted alcohol solutions on hydrodynamics and the gas-liquid mass transfer coefficient of the ELAR was studied. Experimentally, the gas hold-up, liquid velocities and volumetric mass transfer coefficient values in the riser and the downcomer were obtained from the literature source. A computational fluid dynamics (CFD) model was developed, based on two-phase flow, investigating different liquids regarding surface tension, assuming the ideal gas flow, applying the finite volume method and Eulerian-Eulerian model. The volumetric mass transfer coefficient was determined using the CFD and artificial neural network model. The effects of liquid parameters and gas velocity on the characteristics of the gas-liquid mass transfer were simulated. These models were compared with the appropriate experimental results. The CFD model successfully simulates the influence of different alcohols regarding the number of C-atoms on hydrodynamics and mass transfer.*

*Keywords: airlift reactor, hydrodynamics, mass transfer, Eulerian-Eulerian model, artificial neural network model.*

Airlift reactors are widely used in chemical engineering, process engineering, food industry and biotechnology, wastewater treatment, and various fermentation processes. Airlift reactors are gas-liquid or gas-liquid-solid contactors in which the gas is a dis-

persed phase and is introduced continuously. At the same time, the liquid is a continuous phase that is constantly introduced or in batches. The liquid circulates through separate tubes (riser and downcomer), and there is generally no recirculation of the gas phase. The advantages of these devices utilization are: mass and heat transfer are more efficient, high fluid circulation rate, simple construction with no moving parts, maintenance is easier, self-inducing fluid flow due to the difference of fluid densities in the riser and downcomer tube, reliable temperature control, good mixing and low production costs. The parameters that influence the working con-

Correspondence: L. Pezo, University of Belgrade, Institute of General and Physical Chemistry, Belgrade, Serbia.

E-mail: [latopezo@yahoo.co.uk](mailto:latopezo@yahoo.co.uk)

Paper received: 22 May, 2021

Paper revised: 17 August, 2021

Paper accepted: 22 September, 2021

<https://doi.org/10.2298/CICEQ210522034K>

ditions are various: bubble size, the geometry of the construction, the temperature of the fluids, density, viscosity, surface tension, the rheological properties of the fluids, etc. Understanding these influences can contribute to a better conduct of output characteristics. The computational fluid dynamic (CFD) approach is a tool for mathematical modelling of complex flow characteristics and could be useful for this type of external loop airlift reactor. Different numerical approaches, such as artificial neural network (ANN) modelling, can also predict the mass transfer coefficient and hydrodynamic parameters.

The airlift reactor was firstly introduced in the study of Lefrancois *et al.* [1]. Then, a comprehensive review of the research concerning the investigations of the fluid physical characteristics, measurement techniques and review of the developed mathematical models of flow dynamics in airlift reactors were investigated by Zhang *et al.* [2].

For decades, engineers and researchers investigated the hydrodynamics and mass transfer in airlift reactors experimentally and numerically. Some proposed a modified construction of the airlift reactor to obtain better characteristics. A modified airlift reactor with slanted baffles in the riser compartment was developed to improve the oxygen transfer coefficient [3]. A construction based on a combination of an external loop airlift reactor with a fluidized bed was proposed in the study of Guo *et al.* [4]. Lukic *et al.* [5] proposed a novel design of self-agitated impellers to improve flow and mass transfer characteristics.

Many researchers dealt with experimental and numerical investigations to understand, analyse, and improve the flow regime and mass transfer in airlift reactors. The effect of the circulation liquid velocity and the influence of the riser-to-downcomer cross-sectional area ratio on the mixing efficiency was investigated both experimentally and numerically in the study by Burlutskii and Felice [6]. The analyses of the mass transfer in an external-loop airlift reactor were presented in many literature reports [7-10]. The two-phase mathematical model with turbulence characteristics has been used to predict the overall mass transfer coefficient. Experimental analyses and mathematical models have been developed to predict the axial dispersion coefficient in the riser of an external-loop airlift reactor [11].

Experimental study of the hydrodynamics of the liquid circulation was investigated in many literature reports [12, 13]. It was shown that the transition between the homogeneous and heterogeneous flow regimes depends on the liquid circulation, initial gas distribution, and equipment size. The determination

mass transfer coefficient and prediction of the volumetric oxygen transfer coefficient were analyzed in experiments performed by numerous authors [14, 15]. Lin *et al.* [16] investigated the influence of the gas distributor on the local hydrodynamic behaviour of an external loop airlift reactor. Pronczuk and Bizon [17] performed an experimental study of the liquid mixing characteristic of an external-loop airlift reactor with a fluidized bed.

Several computational two-phase flow models can be found in the literature. Jiang *et al.* [18] introduced a CFD study with three different drag models. McClure *et al.* [19] developed a computational numerical model of surfactant-containing systems. The computational approach introduced by the Eulerian-Eulerian model has been introduced with the standard  $k-\epsilon$  turbulence model [20, 21]. Roy *et al.* [22] performed the CFD simulation using the two-fluid flow and axial dispersion model in external loop airlift reactors. A two-phase turbulent  $k-\epsilon$  computational model considering the drag, lift, and turbulent dispersion forces was used to model an airlift loop reactor to treat refined soybean oil wastewater [23]. Other numerical methods have also been used for modelling flow in the airlift reactors, such as the model based on macroscopic balances of the external loop airlift reactor operating in three stages [24], the model supported by vector regression for predicting hydrodynamic parameters [25], and the artificial neural network model for predicting mass transfer in external loop airlift reactors [26].

In this paper, analyses of the hydrodynamics and gas-liquid mass transfer coefficient of airlift reactor were investigated for: water as working fluid, with different superficial gas inlet velocities (0.01-0.08 m/s) (the first set of experiments, which showed the influence of the superficial gas velocity); different working fluids, including water, 0.5% methanol, 0.5% ethanol, 0.5% propanol and 0.5% butanol (the second set of experiments, which showed the influence of the fluid type); and different methanol concentration in water, 0% methanol, 0.5% methanol, 1% methanol, 2% methanol and 5% methanol (the third set of experiments, which showed the influence of fluid concentration). The experimental results [27] were compared with the developed computational model. The two-phase Eulerian-Eulerian model was used for the numerical experiments, and the standard  $k$ -approach was used to model turbulence characteristics. It is worth noting that there is no record in the scientific literature that researchers have succeeded to simulate the influence of various aliphatic alcohols with different concentrations on the hydrodynamics in ELAR systems. Therefore, one of the objectives of this study was to investigate the possibility of predicting the gas hold-up

and gas-liquid mass transfer coefficient for three sets of experiments using the ANN model.

## MATERIALS AND METHODS

The experiment results were taken from a study by Posarac [27] and used for CFD modelling. The diameter of the riser and downcomer was 0.10 m, and the tube height was 2.83 m. Complete separation of the gas and liquid phases occurred in the upper part of the column. Subsequently, the gas did not circulate through the downcomer. The air was sparged in the column through a single orifice of 4 mm in diameter. In all experiments, compressed air was used as the gas phase. The experimental considerations were designed for different inlet velocities (between 0.01 and 0.08 m/s) (first experiment), five types of fluids in the second experiment (water, 0.5% methanol, 0.5% ethanol, 0.5% propanol and 0.5% butanol), and five different methanol concentrations in the third experiment (0% methanol, 0.5% methanol, 1% methanol, 2% methanol and 5% methanol). The physical properties of these liquids are given in Table 1.

Table 1. Properties of the fluids at 20 °C (Posarac, 1988)

Liquid phase	Density (kg/m <sup>3</sup> )	Viscosity (mPa·s)	Surface tension (mN/m)
Water	999.7	1.31	74.2
0.5% methanol	999.0	1.20	72.1
0.5% ethanol	998.8	1.20	70.1
0.5% propanol	998.5	1.21	68.3
0.5% butanol	994.9	1.21	63.8
1% methanol	998.0	1.20	69.9
2% methanol	996.2	1.19	67.2
5% methanol	993.0	1.17	61.6

Experimental tests within this research [27] include the measurements of gas hold-up in the riser tube, the determination of liquid velocity in the downcomer, and the volumetric mass transfer coefficient for the above-mentioned model systems in the ELAR.

The geometrical characteristics of this airlift reactor were presented in the literature [27]. The basic geometry parameters used for the CFD simulation were: the riser tube diameter and height (100 mm and 2800 mm, respectively), the downcomer tube diameter and height (100 mm and 1950 mm, respectively), and the separator width, length and height (300 mm, 440 mm, and 280 mm, respectively), while the gas inlet

diameter was 4 mm. In addition, the distance between the riser and downcomer tube was 100 mm, the liquid height above the inlet tube was 40 mm, and the volume of the liquid was approximately 45 l. The ELAR schematic diagram and the 3D model used for computational simulations are presented in Figure 1.

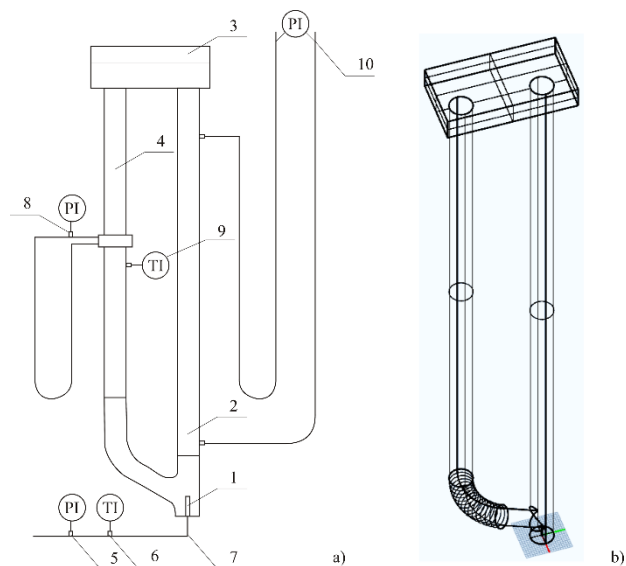


Figure 1. External loop airlift reactor, a) schematic diagram of external loop airlift reactor, 1-inlet, 2-riser tube, 3-gas separator, 4-downcomer tube, 5-manometer, 6-thermometer, 7-gas flow meter, 8-manometer, 9-thermometer, 10-manometer, b) 3D model used for computational simulations.

## Description of the computational model

The numerical experiments were performed to determine the potential of fluid velocity, gas hold-up and gas-liquid mass transfer coefficient for different inlet superficial gas velocities, five fluid types, and different alcohol concentrations, as mentioned in the experimental study section. The Eulerian-Eulerian multiphase model simulated the flow regime in the considered airlift reactor. In the Euler-Euler approach, the different phases were treated as interpenetrating fluids. Each phase occupies its volume, which a different phase cannot occupy. Therefore, the phasic volume fraction concept was introduced and was a distinguishing feature of the model. Conservation equations for momentum and continuity for each phase were solved separately, having a similar structure for all phases. These equations were closed by using constitutive correlations obtained from empirical data. Conservation equations were coupled with the pressure field, which was the same for all phases and through interphase exchange coefficients. In the presented model, the action of the gravitational force was also assumed and added to the balance equations.

### Governing equations

The mass conservation equation for a phase identified by an index  $k$  has the following form:

$$\frac{\partial}{\partial t}(\alpha_k \rho_k) + \nabla \cdot (\alpha_k \rho_k \vec{v}_k) = 0 \quad (1)$$

where  $\vec{v}_k$  and  $\rho_k$  are the velocity and density of phase  $k$ . The parameter  $\alpha_k$  represents the void fraction of phase  $k$ .

The momentum conservation equation for a phase identified by index  $k$  has the following form:

$$\frac{\partial}{\partial t}(\alpha_k \rho_k \vec{v}_k) + \nabla \cdot (\alpha_k \rho_k \vec{v}_k \vec{v}_k) = -\alpha_k \nabla p + \nabla \cdot \tau_k + \alpha_k \rho_k \vec{g} + \vec{F}_k + \vec{F}_{i,k} + \vec{F}_{m,k} + \vec{F}_{vm,k} \quad (2)$$

where  $\nabla p$  is the gradient of the shared pressure,  $\tau_k$  is the stress tensor,  $\vec{F}_k$  is external body force,  $\vec{F}_{i,k}$  is the interphase drag force,  $\vec{F}_{l,k}$  is the lift force, and  $\vec{F}_{vm,k}$  is the virtual mass force.

The stress-strain tensor  $\tau_k$  was computed by:

$$\tau_k = \alpha_k \mu_k (\nabla \vec{v}_k + \nabla \vec{v}_k^T) + \alpha_k \left( \lambda_k - \frac{2}{3} \mu_k \right) \nabla \cdot \vec{v}_k \quad (3)$$

where  $\mu_k$  is shear, and  $\lambda_k$  is the bulk viscosity of phase  $k$ .

Interphase exchange is usually modelled by the Schiller and Naumann drag model [28]. However, this model is usually used for the particles in still fluids. When applied to the external loop reactor, it needs to be modified. This correlation has been widely used to simulate gas-liquid flow [29, 20]; it considers the spherical shape and uniform gas bubble size. A bubble diameter of 3.0 mm was reasonable to approach the flow pattern [20].

The lift force was calculated by [30]:

$$\vec{F}_{lift,k} = -0.5 \rho_k \alpha_k (\vec{v}_k - \vec{v}_j) \times (\nabla \times \vec{v}_k) \quad (4)$$

Virtual mass force was defined in the following manner:

$$\vec{F}_{vm} = 0.5 \rho_k \alpha_k \left( \frac{d\vec{v}_k}{dt} - \frac{d\vec{v}_j}{dt} \right) \quad (5)$$

### Coefficients of mass transfer

The volumetric mass transfer coefficient is calculated as the product of the overall mass transfer coefficient and specific interfacial area. The specific interfacial area depends on the bubble diameter and gas hold-up values. The overall mass transfer coefficient depends on the diffusivity of oxygen in the water and the contact time [9, 31]. The model of mass transfer coefficient based on penetration theory [32]

has been compared for all experimental conditions. The results showed that the penetration model predicts mass transfer coefficient values slightly higher. Regarding other details of the solution algorithm, the choices of the particular schemes, based on previous experience, the suggestion from official software documentation, and the published literature, are summarized in Table 2.

Table 2. Simulation settings

Solver type	Pressure based, 3D, transient
Multiphase model	Eulerian, no slip velocity
Viscous model	Turbulent, two-equation standard $k-\varepsilon$
Materials	Primary phase-water, 0.5% methanol, 0.5% ethanol, 0.5% propanol and 0.5% butanol (the second set of experiments); Water, 0.5% methanol, 1% methanol, 2% methanol and 5% methanol butanol (the third set of experiments); Secondary phase-air
Interaction between phases	Schiller and Naumann (Schiller and Naumann, 1935)
Pressure-velocity coupling	SIMPLE
Pressure interpolation scheme	PRESTO!
Convection scheme - momentum	Second order upwind
Turbulent scalars	First order upwind
Volume fraction	Second order upwind
Time stepping	Backward Euler, first order

Boundary conditions were defined in the following manner: air inlet (0.01-0.08 m/s), fixed walls, an outlet at the top of the reactor, atmospheric pressure. At the inlet, the flow rate conditions were defined as the values of the inlet velocity (constant), the turbulence intensity was set to 5% (constant), and the inlet hydraulic diameter (constant). No-slip velocity conditions were used as boundary conditions at the fixed walls [9, 20]. A special class of the boundary condition was used at the outlet, where the turbulence intensity was set to 5% and the outlet hydraulic diameter was constant. The computational domain was large enough for boundary conditions and did not affect the liquid flow characteristics. The reference values were 300 kPa for pressure and 293 K for temperature. It was assumed that the bubble diameter was 3 mm, and it was an acceptable size to predict the flow pattern in the vicinity of the bulk zone [20, 33]. It was also assumed that the



bubbles have approximately the same size [39]. The time step was 0.001 s.

The three-dimensional computational mesh was used to represent the experimental domain. The presented mesh consisted of tetrahedral cells, with around 900,000 cells. Repeated simulations were conducted on the successively refined meshes until the desired mesh independence was observed, and the reported results were pertinent to the grid-independent solutions. The convergence was achieved when the sums of the absolute values of the residuals for all variables fell below  $10^{-5}$ . Numerical mesh refinement tests showed that the gas hold-up and the overall flow field predictions were relatively insensitive to the increase of the control volumes.

The system of the governing equations introduced the numerical investigation. First, the balance equation set was solved using the finite control volume method based on the SIMPLE solution method (Semi-Implicit Method for Pressure Linked Equations, [34]). Then, a discretization of the partial differential equations for momentum, volume fraction, turbulent kinetic energy, and transient formulation was carried out by the second-order upwind spatial discretization method. The numerical simulations were performed in Ansys Fluent computer code.

### ANN modelling

A multi-layer perceptron model (MLP), which consisted of three layers (input, hidden, and output), was used for modelling an artificial neural network model (ANN) for the prediction of gas hold-up and gas-liquid mass transfer coefficient. Before the calculation, both input and output data were normalized to improve the behaviour of the ANN [35, 36]. In addition, the Broyden-Fletcher-Goldfarb-Shanno (BFGS) algorithm was used as an iterative method for solving unconstrained nonlinear optimization during the ANN modelling.

The experimental database for ANN was randomly divided into training, cross-validation, and testing data (with 60%, 20%, and 20% of experimental data, respectively). A series of different topologies were used, in which the number of hidden neurons varied from 5 to 20, and the training process of the network was run 100,000 times with random initial values of weights and biases. Coefficients associated with the hidden layer (weights and biases) were grouped in matrices  $W_1$  and  $B_1$ . Similarly, coefficients related to the output layer were grouped in matrices  $W_2$  and  $B_2$  [37]:

$$Y = f_1(W_2 \cdot f_2(W_1 \cdot X + B_1) + B_2) \quad (6)$$

where:  $Y$  is the matrix of the output variables,  $f_1$  and  $f_2$  are transfer functions in the hidden and output layers, respectively, and  $X$  is the matrix of input variables.

The coefficients of determination were used as parameters to check the performance of the obtained ANN model.

### The accuracy of the model

The numerical verification of the developed model was tested using the coefficient of determination ( $r^2$ ), reduced chi-square ( $\chi^2$ ), mean bias error (MBE), root mean square error (RMSE) and mean percentage error (MPE). These commonly used parameters can be calculated as follows [38]:

$$\chi^2 = \frac{\sum_{i=1}^N (x_{\text{exp},i} - x_{\text{pre},i})^2}{N - n},$$

$$RMSE = \left[ \frac{1}{N} \cdot \sum_{i=1}^N (x_{\text{pre},i} - x_{\text{exp},i})^2 \right]^{1/2},$$

$$MBE = \frac{1}{N} \cdot \sum_{i=1}^N (x_{\text{pre},i} - x_{\text{exp},i}),$$

$$MPE = \frac{100}{N} \cdot \sum_{i=1}^N \left( \frac{|x_{\text{pre},i} - x_{\text{exp},i}|}{x_{\text{exp},i}} \right) \quad (7)$$

where  $x_{\text{exp},i}$  stands for the experimental values and  $x_{\text{pre},i}$  are the predicted values calculated by the model, and  $N$  and  $n$  are the number of observations and constants, respectively.

## RESULTS AND DISCUSSION

The operation of ELAR was influenced by hydrodynamic parameters related to the behaviour of gas bubbles, such as bubble size, bubble velocity, liquid velocity, etc. Bubble formation has two stages: expansion and bubble rising [39,40]. According to that, the size of the bubble in the bubble flow was determined by the thrust force and interphase stress forces, in the transient flow by the instability of the gas-liquid surface, and at high gas velocities, in the turbulent flow by the ratio of dynamic pressure forces to surface tension forces. With a large number of bubbles, the bubble velocity was small due to the bubbles' mutual interference and the liquid's return flow.

### CFD model

The 3D numerical simulations were conducted, and the results of those numerical experiments are validated with experimental results of gas hold-up and

the velocities of the liquid phase [27].

The computational modelling results for the water velocity field and the superficial gas velocities of 0.01, 0.03, 0.05 and 0.07 m/s are shown in Figure 2. The recirculation of the liquid phase could be observed for all the observed superficial velocities in all cases. The higher value of superficial velocity induced the augmented velocities in both riser and downcomer tubes and recirculation rates. The flow from the downcomer tube strongly influenced the turn of the liquid flow at the position where the downcomer and the riser tube collides.

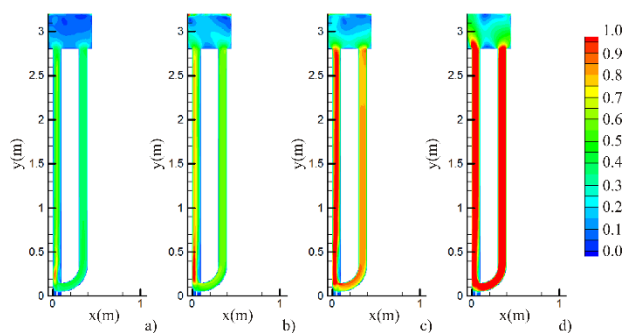


Figure 2. Overall water velocity contours for the superficial velocity of gas: a) 0.01 m/s, b) 0.03 m/s, c) 0.05 m/s and d) 0.07 m/s.

The effect of the dissolved alcohols in water on velocity profile was shown in Figure 3 for water, 0.5% methanol, 0.5% ethanol, 0.5% propanol, and 0.5% butanol. Again, the minimum flow pattern was observed for water. At the same time, the last two cases (0.5% propanol and 0.5% butanol) showed the maximum liquid flow velocities (which were reached according to lesser density and viscosities).

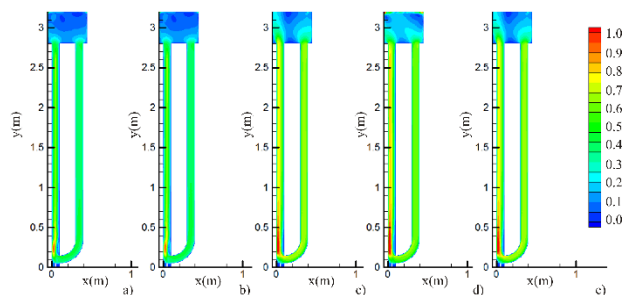


Figure 3. Overall fluid velocity contours for the superficial velocity of gas (equal to 0.01 m/s): a) water, b) 0.5% methanol, c) 0.5% ethanol, d) 0.5% propanol, and e) 0.5% butanol.

The influence of the alcohol concentration (0.5% methanol, 1.0% methanol, 2.0% methanol and 5.0% methanol) was presented on Figure 4. The higher concentration of methanol in the solution influenced

the increase of the velocity in the liquid phase. The aliphatic alcohols (ethanol, propanol and butanol) behave similarly, which coincide with the research by Keitel [41], who showed that a minimum and upper limiting alcohol concentration exerted a noticeable effect on the hydrodynamics and liquid velocity. Increasing the alcohol concentration above the upper limiting concentration enhances the liquid phase frothing and bubble coalescence effect. Therefore, with coalescence prevention in the riser, the driving force for liquid circulation decreased due to a large number of small bubbles representing the resistance to circulation [42].

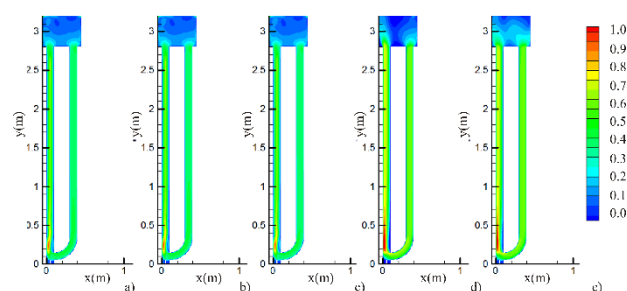


Figure 4. Overall fluid velocity contour for the superficial velocity of gas (equal to 0.01 m/s): a) water, b) 0.5% methanol, c) 1.0% methanol, d) 2.0% methanol, and e) 5.0% methanol.

It can be seen that the increase of the superficial gas velocity induces the increase of the gas hold-up and the swell level position, Figure 5. Therefore, according to the CFD results, there was no gas phase in the downcomer tube, which the experiments confirmed [27].

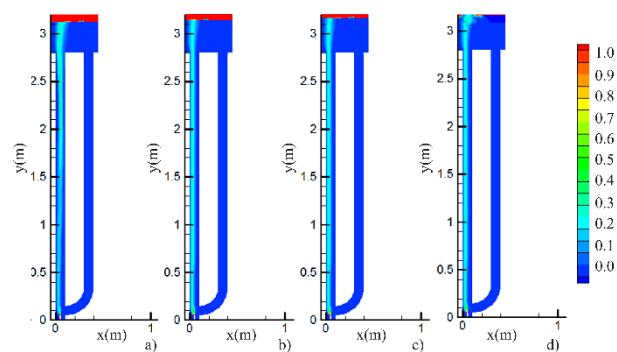


Figure 5. Overall gas hold-up contours for the superficial velocity of gas: a) 0.01 m/s, b) 0.03 m/s, c) 0.05 m/s and d) 0.07 m/s for water.

In Figure 6, the gas hold-up profiles for different fluids were presented. The liquid type (water, or methanol, ethanol, propanol or butanol solution) affected the swell level and the gas hold-up profile. The maximum gas hold-up was observed for 0.5% butanol solution, which was also gained for experimental investigation. The results showed that the increase of

the surface tension gradient, as a consequence of alcohol addition, strongly impacts the airlift reactor's hydrodynamics and mass transfer characteristics. The increase of the surface tension gradient corresponds to the rise of the number of carbon atoms in alcohol molecules [42-44]. The alcohol addition has a remarkable effect on the gas holdup. For example, gas holdup values have an average increase of about 39%, 43%, 70%, and 60% when alcohol solutions (methanol, ethanol, propanol, and butanol, respectively) were added, compared to water. The gas holdup increase was noticeable for the superficial gas velocities up to 0.03 m/s. When the fully turbulent regime was achieved, the alcohol addition did not affect the coalescence prevention, which produced a lower gas holdup increase (about 30%). The alcohol addition has a smaller effect on the liquid velocity than on the gas holdup, and the liquid velocity increased about 10% with alcohol addition.

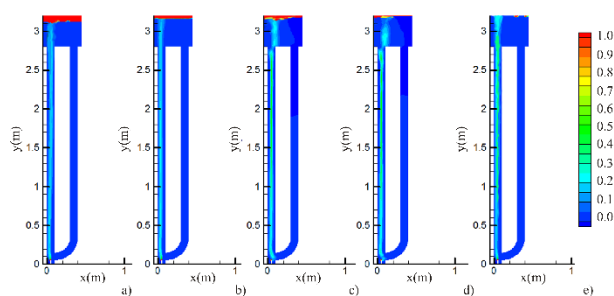


Figure 6. Overall gas hold-up contours for the superficial velocity of gas (equal to 0.01 m/s): a) water, b) 0.5% methanol, c) 0.5% ethanol, d) 0.5% propanol, and e) 0.5% butanol.

In Figure 7, the methanol concentration was investigated, and the gas hold-up was increased at a higher methanol concentration in the water solution. It has been perceived that the influence of alcohols on gas holdup increases with the augment of their concentration and the length of the carbon chain in the alcohol molecule [43]. It can be explained by changes in the surface tension gradient that causes the different coalescence suppression strengths of specific alcohol. Therefore, alcohols with lower C-atoms show lower surface tension gradients and produce lower gas holdup values [44]. In the same manner, surface tension decrease with the augment of alcohol concentration while surface tension gradient rises and consequently leads to an increase in the gas holdup of the ELAR.

In Figure 8, the experimental and CFD-predicted results for gas hold-up values are compared. For predicting gas hold-up for water, 0.5% methanol, 0.5% ethanol, 0.5% propanol, and 0.5% butanol, the CFD

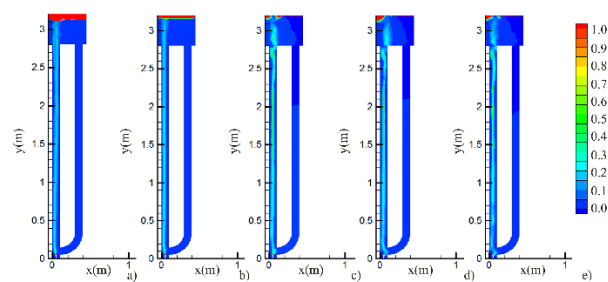


Figure 7. Overall gas hold-up contours for the superficial velocity of gas (equal to 0.01 m/s): a) water, b) 0.5% methanol, c) 1.0% methanol, d) 2.0% methanol, and e) 5.0% methanol.

model showed a good prediction capability, as can be visually observed in Figure 8a. The deviations that can be seen were attributed to the relative inaccuracy of the physical parameters of the solutions. The prediction capabilities of these models could be accessed in Table 3 ( $r^2$  values were 0.995; 0.993; 0.995; 0.991 and 0.997, respectively). According to the CFD model for the prediction of gas hold-up for water, 0.5% methanol, 1% methanol, 2% methanol and 5% methanol, the predicted variables were: 0.998; 0.996; 0.998; 0.996 and 0.992, respectively, Figure 8b and Table 3.

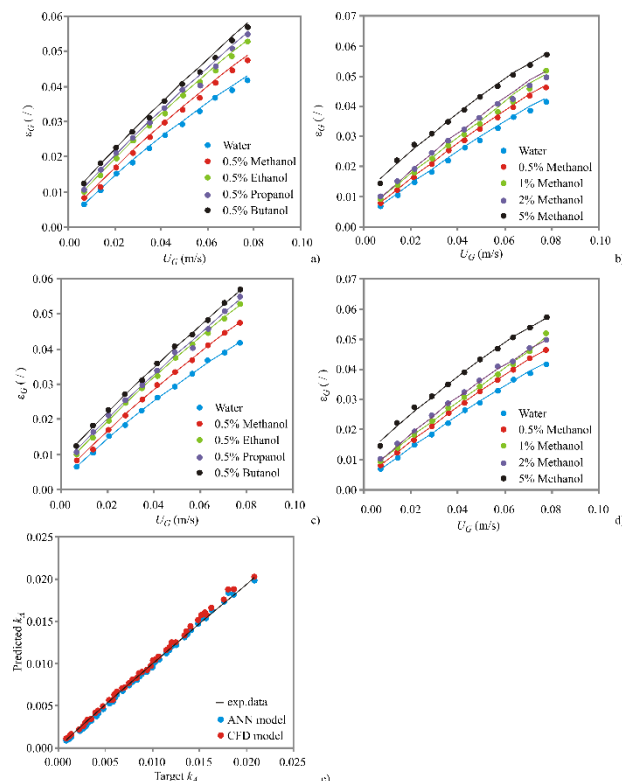


Figure 8. Comparison of experimentally obtained gas hold-up (presented as dots) for water, 0.5% methanol, 0.5% ethanol, 0.5% propanol and 0.5% butanol with a) CFD model and b) CFD model, prediction of gas hold-up for water, 0.5% methanol, 1% methanol, 2% methanol and 5% methanol with c) ANN model and d) ANN model and e) prediction coefficient of volumetric mass transfer (model data are presented as lines).

Table 3. The "goodness of fit" tests for the developed models

	CFD models , for the prediction of gas hold- up									
	$\chi^2$	RMSE	MBE	MPE	$r^2$	Skew	Kurt	Mean	StDev	Var
Water	8.16E-07	8.61E-04	3.07E-04	2.290	0.995	-0.700	2.118	0.000	0.001	7.13E-07
Methanol, 0.5%	1.28E-06	1.08E-03	-2.98E-04	2.784	0.993	1.494	3.013	0.000	0.001	1.18E-06
Ethanol, 0.5%	1.13E-06	1.01E-03	-1.84E-04	2.563	0.995	-0.241	-0.076	0.000	0.001	1.09E-06
Propanol, 0.5%	2.17E-06	1.40E-03	2.17E-05	2.526	0.991	0.639	0.078	0.000	0.001	2.16E-06
Butanol, 0.5%	1.27E-06	1.07E-03	-6.62E-04	2.164	0.997	-0.477	-1.279	-0.001	0.001	7.84E-07
Water	9.06E-07	9.08E-04	-6.09E-04	2.783	0.998	0.353	-1.503	-0.001	0.001	4.98E-07
Methanol, 0.5%	7.68E-07	8.35E-04	2.52E-04	2.066	0.996	0.793	-0.283	0.000	0.001	6.98E-07
Methanol, 1%	1.82E-06	1.28E-03	-8.38E-04	2.870	0.998	-0.295	-1.232	-0.001	0.001	1.04E-06
Methanol, 2%	9.49E-07	9.29E-04	-1.37E-04	2.007	0.996	-1.409	1.867	0.000	0.001	9.29E-07
Methanol, 5%	1.56E-06	1.19E-03	2.10E-04	2.427	0.992	-0.406	-0.512	0.000	0.001	1.51E-06
ANN model, for prediction of gas hold- up (MLP 1-5-5 and MLP 1-4-5)										
Water	2.15E-06	1.08E-03	-5.47E-04	6.467	0.996	-0.585	0.820	-0.001	0.001	9.62E-07
Methanol, 0.5%	1.70E-06	9.62E-04	-3.40E-04	4.823	0.998	-0.616	0.056	0.000	0.001	8.92E-07
Ethanol, 0.5%	1.54E-06	9.17E-04	-1.99E-04	3.576	0.997	-2.157	5.625	0.000	0.001	8.81E-07
Propanol, 0.5%	2.97E-06	1.27E-03	-5.49E-04	4.772	0.994	-1.142	1.249	-0.001	0.001	1.45E-06
Butanol, 0.5%	2.47E-06	1.16E-03	-3.69E-04	3.793	0.995	-1.411	1.428	0.000	0.001	1.33E-06
Water	2.74E-07	3.86E-04	3.74E-05	1.409	0.999	1.091	1.285	0.000	0.000	1.63E-07
Metanol, 0.5%	6.05E-08	1.82E-04	3.01E-05	0.756	1.000	-0.233	-1.176	0.000	0.000	3.53E-08
Metanol, 1%	9.81E-07	7.32E-04	6.07E-05	2.643	0.997	0.175	-0.788	0.000	0.001	5.85E-07
Metanol, 2%	3.17E-07	4.16E-04	1.55E-05	1.037	0.999	-0.987	1.969	0.000	0.000	1.90E-07
Metanol, %5	9.57E-07	7.22E-04	-8.56E-05	2.255	0.997	0.150	0.342	0.000	0.001	5.66E-07
ANN model for prediction of gas-liquid mass transfer coefficient in methanol solution (MLP 6-8-1)										
$k_A$	3.9E-08	0.000	4.8E-06	3.115	0.999	1.313	4.889	4.8E-06	2E-04	3.9E-08

### ANN model

The results of the experiments and results of the ANN models prediction (MLP 1-5-5) for gas hold-up values were presented in Figure 8c (gas hold-up for water, 0.5% methanol, 0.5% ethanol, 0.5% propanol

and 0.5% butanol) and Figure 8d, for model MLP 1-4-5 (gas hold-up for water, 0.5% methanol, 1% methanol, 2% methanol and 5% methanol), which showed good prediction capabilities. The prediction capabilities of these models could be accessed in Table 3 and 4.

Table 4. Artificial neural network model summary (performance and errors), for training, testing, and validation cycles

Network name	Performance			Error			Training algorithm	Error function	Hidden activation	Output activation
	Train.	Test.	Valid.	Train.	Test.	Valid.				
MLP 1-5-5	0.998	1.000	1.000	0.000	0.000	0.000	BFGS 18	SOS	Tanh	Exponential
MLP 1-4-5	0.999	1.000	1.000	0.000	0.000	0.000	BFGS 51	SOS	Tanh	Identity
MLP 6-8-1	0.999	1.000	1.000	0.000	0.000	0.000	BFGS 100	SOS	Logistic	Tanh

\* Performance term represents the coefficients of determination, while error terms indicate a lack of data for the ANN model.

The ANN models predicted experimental variables reasonably well for a broad range of the process variables. The ANN model had an insignificant lack of fit tests, which means the model satisfactorily predicted output variables. A high  $r^2$  indicates that the variation was accounted for and that the proposed model fitted the data adequately [45, 46].

### Coefficients of mass transfer

The ANN model performance for prediction of gas-liquid mass transfer coefficient in water, 0.5% methanol, 0.5% ethanol, 0.5% propanol and 0.5% butanol (MLP 6-8-1) was presented in Table 4. This model predicts the gas-liquid mass transfer coefficient well (the  $r^2$  values during the training cycle for the output variable were 0.999, Table 3).

The goodness of fit between experimental measurements and model-calculated outputs, represented as ANN performance (sum of  $r^2$  between measured and calculated output variables), during training, testing and validation steps, are shown in Table 3, while the visual confirmation of the ANN model could be observed in Figure 8e. The gas holdup and mass transfer coefficients are similar to other research [43, 44].

### CONCLUSION

Analyses of the hydrodynamics and mass transfer in the external loop airlift reactor were performed. The analyses were performed for different superficial gas velocities and two experimental sets depending on the type and concentration of alcohol solutions (working fluids). In addition, the values of gas hold-up, liquid velocity and volumetric mass transfer were compared with experimental values obtained from the literature [27].

The higher superficial inlet gas velocity increased the liquid velocity in both riser and downcomer tubes and recirculation rates. The minimum flow was observed for water, while the higher molecular weight alcohols increased the liquid velocity. Moreover, the higher diluted alcohol concentration influenced the increase of the velocity in the liquid phase.

The increase of the superficial inlet gas velocity induces the increase of the gas hold-up and the increase of the swell level position. The flow from the downcomer tube strongly influenced the profile of the liquid flow at the collision point of the downcomer and the riser tubes. According to the CFD results, there was no gas phase in the downcomer tube, which was also confirmed by the experiments. The liquid type affected the swell level position and gas hold-up profile. The maximum gas hold-up was observed for the highest

investigated molecular weight alcohol, also gained for the experimental investigation. The gas hold-up was increased for a higher alcohol concentration in the water solution.

CFD and ANN results for the volumetric mass transfer coefficient showed good agreement with experimental results.

### Acknowledgment

The research is funded by the Ministry of Education, Science and Technological Development of the Republic of Serbia No. 451-03-9/2021-14/ 200051 and Serbian-Slovenian bilateral project No. 337-00-21/2020-09/40.

### NOMENCLATURE

$C_D$	drag coefficient
$\vec{F}_{i,k}$	interphase drag force
$\vec{F}_{l,k}$	lift force
$\vec{F}_k$	external body force
$\vec{F}_{vm,k}$	virtual mass force
$p$	pressure (Pa)
Re	Reynolds number
$\vec{R}_{jk}$	interaction force between phases
$r^2$	coefficient of determination
$t$	time (s)
$T$	temperature (°C)
$v$	velocity (m/s)
$x_{exp,i}$	experimental values
$x_{pre,i}$	the predicted values calculated by the model
$N$	number of observations
$n$	number of constants
$\alpha_k$	void fraction of phase $k$
$\lambda_k$	bulk viscosity of phase $k$
$\mu_k$	shear
$\rho$	density (kg/m <sup>3</sup> )
$\tau_k$	the stress tensor
$\chi^2$	reduced chi-square
ANN	Artificial Neural Network
CFD	Computational Fluid Dynamics
ELAR	External-Loop Airlift Reactor
FVM	Finite Volume Method
MBE	Mean Bias Error
MLP	Multi-Layer Perceptron Model

MPE	Mean Percentage Error
RMSE	Root Mean Square Error
SIMPLE	Semi-Implicit Method for Pressure Linked Equations

## REFERENCES

- [1] M.L. Lefrancois, C.G. Mariller, J.V. Mejane, Effectionnements aux procedes de cultures forgiques et de fermentations industrielles. Brevet d'Invention, France, no. 1 102 200. (1955).
- [2] T. Zhang, C. Wei, C. Feng, Y. Ren, H. Wu, S. Preis, Chemical Engineering & Processing: Process Intensification. 144 (2019) 107633.
- [3] S. Bun, N. Chawaloesphonsiya, F. Nakajima, T. Tobino, P. Painmanakul, Journal of Environmental Chemical Engineering, 7 (2019) 103206.
- [4] Y.X. Guo, Rathor, M.N., Ti, H.C., Chem. Eng. J. 67 (1997) 205-214.
- [5] N. Lj. Lukic, I. M. Sijacki, P. S. Kojic, S. S. Popovic, M. N. Tekic, D. Lj. Petrovic, Biochem. Eng. J. 118 (2017) 53-63.
- [6] E. Burlutskii, R. Di Felice, Int. J. of Multiphas. Flow 119 (2019) 1-13.
- [7] H. Dhaouadi, S. Poncin, J. M. Hornut, G. Wild, P. Oinas, J. Korpijarvi, Chem. Eng. Sci. 52 (1997) 3909- 3917.
- [8] P. Lestinsky, P. Vayrynen, M. Vecer, K. Wichterle, Procedia Engineer. 42 (2012) 892 - 907.
- [9] S. M. Teli, C. Mathpati, Chinese J. Chem. Eng. 32 (2021) 39-60.
- [10] R. Salehpour, E. Jalilnejad, M. Nalband, K. Ghasemzadeh, Particuology. 51 (2020) 91-108.
- [11] Ch. Vial, S. Poncin, G. Wild, N. Midoux, Chem. Eng. Sci. 60 (2005) 5945 - 5954.
- [12] A.H. Essadki, B. Gourich, Ch. Vial, H. Delmas, Chem. Eng. Sci. 66 (2011) 3125-3132.
- [13] N. Bendjaballah, H. Dhaouadi, S. Poncin, N. Midoux, J. M. Hornut, G. Wild, Chem. Eng. Sci. 54 (1999) 5211-5221.
- [14] M. Gavrilescu, R. Z. Tudose, Chem. Eng. J. 66 (1997) 97-104.
- [15] K. Mohanty, D. Das, M. N. Biswas, Chem. Eng. J. 133 (2007) 257-264.
- [16] J. Lin, M. Han, T. Wang, T. Zhang, J. Wang, Y. Jin, Chem. Eng. J. 102 (2004) 51-59.
- [17] M. Pronczuk, K. Bizon, Chem. Eng. Sci. 210 (2019) 115231.
- [18] X. Jiang, N. Yang, B. Yang, Particuology 27 (2016) 95-101.
- [19] D. D. McClure, H. Norris, J. M. Kavanagh, D. F. Fletcher, G. W. Barton, Chem. Eng. Sci. 127 (2015) 189-201.
- [20] N. Moudoud, R. Rihani, F. Bentahar, J. Legrand, Chemical Engineering & Processing: Process Intensification 129 (2018) 118-130.
- [21] K. M. Dhanasekharan, J. Sanya, A. Jain, A. Haidari, Chem. Eng. Sci. 60 (2005) 213 - 218.
- [22] S. Roy, M. T. Dhotre, J. B. Joshi, Chem. Eng. Res. Des. 84(A8) (2005) 677-690.
- [23] Y. Shi, S. Wu, H. Ren, M. Jin, L. Wang, N. Qiao, D. Yu, Bioresource Technol. 296 (2020) 122316.
- [24] S. Sarkar, K. Mohanty, B.C. Meikap, Chem. Eng. J. 145 (2008) 69-77.
- [25] P. Kojic, R. Omorjan, Chem. Eng. Res. Des. 125 (2017) 398-407.
- [26] N. Naidoo, W.J. Pauck, M. Carsky, South African Journal of Chemical Engineering 33 (2020) 83-89.
- [27] D. Posarac, Investigation of Hydrodynamics and Mass-transfer in External-loop Airlift Reactor. University of Novi Sad, Faculty of Technology, Novi Sad, Serbia (PhD) (1988).
- [28] L. Schiller, A. Naumann, VDI Zeitung, 77 (1935) 318-320.
- [29] A. Gupta, S. Roy, Chem. Eng. J. 225 (2013) 818-836.
- [30] A. Tomiyama, G.P. Celata, S. Hosokawa, S. Yoshida, Int. J. Multiph. Flow. 28 (2002) 1497-1519.
- [31] X. Lu, J. Yu, Y. Ding, Can J Chem Eng 98(7) (2020) 1593-1606.
- [32] R. Higbie, Trans. Am. Inst. Chern. Eng. 31 (1935) 365-389.
- [33] M. Pourtousi, P. Ganesan, J.N. Sahu, Measurement 76 (2015) 255-270.
- [34] S.V. Patankar, D.B. Spalding, Int. J. Heat Mass Transfer 15 (1972) 1787-1806.
- [35] T. Kollo, D. von Rosen, Advanced Multivariate Statistics with Matrices (Springer, Dordrecht) (2005).
- [36] L. Pezo, B.Lj. Čurčić, V.S. Filipović, M.R. Nićetin, G.B. Koprivica, N.M. Mišljenović, Lj.B. Lević, Hem. Ind. 67 (2013) 465-475.
- [37] C.I. Ochoa-Martínez, A.A. Ayala-Aponte, LWT - Food Sci Technol 40 (4) (2007) 638-6.
- [38] M. Aćimović, L. Pezo, V. Tešević, I. Čabarkapa, M. Todosijević, Ind. Crop. Prod. 154 (15) (2020) 112752.
- [39] D. F. Fletcher, D. D. McClure, J. M. Kavanagh, G. W. Barton, App. Math. Model. 44 (2017) 25-42.
- [40] K. Schügerl, J. Lücke, U. Oels, Adv. Biochem. Eng. 7 (1977) 1-84.
- [41] G. Keitel, Untersuchungen zum Stoffaustausch in Gas-Flüssig-Dispersionen in Rührschlaufen reaktor und Blasensäule, 1978. Universität Dortmund, Dortmund, Germany (PhD Thesis).
- [42] P. S. Kojić, S. S. Popović, M. S. Tokić, I. M. Šijački, N. L. Lukić, D. Z. Jovičević, D. L. Petrović, Braz. J. Chem. Eng. 34 (2017) 493-505.
- [43] P. S. Kojić, I. M. Šijački, N. L. Lukić, D. Z. Jovičević, S. S. Popović, D. L. Petrović, Chem. Ind. Chem. Eng. Q. 22(3) (2016) 275-284.
- [44] P. S. Kojić, M. S. Tokić, I. M. Šijački, N. L. Lukić, D. L. Petrović, D. Z. Jovičević, S. S. Popović, Chemical Engineering and Technology, 38(4) (2015) 701-708.
- [45] Z. Erbay, F. Icier, J. Food Eng. 91(4) (2009) 533-541.
- [46] T. Turanyi, A.S. Tomlin, Analysis of Kinetics Reaction Mechanisms. (Springer, Berlin Heidelberg) (2014).

PREDRAG KOJIĆ <sup>1</sup>  
JOVANA KOJIĆ <sup>2</sup>  
MILADA PEZO <sup>3</sup>  
JELENA KRULJ <sup>2</sup>  
LATO PEZO <sup>4</sup>  
NIKOLA MIRKOV <sup>3</sup>

<sup>1</sup> Univerzitet u Novom Sadu,  
Tehnološki fakultet Novi Sad, Novi  
Sad, Srbija

<sup>2</sup> Univerzitet u Novom Sadu, Institut  
za prehrambenu tehnologiju, Novi  
Sad, Srbija

<sup>3</sup> Univerzitet u Beogradu, Odeljenje  
za termotehniku i energetiku, Institut  
za nuklearne nauke "Vinča" -  
Nacionalni institut Republike Srbije

<sup>4</sup> Univerzitet u Beogradu, Institut za  
opštu i fizičku hemiju, Beograd,  
Srbija

NAUČNI RAD

## NUMERIČKA STUDIJA HIDRODINAMIČKOG I MASENOG TRANSFERA U SPOLJNOM KRUGU AIRLIFT REAKTORA

*Cilj ove studije bio je istraživanje hidrodinamičkih i maseno-prenosnih karakteristika airlift reaktora sa spoljnom recirkulacijom (ELAR). ELAR je ispitan za tri slučaja: za različite ulazne brzine gasa, za različite rastvore alkohola (voda, 0,5% metanol, 0,5% etanol, 0,5% propanol i 0,5% butanol) i za različite koncentracije metanola u rastvorima (0%, 0,5%, 1%, 2% i 5%). Proučavan je uticaj ulazne prividne brzine gasa i uticaj različitih vrsta razređenih rastvora alkohola na hidrodinamiku i koeficijent prenosa mase gas-tečnost ELAR-a. Eksperimentalne vrednosti sadržaja gasa, brzine tečnosti i koeficijenta prenosa mase u ulaznoj i silaznoj cevi su preuzete iz literaturnih izvora.*

*Razvijen je matematički model zasnovan na numeričkoj mehanici fluida (CFD), primenjen na dvofazno strujanje, a istraživane su različite tečnosti u pogledu površinskog napona, primenjujući metodu konačnih zapremina, Eulerov-Eulerov model i jednačine za idealan gas. Koeficijent zapreminskog prenosa mase i vrednosti za sadržaj gasa određene su CFD modelom, kao i modelom veštačke neuronske mreže. Ispitivani su uticaji parametara tečnosti i brzine gasa na karakteristike prenosa mase u sistemu gas-tečnost. Razvijeni modeli su upoređeni sa odgovarajućim eksperimentalnim rezultatima.*

*Ključne reči: airlift reaktor, hidrodinamika, prenos mase, Eulerov-Eulerov model, model veštačke neuronske mreže.*





MARIJA B. TASIĆ<sup>1</sup>  
MIONA S. STANKOVIĆ<sup>1</sup>  
MILAN D. KOSTIĆ<sup>1</sup>  
OLIVERA S. STAMENKOVIĆ<sup>1</sup>  
VLADA B. VELJKOVIĆ<sup>1,2</sup>

<sup>1</sup> University of Niš, Faculty of  
Technology, Leskovac, Serbia

<sup>2</sup> The Serbian Academy of Sciences  
and Arts, Belgrade, Serbia

SCIENTIFIC PAPER

UDC 662.756.3:634.11:66

## CIRCULAR ECONOMY IN APPLE PROCESSING INDUSTRY: BIODIESEL PRODUCTION FROM WASTE APPLE SEEDS

### Article Highlights

- Apple seeds landfilling increases terrestrial acidity
- Valorization of apple seeds for the circular economy
- Simulation, economic and environmental models were created
- The lowest biodiesel price was 0.39 US\$/kg
- Biodiesel production from apple seeds can be environmentally friendly

### Abstract

*Apple pomace is a solid waste derived from the apple processing industry. To foster sustainability, the apple processing industry must implement the circular economy model of biorefinery and treat apple pomace as a valuable source of apple seed oil. For the first time, this study dealt with the design, economic, and potential environmental impact assessment of biodiesel production from apple seed oil obtained from apple pomace. An Aspen Plus® and WAR® software were used to evaluate the designed biodiesel production. The main production steps were the supercritical CO<sub>2</sub> extraction, the methanolysis of apple seed oil, the methanol recovery, and the biodiesel separation. The production facility was assumed to process 24 tons of apple seeds daily. The total capital and production costs were 1.26 US\$ million and 2.82 US\$ million, respectively. If revenues from selling apple seed meal as cattle feed were included, a biodiesel price could be 0.39 US\$/kg. The process was environmentally friendly when apple seed meal was not treated as waste.*

*Keywords: apple seeds, Aspen Plus®, biodiesel; economics, supercritical technology, WAR®.*

Modern industrial development is toward implementing the circular economy model to foster sustainability. Thus, all industrial waste should be used as the source of value-added products. However, industrial food waste produced in large amounts generates a significant loss of valuable materials and raises serious management problems. Nevertheless, fruits have the highest wastage rates of any food. The apple processing industry generates yearly around 8 million tons of waste apple pomace [1,2]. So far, apple pomace has been used in the production of protein-

enriched feed [3], pectin [4], citric acid [5], biopolymer polyhydroxyalkanoates [6], charcoal [7], biogas [8], ethanol [9], and acetone-butanol-ethanol [10] among others. Economically, the best technique to reuse apple pomace is yet to be shown. Vinegar production is a widely practiced way to utilize pomace from a facility engaged in apple processing. However, apple seeds in apple pomace of 2%–4% [2] can cause a bitter taste of vinegar due to hydrogen cyanide formed during the long fermentation process. Therefore, the industry prefers to remove the waste apple seeds, whose landfilling can cause severe human air to breathe problems and disturb terrestrial ecosystems.

On the other hand, apple seeds are a good source of oil and are obtained by sieving and separating from apple pomace [11]. The apple seed oil content varies in the range of 15–29.4% [12], which is similar to the soybean seed oil content (about 20%) but lower than the sunflower seed oil content (about 40%) [13]. Apple seed

Correspondence: M. Tasić, University of Niš, Faculty of Technology, Department of Chemical Engineering, Bulevar oslobođenja 124, 16000 Leskovac, Serbia.  
E-mail: [mtasic@tf.ni.ac.rs](mailto:mtasic@tf.ni.ac.rs)  
Paper received: 19 August, 2021  
Paper revised: 26 September, 2021  
Paper accepted: 29 September, 2021

<https://doi.org/10.2298/CICEQ210819035T>

oil is declared edible [14–16], but it would be hard to achieve market success like sunflower or soybean oil due to humans' difficulties to change acquired taste habits. Besides that, more information is needed on the metabolic effect of apple seed oil in humans [17,18]. Apple seed oil is already used in cosmetic industries in various products [19]. However, little is known about the waste generated in the cosmetic industry and its impact on the environment.

Biodiesel is a green alternative to fossil-derived diesel. However, feedstock production and its conversion to biodiesel can emit more greenhouse gases than fossil fuels [20]. Various feedstocks have been tested to overcome this problem. There have been several studies about the economic and environmental analysis of biodiesel production from waste biomass. However, most simulation studies of biodiesel production have focused only on waste cooking [21,22] and nonedible oils [23,24], chicken fat [25], tallow [26], and microalgae [27]. Since recently, the waste of the fruit processing industry has attracted scientists investigating biodiesel production. Valorization of fruit waste, as low-cost oily feedstocks, fits in the scope of cheap and clean biodiesel production technologies. Grape [28] and apple pomace [29,30] are promising feedstocks for biodiesel production. Although there have been several studies about custard apple waste for biodiesel production [31,32], the production is limited to tropical countries. Except for grape pomace, no previous work has included an economic evaluation or a biodiesel refinery environmental impact assessment. In addition, a recently published paper points out the lack of profound research studies with techno-economic analysis, life-cycle assessment, and inter-sectoral initiatives of apple processing-derived waste [33]. Therefore, this study improves apple waste processing compared to landfill disposal, combustion for energy, or implementation in cosmetic industries.

## MATERIALS AND METHODS

### Background

#### *Process design and simulation basis*

This paper provides an innovative conceptual process design for converting waste apple seeds to biodiesel using the Aspen Plus® v8.6 software computer simulation to obtain the consistent process flowsheet, mass and energy balances, equipment sizing, and the involved process costs. The process design and simulation involve creating a process flowsheet (setting up the unit models, operational conditions, and reaction) and defining chemical components and thermodynamics.

#### *Experimental studies supporting the model*

Figure 1 shows a block diagram for manufacturing biodiesel from apple seeds originating from waste apple pomace. Additional pretreatment steps of apple pomace (drying and deseeding) are not considered for process design because fruit processing companies perform apple pomace deseeding. Besides, many research studies have reported that they obtained apple seeds from local fruit processing companies [16,19,34,35].

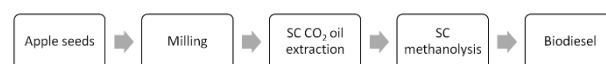


Figure 1. Block diagram of biodiesel production from apple seeds.

Apple seeds were first milled to reduce the size of seed particles and then submitted to oil extraction. So far, the oil has been extracted from apple seeds with petroleum ether [15], *n*-hexane [16,36], and supercritical (SC) CO<sub>2</sub> [34,35]. Linoleic acid is a predominantly fatty acid of apple oil regardless of the used technique from oil recovery. Therefore, the oil may be considered a suitable feedstock for biodiesel production if the ratio of polyunsaturated fatty acid content and the sum of saturated and monounsaturated fatty acid contents,  $\sum\text{PUFA}/(\sum\text{SFA} + \sum\text{MUFA})$ , is close to one or below. However, the cold filter plugging point (CFPP) has a low value [36]. Generally, apple seed oil obtained using solvents show better potential as biodiesel feedstocks. However, solvents are of fossil origin, so their replacement is strongly recommended. Furthermore, among the SC techniques, the empirical cold filter plugging point (CFPP) of apple seed oil obtained with the ultra-high SC extraction system (-7.5 °C) was lower than that (4.5 °C) conducted in the pressure range of 100–450 bar. Still, processing at ultra-high SC pressures may not be cost-competitive and safe. For the reasons above, the present study has been conceived to simulate the SC-CO<sub>2</sub> extraction of oil from apple seeds below 30 MPa. The data on the SC extraction unit conditions were based on the experimental values [34].

The extracted oil was then subjected to alcoholysis. Biodiesel production processes based on homo- or heterogeneously-catalyzed alcoholysis were not considered since the operation parameters of the oil pretreatment and the implemented catalyst have not been validated against any experimental research. However, SC simulation was relied on just one assumption - operating conditions. SC methanolysis has neither been experimentally verified. Moreover, the lab- or pilot-scale research about apple waste for biodiesel production is currently quite limited. However, simulation results will be reliable and accurate since

process simulation used in this study was classified into design mode, which means that some level of equipment performance was assumed for equipment designs to meet this performance. In this way, simulation helps to avoid the cost of building a pilot and industrial plant. The reactor equilibrium (REquil) model was used to simulate the reactor for the SC methanolysis. This reactor model performs the chemical and phase equilibrium simultaneously using only the reaction stoichiometric. With the REquil model, biodiesel yield can be predicted only using the methanolysis stoichiometry and the SC operating conditions. The standard SC oil methanolysis conditions (350 °C, 20 MPa, and oil-to-methanol molar ratio of 1:42) are implemented [37,38]. The post-treatment stage of methanol recovery and biodiesel separation was briefly examined, too.

#### *Models of chemical components and physical properties*

The simulation model components were apple seeds, trilinolein (considered apple seed oil), methanol, methyl linoleate (biodiesel), glycerol, and CO<sub>2</sub>. All chemical species were available in the Aspen Plus<sup>®</sup> component database except for apple seeds. The usage of seeds as modeling components for simulation purposes is rare. The thermodynamic properties of seeds are unknown and are defined as nonconventional solids with a particle size distribution.

The Peng-Robinson state equation was selected as a general thermodynamic model because it is an industry-standard for calculating solid-vapor and solid-liquid equilibrium [39]. Simultaneously, UNIFAC and UNIQUAQ were used in thermodynamic calculations for the process units involving apple seeds, oil, and CO<sub>2</sub>.

#### *Economics basis*

Process equipment sizing and capital cost estimating were conducted through vendor quotes and estimations for the 1<sup>st</sup> quarter of 1994, from Aspen Economic Analyzer<sup>®</sup> v8.6 software. The apple seed facility was a grass-root located in North America. The facility lifetime was set at 8760 h/year (assuming 365 operating days/year). The biorefinery would be located on soft-clay soil. It would promote a new, slightly complex process with digital process control and an ASME pressure vessel design code. The possible contingency was 18%. The facility operation and maintenance labor were set as three shifts per day. Operator and supervisor labor unit costs were 29 US\$/h and 44 US\$/h, respectively [40]. It was assumed that three operators and one supervisor could maintain continuous work of the process per shift. The estimated start date of basic engineering was

2022/03/15. The costing basis (US\$) and investment parameters are summarized in Table 1.

*Table 1. Costing basis for economic analysis*

<b>Specifications of investment parameters</b>	
The economic life of the project	25 years
Tax rate	30%/year
The desired rate of return/Interest rate	20%/year
Salvage value	20% of initial capital cost
Depreciation method	Straight line
Project capital escalation	5%/year
Products escalation	5%/year
Raw material escalation	3.5%/year
Operating and maintenance labor escalation	3%/year
Utility escalation	3%/year
Working capital percentage	5%/year
Operating supplies	10% of maintenance/year
Laboratory charges	25% operating labor/year
Facility overhead	50% of operating labor and maintenance costs/year
G&A expenses	8% of subtotal operating costs/year
Facility type	Chemical processing facility
Operating mode	Continuous processing
Length of the start-up period	20 weeks
Process fluids	Liquids, gases, and solids
<b>Prices of chemicals (US\$/kg)</b>	
Apple seeds	0.000 <sup>a</sup>
Methanol	0.267
CO <sub>2</sub>	0.0059
Biodiesel	≤0.970
Apple seed meal	0.260
Wastewater treatment	0.091
<b>Prices of utility (US\$/MJ)</b>	
Fired heat (1000 °C)	3.5
High pressure (HP) steam	2.5
Low pressure (LP) steam	2.2
Refrigerante (Propane)	21.2
Electricity	0.0775 <sup>b</sup>

<sup>a</sup>Apple waste currently is without value in the market; <sup>b</sup>US\$/kWh.

This study considered the zero feedstock price since apple seeds were a waste (Table 1). The costs of drying apple pomace and separating the seeds might be included in the biorefinery feedstock price, depending on the applied apple processing industry technology. The transport cost should be neglected because the

biorefinery would be close to the apple processing facility. The trading CO<sub>2</sub> price of 0.0059 US\$/kg was used to promote emissions trading systems. The price of fossil diesel on the global market ranges from 0.97 US\$/kg to 1.88 US\$/kg [41], so the price of biodiesel must be lower. Defatted apple seed meal can be used to enrich wheat bread [42], as cattle feed [16,43], or incorporated in the chewing gum system [44]. In this study, apple seed meal was considered as cattle feed.

#### *Environmental impact assessment basis*

The PEIs of the biodiesel production processes from apple seeds were assessed with the waste reduction algorithm (WAR<sup>®</sup> v.1.0.17, United States Environmental Protection Agency, Washington, DC, USA). WAR<sup>®</sup> is a tool for rapid analysis of a product's life cycle during the conceptual and design stages. Total PEI was calculated as the sum of eight PEI categories: human toxicity potential by ingestion (HTPI), human toxicity potential by dermal and inhalation exposure (HTPE), terrestrial toxicity potential (TTP), aquatic toxicity potential (ATP), global warming potential (GWP), ozone depletion potential (ODP), photochemical oxidation potential (PCOP), and acidification potential (AP). The lower PEI, the environmental friendliness process is. Each component in the process stream contributes to each category through the mass flow rate and chemical potency. Category scores were normalized, and their weighting factors were set to 1.0 to eliminate bias in the PEI calculation. Energy balance data must also be specified to evaluate the energy consumption rate from fossil sources. In the present study, processes were assumed to be natural gas-based.

## RESULTS AND DISCUSSION

### Process design

The flowsheet and main streams table of the biodiesel production from apple seed is presented in Figure 2. The process consists of the following steps: SC-CO<sub>2</sub> oil extraction, SC biodiesel production, methanol recovery, and biodiesel separation. First, the apple seeds were crushed (CRUSHER). The particle size distribution of the obtained apple seed powder was taken from elsewhere [34].

Then, CO<sub>2</sub> previously compressed (COMP) at 24 MPa and heated (HX-1) at 40 °C, combined with the recycled CO<sub>2</sub>, was used to SC extract the oil from the apple seed powder (SCE-1/SCE-2). The oil was removed from the residual seed meal by centrifugation (CTFG). Next, apple seed oil and methanol were transferred to the SC methanolysis reactor (R-1). Both

methanol and oil were pressurized (P-1 and P-2) and heated (HX-2, HX-3, and HX-4) before the methanolysis stage (20 MPa, 350 °C).

A standard molar ratio (42:1) of methanol and apple seed oil was used. Methanol was recovered using a flash distillation unit (FLASH), colled (HX-5), and recycled. The residual reaction mixture was first depressurized (V-1) and cooled (HX-6), and then the methanol/glycerol mixture was separated from the biodiesel phase by a gravitational decanter (DECANTER). Thermodynamic calculations determined the simulated biodiesel product specifications (Table 2) in Aspen Plus<sup>®</sup>.

The European biodiesel standards (EN 14214) were not met in simulated specifications, except for the density and cetane number (Table 2). However, significantly better physicochemical properties were reported [36]. This inconsistency resulted from the difference in assumptions adopted for biodiesel composition. The simulated biodiesel was presented as methyl linoleate, while its physicochemical properties were calculated empirically. Moreover, empirically calculated biodiesel values were based on the mean values of fatty acid methyl esters determined for apple seed oil samples extracted using *n*-hexane. Thus, more studies were needed to specification apple seed oil obtained from other extraction techniques (*i.e.*, SC extraction).

### Cost estimation

Figure 3 shows the fixed capital and production costs distribution for apple seed oil-based biodiesel production. As shown in Figure 3a, the oil extraction facility was the most expensive, contributing 47% of the total fixed capital cost. The utility costs were the highest fraction of the total production costs (Figure 3b). The most cost-impacting factors were electricity and LP steam. The oil extraction unit consumed electricity significantly, while the biodiesel production unit spent LP steam. A heuristic (discovery) model was used for the techno-economic analyses, and therefore the heat integration was not implemented here. The contributions of raw material were found to be negligible. The results showed that raw material costs derived only on methanol costs; the apple seeds as waste were priceless while CO<sub>2</sub> was recycled. Several other SC biodiesel processes have higher raw material costs due to the higher price of the employed oily feedstock [48-50]. The annual capital costs were 2.82 US\$ million, which were significantly lower than the capital cost of *Jatropha* and waste canola of ~32 US\$ million [48,49] or waste frying oil of 35 US\$ million [51]. However, the reported studies were related to a higher biodiesel annual capacity of 40000 tons. Also, these

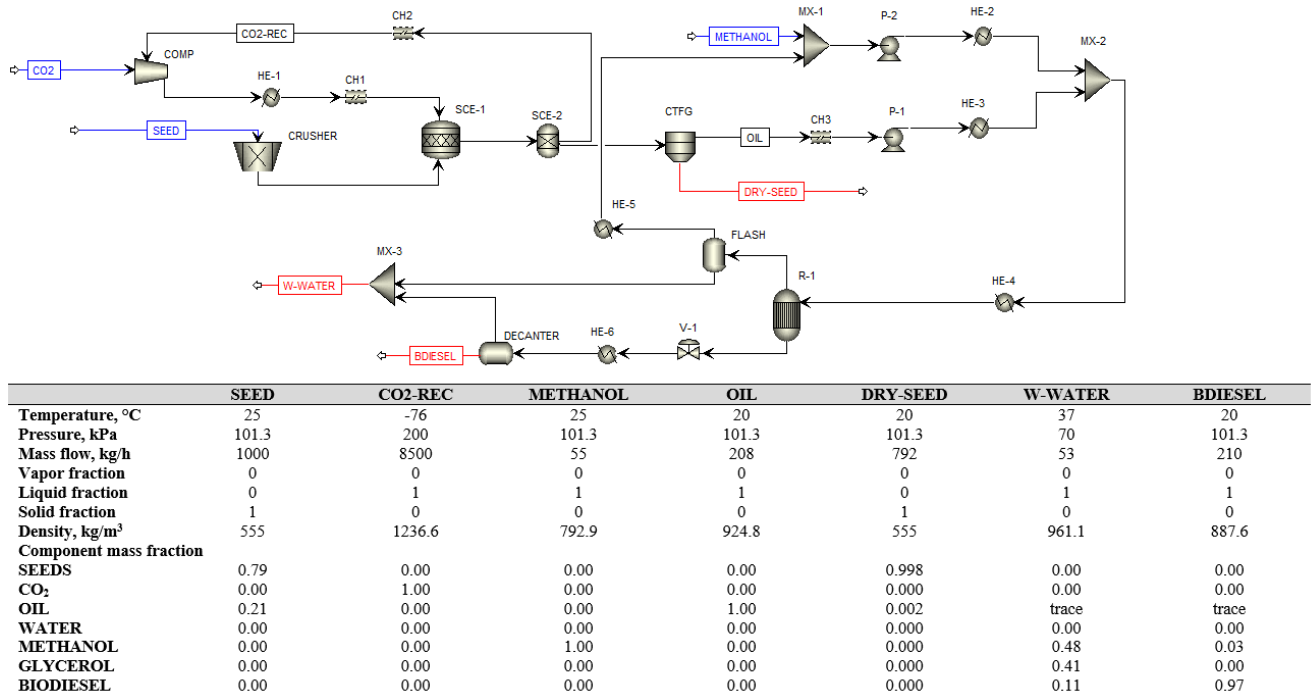


Figure 2. SC biodiesel production from apple seed.

Table 2. Physicochemical properties of the simulated apple seed oil and biodiesel

Property	Oil		Biodiesel		EN 14214
	Simulated	Experimental	Simulated	Experimental	
Density, kg/m <sup>3</sup>	924.9 <sup>a</sup>	921.9 <sup>a</sup>	891 <sup>b</sup>	881 <sup>b</sup>	860-900 <sup>b</sup>
Viscosity	49.8 <sup>c</sup>	-	2.28 <sup>d</sup>	4.12 <sup>d</sup>	3.5-5.0 <sup>d</sup>
Iodine value, g J <sub>2</sub> /100 g	-	1.29	-	126.9	≤120
Saponification value, mg KOH/g oil	-	186.5			
Refractive index <sup>a</sup>	1.46	1.47			
Flash point, °C			27.5	-	≥101
(Palmitic acid) C16:0		13.39			
(Stearic acid) C18:0		7.69			
(Oleic acid) C18:1		34.84			
(Linoleic acid) C18:2		63.76			
(Linolenic acid) C18:3		1.61			
(Arachidic acid) C22:0		2.04			
Cetane number			51.4	50.4	≥51
Oxidative stability (110 °C), h			-	4.48	6 min
Reference	This study	[34,16]	This study	[36]	

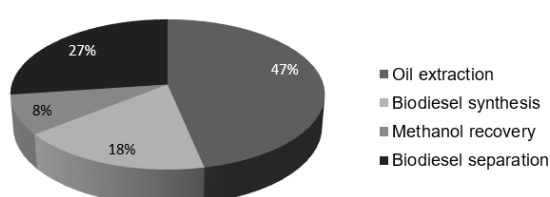
<sup>a</sup>At 20 °C; <sup>b</sup>at 15 °C; <sup>c</sup>at 20 °C, mPas; <sup>d</sup>at 40 °C, mm<sup>2</sup>/s.

studies evaluated biodiesel production from oil, while the present study included oil extraction.

Concerning reactants used in this process, little waste was generated. Wastewaters (W-WATER) were sent to the treatment facility, while the residual apple seed meal (DRY-SEED) could be discharged in the field as fertilizer or used as cattle feed. Considerable amounts of protein, fiber, and toxigenic amygdalin (source of cyanide anions) can be found in apple seed residues [43]. Amygdalin is the glucoside occurring in apple seeds at contents of approximately 0.2% [45].

During the processing, releases of cyanide from apple seeds amygdalin to the environment (0.06 g/g of theoretical yield) may occur [46]. While the nutritional value of apple seed meal protein is low, clinical studies regarding the toxic doses of amygdalin have been conducted only with rats and mice. Amygdalin at a moderate dose can increase protein digestibility in rats [43] and improve oxidative balance in mice [47]. However, little is known about the therapeutic doses of apple seed meal in animals, and therefore its use as a cattle feed has not been revealed and waits for its official approval.

a) Fixed capital costs (1.26 US\$ millions)



b) Total production costs (2.82 US\$ millions)

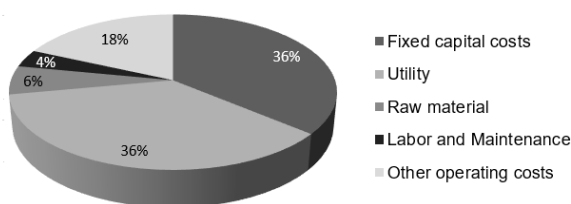


Figure 3. Distribution of (a) fixed capital and (b) total production costs.

### Profitability analysis

A biodiesel production cost of 0.96 US\$/kg was calculated based on the total annual production cost (2.82 US\$ million) and the produced biodiesel capacity (1840 tons/year). The wastewater was considered as a cost, while biodiesel brought revenues. In this study, the revenues from the sale of apple seed meal as cattle feed were also considered. The annual selling revenue was 1.72 US\$ million and 3.53 US\$ million for biodiesel (0.96 US\$/kg) and biodiesel/apple seed meal sales, respectively. Table 3 shows the profitability measures for the SC biodiesel processes from several oily feedstocks. The NPV of the apple seed facility was positive and higher than those of the other two oily feedstocks. Several investigators [23,52,38] have designed facilities with a higher annual capacity (8000 tons of biodiesel) than the facility considered in the present study for the same

feedstock mass flow because the previous studies were based on the oil mass flow and the present study on the seed mass flow. Therefore, the capacity of the facility based on apple seed was increased by 440% and 810% to produce 8000 and 30000 tons/year of biodiesel, respectively, and compared to those based on castor and waste canola oil (Table 3). With increasing the facility capacity, NPVs increased while the payback period decreased. This trend was significant when the revenues from the sale of apple seed meal were included in analyzing the facility's profitability.

Food waste biorefineries have a higher (25 years) lifetime period [40]. Positive ROI (return of investment) and payback period below 15 years make the food waste biorefinery attractive for investment [40]. With a payback period of 8 years (Table 3), the apple seed-based biodiesel facility was considered economically profitable.

Table 3. The profitability measures of a biodiesel facility

	This study						Castor oil [24]	Waste canola oil [49]
	Biodiesel			Biodiesel & Apple seed meal			Biodiesel & Glycerol	
Revenues								
Annual facility capacity, tons	1840	8000	30000	1840	8000	30000	8000	30000
NPV, US\$ millions	1.99	35.8	152	5.36	46.9	164	4.16	21.07
ROI, %	12.58	94.3	128.2	55.9	-	-	20	23.81
Payback period, year	7.95	1.06	0.78	1.79	0	0	5.00	4.2

### Sensitivity analysis

Sensitivity analyses were conducted to investigate the sensitivity of the NPVs and payback period to changes in a variety of parameters. Two

Table 4. Sensitivity analysis on a biodiesel production cost

	-40%	-30%	-20%	-10%	Base case	10%	20%	30%	40%
Apple seed, US\$/kg	-	-	-	-	0	0.10	0.20	0.30	0.40
Biodiesel, US\$/kg	0.58	0.68	0.77	0.87	0.96	1.08	1.21	1.38	1.62

Any increase in the price of apple seeds, at a selling price of biodiesel of 0.96 US\$/kg, would lead to the unprofitability of the facility. However, for a biodiesel price of 1.38 US\$/kg, the apple seeds price could increase by 10% (the NVP of 1.28 US\$ million and the payback period of 12.6 years). Therefore, a further increase in the apple seed price would lead to economic unfeasibility. On the other hand, biodiesel price could be decreased to 0.87 US\$/kg, without costs for apple seeds (Figure 4a). The best scenario, not considered in this study, is that price of waste is negative because it imposes several

environmental problems; therefore, removing them from the environment incurred negative costs. In that case, the final biodiesel cost will again reduce.

However, if apple seed meal were included as revenue, biodiesel price could be decreased to 0.39 US\$/kg with an increase in apple seed price by 10% (Figure 4b). The suggested biodiesel production facility was profitable since the payback period varied from 2 to 12 years. However, this process could be, in the future, highly dependent on the apple seed price.

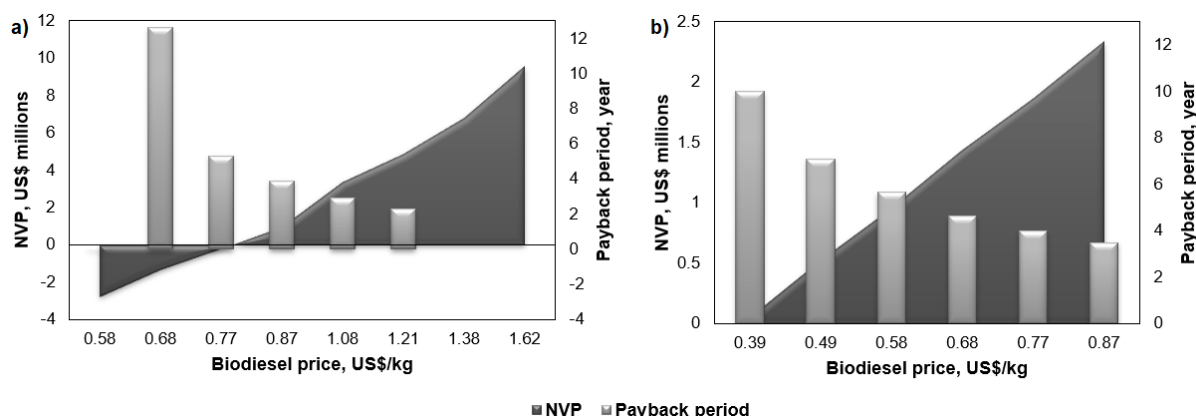


Figure 4. Influence of biodiesel price on process profitability.

Retail diesel prices were 0.97 US\$/kg to 1.88 US\$/kg [41], which means that biodiesel from apple seed (0.39 US\$/kg to 1.21 US\$/kg) was comparative to commercial diesel. Biodiesel price was in the range from 0.5 US\$/kg for waste cooking oil [53] to 2.0 US\$/kg for palm oil [54], depending on the production technology. Generally, SC technologies have a biodiesel selling price of 0.48 US\$/kg [55] to 1.53 US\$/kg [56]. The use of whole apple pomace to produce bioethanol was cost-competitive; the reported apple pomace-based bioethanol price in 1996 was 0.20 US\$/kg [57].

### Environmental impact assessment

A comparative assessment of the PEIs generated within the system, including the energy effect, was investigated to identify the major contributors of biodiesel production from apple seeds to the environmental outcomes. Figure 5 shows that if apple seed meal was used as cattle feed, PEI of the process was much lower than the PEI of the process, which treated apple seed meal as waste. The highest contributor to the PEI was AP because of the high content of biodegradable proteins and fibers. The high consumption of fossil

fuels could also increase AP. On the other hand, a high PCOP in waste apple seed meal may be explained by the presence of volatile hydrogen cyanide, which may produce photochemical smog.

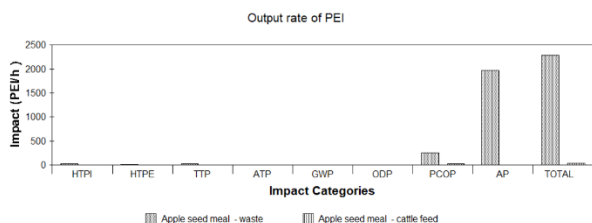


Figure 5. Influence of biodiesel price on process profitability.

The total environmental impact of biodiesel production from apple seeds was 2290 PEI/h and 384 PEI/h, with and without treating apple seed meal as waste. Biodiesel production processes from green seed canola oil and waste vegetable oils show a lower total environmental impact of 27.3 PEI/h [23] and 58.7 PEI/h [58], respectively. Except process using waste vegetable oils and fats [21,22,25,26], low PEIs values of the green seed canola oil process do not reveal it as environmentally friendly because oil extraction is excluded in the analysis. The same situation is with the processes that excluded extraction steps from palm, *Jatropha*, and microalgae [26]. Furthermore, treating apple seed meal as waste gave positive pollution risks to humans and land, as shown by the HTPI, HTPE, and TTP indexes (Figure 5). These indexes have a mitigation effect on humans and animals.

## CONCLUSION

The use of apple seed from waste apple pomace as a biodiesel feedstock is at an early stage of development. Huge worldwide available quantities of apple pomace and less resource-intensive processes (such as the process presented in this study) are promising elements to prove the viability of the food waste biorefinery concept. The main advantages of using apple seeds are that waste apple pomace is a no or low-cost feedstock. Apple seed oil has not been used for biodiesel purposes. So, the present study is an improved way of valorizing apple seeds. The biodiesel price suggested by this study (0.39 US\$/kg - 0.96 US\$/kg) made this apple seed valorization path a cost-competitive technology. This paper demonstrated that the biodiesel production process from apple seeds was environmentally favorable only if apple seed meal was treated as cattle feed. High energy demand contributed

to the high possibilities for acidification, thus indicating the need for heat integration. Also, the experimental-based apple seed biorefinery is still challenging. Furthermore, apple seed meal should wait for an official proof as cattle feed.

## Acknowledgment

The Republic of Serbia financially supported this work - Ministry of Education, Science and Technological Development, Program for financing scientific research work, number 451-03-68/2022-14/200133 (assigned to the Faculty of Technology, Leskovac, University of Niš, researchers' group III 45001).

## REFERENCES

- [1] FAOSTAT n.d. <http://www.fao.org/faostat/en/#home> (accessed March 14, 2021).
- [2] S. Bhushan, K. Kalia, M. Sharma, B. Singh, P. Ahuja, *Crit. Rev. Biotechnol.* (2008) 285-96.
- [3] F. Vendruscolo, F. Koch, L. Pitol, J. Ninow, *Rev. Bras. Tecnol. Agroindustrial.* (2007) 53-57.
- [4] N. O'Shea, A. Ktenioudaki, T. Smyth, P. McLoughlin, L. Doran, M. Auty, E. Arendt, E. Gallaghery, *J. Food. Eng.* (2015) 89-95.
- [5] Y. Hang, E. Woodams, *Biotechnol. Lett.* (1984) 763-764.
- [6] H. Liu, V. Kumar, L. Jia, S. Sarsaiya, D. Kumar, A. Juneja, Z. Zhang, R. Sindhu, P. Binod, S. Bhatia, M. Awasthi, *Chemosphere* (2021) 131427.
- [7] R. Walter, R. Sherman, *J. Agric. Food. Chem.* (1975) 1218.
- [8] W. Jewell, R. Cummings, *J. Food. Sci.* (1984) 407-410.
- [9] Y. Hang, C. Lee, E. Woodams, *J. Food. Sci.* (1982) 1851-1852.
- [10] Q. Jin, N. Qureshi, H. Wang, H. Huang, *Fuel.* (2019) 536-544.
- [11] S. Bhushan, S. Gupta, D. Babu, M. Sharma, P. Ahuja (Council of Scientific & Industrial Research, India) US 9 011 952 B2 (2012.).
- [12] M. Fromm, S. Bayha, R. Carle, D. Kammerer, *Eur. Food. Res. Technol.* (2012) 1033-1041.
- [13] S. Taylor, F. Eller, J. King, *Food. Res. Int.* (1997) 365-370.
- [14] W. Kolanowski, M. Zakrzewska, *J. Food. Nutr. Res.* (2019) 92-98.
- [15] R. Yukui, W. Wenya, F. Rashid, L. Qing, *Int. J. Food. Prop.* (2009) 774-779.
- [16] X. Yu, F. Van De Voort, Z. Li, T. Yue, *Int. J. Food. Eng.* (2007).
- [17] M. Walia, K. Rawat, S. Bhushan, Y. Padwad, B. Singh, *J. Sci. Food. Agric.* (2014) 929-934.
- [18] B. Fotschki, A. Jurgoński, J. Juśkiewicz, Z. Zduńczyk, *Zywn. Nauk. Technol. Jakosc.* (2015) 220-231.
- [19] P. Górnaś, M. Rudzińska, D. Segliņa, *Ind. Crops. Prod.* (2014) 86-91.
- [20] S. Isah, G. Ozbay, *Front. Sustain. Food. Syst.* (2020) Article 82.
- [21] L. Chryssikou, V. Dagonikou, A. Dimitriadis, S. Bezergianni,



- J. Clean. Prod. (2019) 566-575.
- [22] Y. Budiman Abdurakhman, Z. Adi Putra, M. Bilad, N. Md Nordin, M. Wirzal, Chem Eng. Res. Des. (2018) 564-574.
- [23] C. Baroi, A. Dalai, Fuel. Process. Technol. (2015) 105-119.
- [24] A. Dimian, P. Iancu, V. Plesu, A. Bonet-Ruiz, J. Bonet-Ruiz, Chem. Eng. Res. Des. (2019) 198-219.
- [25] V. Marulanda, J. Clean. Prod. (2012) 109-116.
- [26] L. Rincón, J. Jaramillo, C. Cardona. Renew. Energy. (2014) 479-487.
- [27] L. Hernández-Pérez, E. Sánchez-Tuirán, K. Ojeda, M. El-Halwagi, J. Ponce-Ortega, ACS Sustain. Chem. Eng. (2019) 8490-8498.
- [28] M. Fernández Barajas Life cycle analysis of grapeseed oil biofuel in Spain, Master thesis. Universidad Politécnica de Madrid, School Of Mines And Energy, E.T.S.I de Minas y Energía, 2018.
- [29] S. Karatay, E. Demiray, G. Dönmez, Biomass. Convers. Biorefinery (2020).
- [30] S. Qin, B. Shekher Giri, A. Kumar Patel, T. Sar, H. Liu, H. Chen, A. Juneja, D. Kumar, Z. Zhang, M. Awasthi, M. Taherzadeh, Bioresour. Technol. (2021) 124496.
- [31] V. Sriram, J. Jeevahan, A. Poovannan, Int. J. Ambient. Energy (2017) 54-56.
- [32] A. Yadav, M. Emran Khan, A. Pal, Int. J. Oil Gas. Coal. Technol. (2019) 473-492.
- [33] M. Awasthi, J. Ferreira, R. Sirohi, S. Sarsaiya, B. Khoshnevisan, S. Baladi, R. Sindhu, P. Binod, A. Pandey, A. Juneja, D. Kumar, Z. Zhang, M. Taherzadeh, Renew. Sustain. Energy Rev. (2021) 110972.
- [34] G. Ferrentino, S. Giampiccolo, K. Morozova, N. Haman, S. Spilimbergo, M. Scampicchio, Innov. Food Sci. Emerg. Technol. (2020) 102428.
- [35] F. Montañés, O. Catchpole, S. Tallon, K. Mitchell, D. Scott, R. Webby, J. Supercrit. Fluids (2018) 128-136.
- [36] P. Górnaś, M. Rudzińska, Ind. Crops Prod. (2016) 329-338.
- [37] S. Saka, D. Kusdiana, Fuel (2001) 225-231.
- [38] A. West, D. Posarac, N. Ellis, Bioresour. Technol. (2008) 6587-6601.
- [39] S. Martynov, S. Brown, H. Mahgerefteh, Greenh. Gases Sci. Technol. (2013) 136-147.
- [40] J. Cristóbal, C. Caldeira, S. Corrado, S. Sala, Bioresour. Technol. (2018) 244-252.
- [41] J. Lee, B. Lee, Y. Ok, H. Lim, Bioresour. Technol. (2020) 123086.
- [42] M. Purić, B. Rabrenović, V. Rac, L. Pezo, I. Tomašević, M. Demin, LWT (2020) 109391.
- [43] P. Opyd, A. Jurgoński, J. Juśkiewicz, J. Milala, Z. Zduńczyk, B. Król, Nutrients (2017) 1091.
- [44] R. Gunes, I. Palabiyik, O. Toker, N. Konar, S. Kurultay, J. Food Eng. (2019) 9-14.
- [45] I. Bolarinwa, C. Orfila, M. Morgan, Food Chem. (2015) 437-442.
- [46] ECETOC, Cyanides of Hydrogen, Sodium and Potassium, and Acetone Cyanohydrin, JACC, Brussels (2007.).
- [47] S. Albogami, A. Hassan, N. Ahmed, A. Alnefaie, A. Alattas, L. Alquthami, A. Alharbi, Peer J. (2020) e9232.
- [48] N. Yusuf, S. Kamarudin, Energy Convers. Manag. (2013) 710-717.
- [49] S. Lee, D. Posarac, N. Ellis, Chem. Eng. Res. Des. (2011) 2626-2642.
- [50] A. Deshpande, G. Anitescu, P. Rice, L. Tavlarides, Bioresour. Technol. (2010) 1834-1843.
- [51] J. Marchetti, A. Errazu, Energy Convers. Manag. (2008) 2160-2164.
- [52] Y. Zhang, M. Dubé, D. McLean, M. Kates, Bioresour. Technol. (2003) 1-16.
- [53] T. Sakai, A. Kawashima, T. Koshikawa, Bioresour. Technol. (2009) 3268-3276.
- [54] K. Jegannathan, C. Eng-Seng, P. Ravindra, Renew. Sustain. Energy Rev. (2011) 745-751.
- [55] F. Gutiérrez Ortiz, P. de Santa-Ana, J. Supercrit. Fluids (2017) 349-358.
- [56] H. Taher, A. Giwa, H. Abusabiekeh, S. Al-Zuhair, Fuel Process. Technol. (2020) 106249.
- [57] V. Joshi, D. Sandhu, Bioresour. Technol. (1996) 251-255.
- [58] S. Morais, S. Couto, A. Martins, T. Mata, Comput. Aided Chem. Eng. (2010) 253-258.

MARIJA B. TASIĆ <sup>1</sup>

MIONA S. STANKOVIĆ <sup>1</sup>

MILAN D. KOSTIĆ <sup>1</sup>

OLIVERA S. STAMENKOVIĆ <sup>1</sup>

VLADA B. VELJKOVIĆ <sup>1,2</sup>

<sup>1</sup> Univerzitet u Nišu, Tehnološki fakultet, Leskovac, Serbia

<sup>2</sup> Srpska akademija nauka i umetnosti, Beograd, Srbija

## CIRKULARNA EKONOMIJA U INDUSTRIJI PRERADE JABUKA: PROIZVODNJA BIODIZELA IZ OTPADNIH SEMENA JABUKA

*Trop jabuke je čvrsti otpad industrije prerade jabuka. Da bi podstakla održivost, industrija prerade jabuka mora da primeni model cirkularne ekonomije biorafinerije i da tretira trop jabuke kao vredan izvor ulja semena jabuke. Po prvi put, ovo istraživanje se bavilo projektovanjem, ekonomikom i procenom uticaja proizvodnje biodizela iz ulja semena jabuke dobijenog iz tropa jabuke na životnu sredinu. Aspen Plus<sup>®</sup> i WAR<sup>®</sup> su softveri, korišćeni za projektovane i procenu proizvodnje biodizela. Glavne proizvodne faze bile su superkrična CO<sub>2</sub> ekstrakcija, metanoliza ulja semena jabuke, regeneracija metanola i separacija biodizela. Predviđeno je da proizvodni pogon prerađuje 24 tone semena jabuke dnevno. Ukupni kapitalni i proizvodni troškovi bili su 1,26 miliona US\$ i 2,82 miliona US\$, respektivno. Ako bi se uračunali prihodi od prodaje sačme semena jabuke kao stočne hrane, cena biodizela bi mogla biti 0,39 US\$/kg. Proces je bio ekološki prihvatljiv kada se sačma semena jabuke nije tretirala kao otpad.*

*Ključne reči: seme jabuka, Aspen Plus<sup>®</sup>, biodizel, ekonomija, superkrična tehnologija, WAR<sup>®</sup>.*

NAUČNI RAD



THAYAMMAL  
GANESAN ARUL <sup>1</sup>  
VARATHARAJU PERUMAL <sup>2</sup>  
RAJASEKARAN  
THANIGAIVELAN <sup>3</sup>

<sup>1</sup> St Mary's Engineering  
College, Hyderabad, Telangana,  
India

<sup>2</sup> Department of Automobile  
Technology, Ethiopian Technical  
University, Addis Ababa, Ethiopia

<sup>3</sup> Department of Mechanical  
Engineering, Muthayammal  
Engineering College, Rasipuram,  
India

SCIENTIFIC PAPER

UDC 544.6:54:543

## PERFORMANCE STUDY OF ELECTROCHEMICAL MICROMACHINING USING SQUARE COMPOSITE ELECTRODE FOR COPPER

### Article Highlights

- In this research, an attempt is made to fabricate a micro-square hole on the copper workpiece
- Stainless steel and aluminum composite square electrode are considered for the EMM experiments
- Aluminum composite square electrodes show a significant effect on the accuracy of the micro-square hole

### Abstract

*The use of micro components is increasing day by day in the industries such as aviation, power circuit boards, inkjet nozzle, and biomedical. Among various non-traditional micromachining methods, electrochemical micromachining (EMM) shows unique characteristics, such as no tool wear, no residual stress, and high accuracy. In this research, EMM is considered to study the effect of square-shaped stainless steel (SS) and aluminum metal matrix composite (AMC) tools on square hole generation. The significant process parameters, such as machining voltage, duty cycle, and aqueous sodium nitrate (NaNO<sub>3</sub>) electrolyte of varying concentrations, are considered for the study. The performances of the EMM process are evaluated in terms of machining rate (MR) and Overcut (OC). The AMC tool shows 43.22% lesser OC than the SS tool at the parameter combinations of 8 V, 85%, and 23 g/L. Also, the same parameter combination MR for the SS tool is 71.6% higher than the AMC tool. Field emission scanning electron microscope image (FESEM) analysis shows that the micro square hole generated using composite electrode shows micro-pits on the circumference of the square hole. The energy-dispersive X-ray spectroscopy (EDAX) analysis is conducted to verify the presence and distributions of reinforcement in the AMC tool.*

*Keywords: square tool electrode, composite electrode, electrochemical micromachining, copper.*

The application of micro features, such as micro square holes, micro grooves, taper surfaces, slots, micro holes, and micro slits, was increasing enormously in microelectromechanical systems (MEMS). Also, micromachining plays a significant role

in manufacturing due to the miniaturization of electronic, medical, biomedical, and automobile devices [1-4]. The documented knowledge in EMM for generation micro features is archived for micro holes. In line with that, Pradeep *et al.* [5] studied the performance of EMM using cryogenically treated graphite electrodes on SS 304. The use cryogenic treated tool shows good stray current protection and improves the accuracy of the micro-hole. Soundarrajan *et al.* [6] have utilized geometrically modified and coated electrodes on copper work material in the EMM process. They reported that electrode size (in length) contributes to the higher MR. The ceramic and hot melt glues are significantly improving the overcut and MR.

Correspondence: R. Thanigaivelan, Department of Mechanical Engineering, Muthayammal Engineering College, Rasipuram-637408, Namakkal (Dt), India.  
E-mail: [tvelan10@gmail.com](mailto:tvelan10@gmail.com)  
Paper received: 1 May, 2021  
Paper revised: 10 October, 2021  
Paper accepted: 19 October, 2021

<https://doi.org/10.2298/CICEQ210501036A>

Liu *et al.* [7] used a rotating helical electrode in EMM on SS 304 and improved the electrolyte flow in the machining zone. Kishi *et al.* [8] fabricated rectangular grooves with rotary electrodes in a hybrid electro-discharge and electrochemical machining process. The rotary motion of the electrode significantly improves the surface roughness from 3.82  $\mu\text{m}$  to 0.86  $\mu\text{m}$  on the machined area. Ayyappan *et al.* [9] studied the performance of EMM with abrasive and epoxy coated tools. The epoxy-coated tools were found to reduce the overcut, and also, the spark production in the inter-electrode gap was decreased significantly, resulting in a good quality micro-hole. Maniraj *et al.* [10] performed experiments with the heated electrode in EMM for machining micro holes on AMC. The heated electrode initiates the micro stirring effect at the machining zone and significantly enhances the machining performance. Arab *et al.* [11] studied the influences of tool roughness on the machining accuracy of the ECDM process. They noticed the higher surface roughness of the tool increases the overcut and reduces the accuracy of the hole. Geethapriyan *et al.* [12] conducted the experiments using copper and brass electrodes on the EMM of SS 420. They have reported that the copper electrode produces the 20.9% and 29.65% higher MR and overcut, respectively, than the brass electrode. Pang *et al.* [13] proposed the floating tool electrode in ECM to maintain a constant electrode gap between tool and work. The results obtained in modeling and experimental correlate with each other. Paczkowski *et al.* [14] investigated the EMM with a vibrated electrode on alloy tool steel. They have noticed that the kinetic movements of the electrode significantly improve the machining rate and production efficiency. Thanigaivelan *et al.* [15] fabricated the micro holes on SS 304 using flat, conical, wedge, and round-ended tools. They found uniform current distributions with the conical-shaped electrode than the other tools, enhancing machining performance. Sandip *et al.* [16] fabricated the micro slots using EMM on the titanium work material. The literature clarifies that many techniques are endeavored by the researchers in EMM with different tools from different perspectives.

Usually, square holes are fabricated in the electro-discharge machining process. However, a direct attempt at micro-square hole fabrication in EMM is attempted due to the inherent drawback of tool electrode wear. Hence, two different electrode materials, SS and AMC, of the same specifications are considered to generate the micro square hole. Generally, composite electrodes are used in wastewater treatments, electrochemical depositions,

and batteries for various applications due to their effective mechanical and electrical properties [17-19]. Therefore, the accuracy and MR for both the electrodes are compared by varying process parameters such as electrolyte concentration, machining voltage, and duty cycle. Furthermore, the scanning electron microscope image and EDAX analysis were carried out to study the impact of the electrode on the micro-square hole surfaces.

## MATERIALS AND METHODS

An indigenously developed EMM setup shown in Figure 1 is used for conducting the experiments.

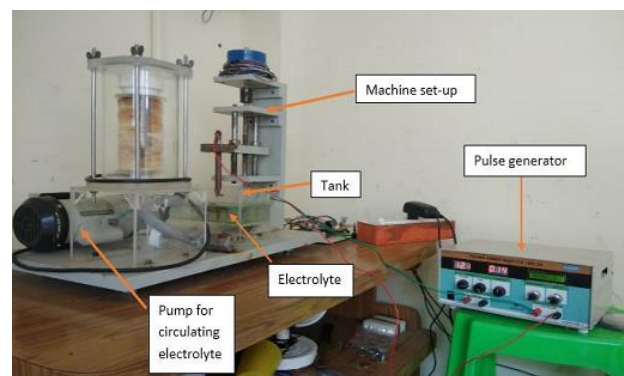


Figure 1. Experimental setup.

The setup included an electrolyte supply system, tool feeding system, microcontroller unit, and pulse rectifier. The stepper motor maintains the inter-electrode gap [IEG] between the tool and the electrode. The IEG is held at 40  $\mu\text{m}$  with the help of a stepper motor, microcontroller, and tool feeding arrangements. The electrolyte supply system consists of a pump and filter. The used electrolyte is continuously pumped, filtered, and re-circulated to the machining chamber. Copper finds a wide range of applications in various sectors. Hence, a 2 mm thick copper plate is considered a workpiece. The workpiece is clamped in the workpiece holder made up of acrylic material. The work holder consists of two blocks that are fastened with a bolt by keeping the work material between them. Two types of square tools are prepared for the size of 1 mm x 1mm in AMC and SS 304 material. The AMC is prepared through a stir casting furnace made up of Al6063 alloy is reinforced with 12% SiCp and 5% graphite particles. The chemical composition of Al6063, SiCp, and graphite particles are presented in Tables 1, 2, and 3, respectively [20]. SODICK CNC wire cut EDM is used to prepare the square tool. The voltage in the range of 8 to 12 V, duty cycle in the range of 50% to 90%, and electrolyte concentration in the range of 21 g/L to 29 g/L are considered for the study. The experimental plan

Table 1. Chemical composition of Al6063 Alloy

Elements	% of compositions
Al	98.640
Mg	0.514
Si	0.535
Cu	0.001
Mn	0.028
Fe	0.211
Zn	0.004
Cr	0.001
Ti	0.011
Ca	0.051

Table 2. Chemical composition of SiCp

Elements	% of compositions
SiC	96
Fe	0.2
SiO <sub>2</sub>	0.8
Si	0.5
C	0.6
Al	0.2
Ca	0.65
Mg	1.05

Table 3. Chemical composition of graphite

Elements	% of compositions
C	55.2
O	24.5
Ca	8.4
Si	7.5
Fe	1.3
Al	1.7
Mg	0.8

follows the varying one parameter at a time design. The aqueous sodium nitrate electrolyte of different concentrations is used in the experiments. The electrolyte is prepared using distilled water and sodium nitrate salts. For example, to prepare electrolyte concentration of 20 g/L, the sodium nitrate salt of 20 g is mixed in 1 L of distilled water and stirred well. The pulse frequency is kept at a constant value of 50 Hz, while the thickness of the workpiece and the size of the square electrode are maintained constant, as mentioned throughout the experiments.

Figure 2 presents the SEM images of tool

electrodes. The EDAX test is carried out on the fabricated tools to analyze the composition and distribution of reinforcement.

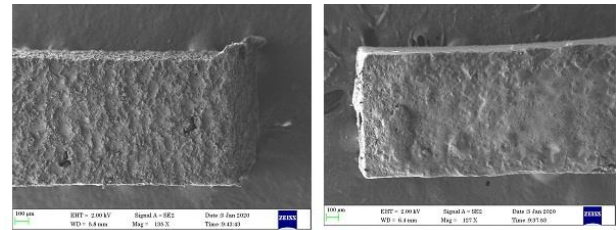


Figure 2. SEM image of tool (a) SS (b) AMC.

The EDAX test confirms the homogeneous distributions of reinforcements, as shown in Figure 3 for the AMC tool. The machining rate (MR) and overcut (OC) are considered to evaluate performance measures. The MR is calculated using the total machining time required for producing through the hole. The differences between the bottom area of the tool and the machined hole area are considered for the overcut. The optical microscope was used to calculate the overcut area of the square hole.

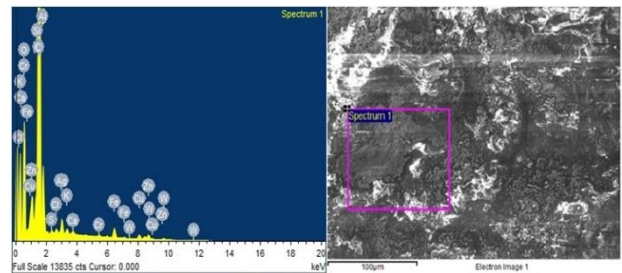


Figure 3. EDAX image of AMC tool.

## RESULTS AND DISCUSSION

### Influences of machining voltage on OC and MR

Figure 4 represents the influences of machining voltage on OC for the SS and AMC tools. According to the graph, SS and AMC tools create an OC of 1763  $\mu\text{m}$  and 1231  $\mu\text{m}$ , respectively, with a parameter combination of 8 V, 85%, and 23 g/L. Graphite reinforcement particles play a vital role in lower OC in the AMC tool. The aluminum material is a good electrical conductor, and reinforcements alter the conductivity of the AMC electrode. The presence of graphite and silica in the AMC tool reduces the conductivity of the electrode leading to lesser overcut. The AMC tool shows 43.22% lesser OC than the SS tool, and also this is the least OC value among all the experiments. Also, the parametric combinations 9 V, 85%, and 23 g/L produce 37.72% less OC than the SS tool, the second least OC among the experiments. The

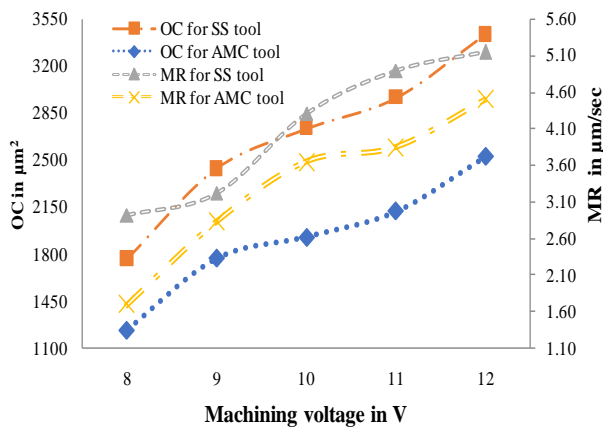


Figure 4. Influence of Machining voltage on OC & MR.

SEM images in Figure 5 show the square micro hole machined through AMC and SS tools, respectively, at the parameter combination 8 V, 85%, and 23 g/L. Based on the figure, the AMC tool's micro square hole shows good sharp edges with slight waviness on the circumferences. Also, the circumferences of micro-holes are seen with the micropores. It is because reinforcement particle distributions in the AMC tool alter the machining zone's current distributions. The presence of silica on the surface of the tool induces joule heating in the electrode. The Joule heat value is proportional to the square of the current that occurs in the electrode. This phenomenon creates the rapid sporadic electrolysis between the tool face and the electrode, leading to the development of micropores [10]. The tool shows the circumference with fewer pores and higher curved circumference for micro holes machined with the SS, as displayed in Figure 5. In the SS electrode, the uniform metallographic structure of metals creates a uniform flow of current, contributing to a smooth machining surface.

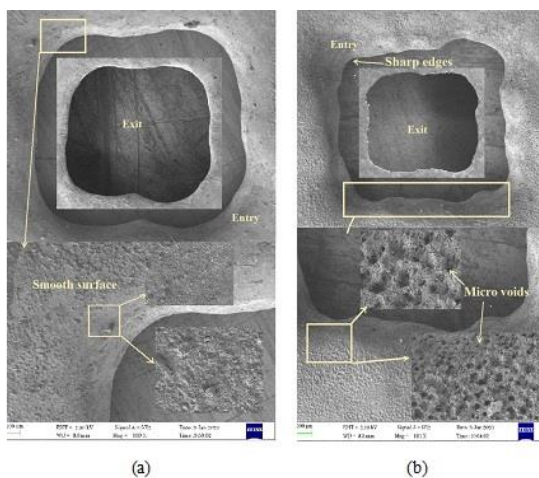


Figure 5. SEM images of the micro holes (a) SS tool (b) AMC tool.

Figure 4 shows the influences of machining voltage on MR for the AMC and SS tools. According to the graph, the SS tool produces higher MR than the AMC tool, and the graph trend indicates that by increasing the machining voltage, MR for both tools increases. The SS and AMC tools produce an MR of 2.908  $\mu\text{m}/\text{sec}$  and 1.693  $\mu\text{m}/\text{sec}$ . The disturbance of current conductivity between the tool and the electrode plays a major role in MR. The SS tool material shows good attraction between the metallic molecules attributing to a smooth current flow at the machining zone. At the same time, the AMC tool has a lesser intermolecular metallic bonding among the molecules [21]. Hence, the uniform current flow in the IEG increases the MR in the SS tool more than in the AMC tool. The SS tool produces around 71.6% higher MR than the AMC tool for the parameter combination of 8 V, 85%, and 23 g/L. Moreover, this is the highest MR of all other conducted experiments.

#### Influences of duty cycle on OC and MR

The influences of SS and AMC tools on the duty cycle are represented in Figure 6.

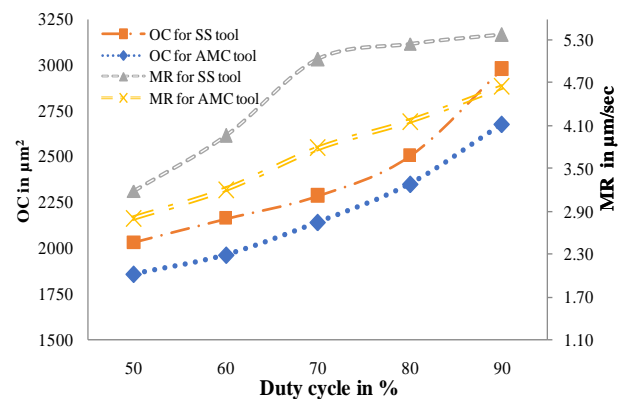


Figure 6. Influence of Duty cycle on OC & MR.

The graph indicates that the OC increases with an increase in duty cycle with respect to both tools. The AMC tool produces 1859  $\mu\text{m}^2$  OC for the parameter combination of 50%, 12 V, 29 g/L. As well as, the SS tool produces 2028  $\mu\text{m}^2$  OC for the same parameter combination, which is 9.1% higher than the AMC tool. The presence of aluminum in the composite provides good electrical conductivity in the electrolyte due to its low specific gravity and density nature [10]. Therefore, the AMC tool produces less OC than the SS tool. Also, the AMC and SS tools produce 2161  $\mu\text{m}^2$  and 1961  $\mu\text{m}^2$  OC, respectively, for the parametric combination of 60%, 12 V, and 29 g/L. The OC is found to be 10.21% lesser than the SS tool. Figure 7 shows an SEM image of a square micro hole machined with the AMC and SS

tools, respectively, for the parameter combination of 50%, 12 V, and 29 g/L. The MR for the SS and AMC tools is 3.189  $\mu\text{m}/\text{sec}$  and 2.8057  $\mu\text{m}/\text{sec}$ , respectively. It is evident from the graph that the SS tool produces a 13.5% higher MR than the AMC tool for the parameter combination of 50%, 12 V, 29 g/L. A higher duty cycle allows more current between the electrodes for a longer duration of time. SS tool continuously produces higher MR such as 15.1% and 23.5% for the 60% and 70% duty cycle, respectively.

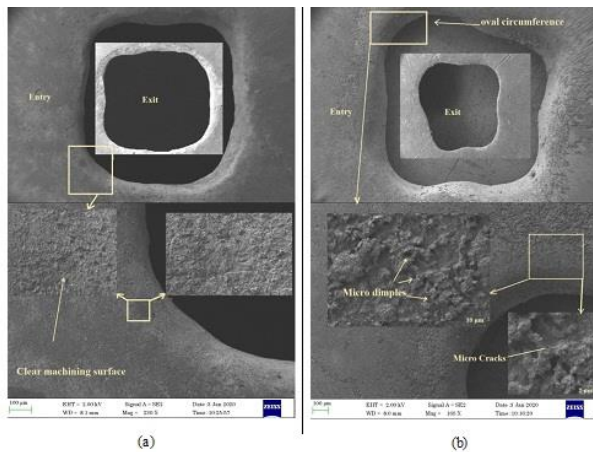


Figure 7. SEM images of the micro holes (a) SS tool (b) AMC tool.

### Influences of electrolyte concentration on OC and MR

Figure 8 presents the influences of electrolyte concentration on OC for the AMC and SS tools. According to the graph, the electrolyte concentration increases the OC for both tools. It is expected that ions in electrolytes increase with the concentration. Between both tools, the AMC tool produces the lower OC of 1808  $\mu\text{m}^2$  at the parameter combination of 21 g/L, 90%, and 12 V. The OC increased gradually from 23 g/L to 30 g/L because the square shape of the tool induces a heating effect in the inter-electrode gap (IEG) due to the electrical potential difference. Continued heat generation in the IEG causes electron energization, resulting in higher sludge formations. This higher sludge formation in the machining zone reduces the IEG, leading to the short circuit and stopping further machining. Therefore, the AMC tool produces a lower OC than the SS tool [10]. Also, the AMC tool produces 14.8% and 20.4% reduced OC for the electrolyte concentrations of 23 g/L and 25 g/L, respectively. Figure 9 shows the micro hole's SEM image machined with the square AMC and SS tools. The outer perimeter of the square hole surface, machined with the AMC tool, exhibits microvoids due to the reactions of byproducts.

The graph indicates that the SS tool produces

32.86% higher MR than the AMC tool for the parameter combination of 21 g/L, 90%, and 12 V. The machining zone's bubble generation contributes to higher MR in the SS tool. The breaking of bubbles generates the micro stirring effect in the electrolyte ensures the renewal of electrolyte at the machining zone periodically [10]. Therefore, the SS tool produces a higher MR than the AMC tool. Also, the electrolyte concentration of 23 g/L and 25 g/L produces 22.4% and 26.2% higher MR with the SS tool than with the AMC tool.

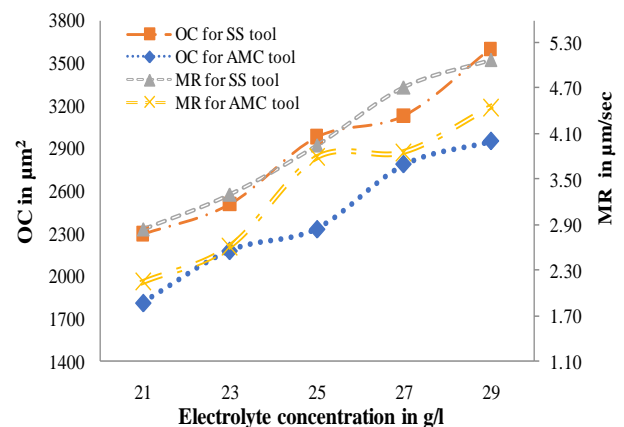


Figure 8. Influence of Electrolyte concentration on OC & MR.

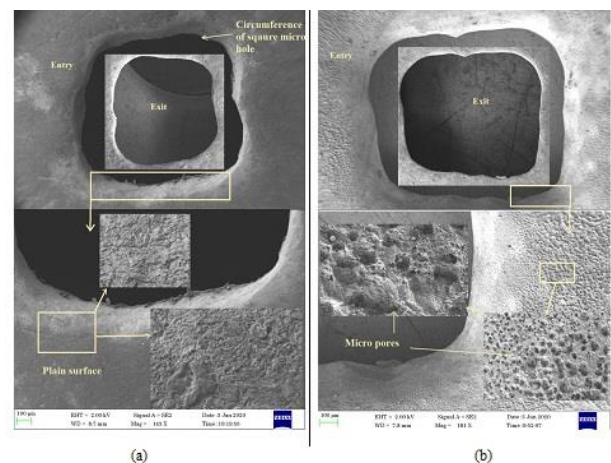


Figure 9. SEM images of the micro holes (a) SS tool (b) AMC tool.

### CONCLUSION

In EMM, there is no direct attempt at square hole fabrication, whereas the application of square holes is numerous in various fields. Hence, to reveal the process parameters of EMM, the square holes are fabricated. Two different tools were manufactured successfully to the required size on AMC and SS materials. The SS tool at the parameter combinations of 8 V, 85%, and 23 g/L shows 71.6% higher MR than

the AMC tool. Also, the AMC tool produces 43.22% less OC than the SS tool for the same parameter combination. Square micro hole machined with AMC tool shows sharp edges when compared to SS tool. The outer perimeter surface of the square micro hole machined with the AMC tool creates more micro pits. Hence, the AMC tool electrode can be considered for making sharp edges with lesser overcuts in EMM. Further, the surface modification of biomaterials through the generation of micro-dimples and micro-pits can be performed using the AMC electrodes. More experiments can be planned with different reinforcements to generate micro features like triangles and round and hexagonal-shaped holes.

### Acknowledgment

The authors thank the South India Textile Research Association SITRA, Coimbatore, for providing the FESEM facilities. In addition, the authors thank the management of Muthayammal Engineering College, Rasipuram, Tamil Nadu, for the encouragement and support. Finally, the authors are grateful to the management of Sona College of Technology, Salem, for providing the optical microscope facilities to verify the overcut area.

### REFERENCES

- [1] M.R. Pratheesh Kumar, K. Prakasan, K. Kalaichelvan, *Russ. J. Electrochem.* 52 (2016) 943-954.
- [2] M. Soundarrajan, R. Thanigaivelan, *Russ. J. Appl. Chem.* 91 (2018) 1805-1813.
- [3] B. Mouliprasanth P. Hariharan, *Exp. Tech.* 44 (2019) 259-273.
- [4] M. Soundarrajan, R. Thanigaivelan, *Russ. J. Electrochem.* 57 (2021) 172-182.
- [5] N. Pradeep, K.S. Sundaram, M. Pradeep Kumar, *Mater. Manuf. Processes.* 35(2020) 72-85.
- [6] M. Soundarrajan, R. Thanigaivelan, *Mater. Manuf. Processes.* 35 (2020) 775-782.
- [7] B. Liu, H. Zou, H. Luo, X. Yue, *Micromachines* 11 (2020) 118.
- [8] R. Kishi, J. Yan, *J. Micro Nano-Manuf.* 8 (2020) 010906 (6 pages).
- [9] S. Ayyappan, N. Vengatajalapathi, *Advances in Unconventional Machining and Composites*, in *Proceeding of AIMTDR 2018*, Anna University, Chennai, India (2018) p 255-268.
- [10] S. Maniraj, R. Thanigaivelan, *Mater. Manuf. Processes.* 34 (2019) 1494-1501.
- [11] J. Arab, H.K. Kannoja, P. Dixit, *Precis. Eng.* 60 (2019) 437-447.
- [12] T. Geethapriyan, P. Lakshmanan, M. Prakash, U.M. Iqbal, S. Suraj, *Advances in Manufacturing Processes*, in *Proceeding of AIMTDR 2018*, Anna University, Chennai, India (2018) p. 441-456.
- [13] G. Pang, K. Xin, F. Bu, T. Gao, *Int. J. Adv. Manuf. Technol.* 101 (2019) 2151-2164.
- [14] T. Paczkowski, J. Zdrojewski, *J. Mater. Process. Technol.* 244 (2017) 204-214.
- [15] R. Thanigaivelan, R. Senthilkumar, R.M. Arunachalam, N. Natarajan, *Surf. Eng. Appl. Electrochem.* 53 (2017) 486-492.
- [16] S.S. Anasane, B. Bhattacharyya, *Int. J. Precis. Technol.* 6 (2016) 231-248.
- [17] A.K. Verma, *J. Water Process. Eng.* 20 (2017) 168-172.
- [18] H.T. Yang, B.M. Chen, Z.C. Guo, H.R. Liu, Y.C. Zhang, H. Huang, R.C. Fu, *Trans. Nonferrous Met. Soc. China* 24 (2014) 3394-3404.
- [19] Y. Yao, G. Teng, Y. Yang, B. Ren, L. Cui, *Sep. Purif. Technol.* 227 (2019) 115684.
- [20] G. Pradeep Kumar, R. Thanigaivelan, R.M. Arunachalam, P. Paramasivam, *High Temperature Material Processes: Int. Q. High-Technol. Plasma Processes* 18 (2014) 27-43.
- [21] J.C.P.T. Oliveira, A.F. Padilha, *Rev. Esc. Minas* 62 (2009) 373-378.



THAYAMMAL  
GANESAN ARUL <sup>1</sup>  
VARATHARAJU PERUMAL <sup>2</sup>  
RAJASEKARAN  
THANIGAIVELAN <sup>3</sup>

<sup>1</sup> St Mary's Engineering  
College, Hyderabad, Telangana,  
India

<sup>2</sup> Department of Automobile  
Technology, Ethiopian Technical  
University, Addis Ababa, Ethiopia

<sup>3</sup> Department of Mechanical  
Engineering, Muthayammal  
Engineering College, Rasipuram,  
India

NAUČNI RAD

## PROUČAVANJE PERFORMANSE ELEKTROHEMIJSKE MIKROMAŠINSKE OBRAD KVADRATNOM KOMPOZITNOM ELEKTRODOM ZA BAKAR

*Upotreba mikro komponenti raste iz dana u dan u industrijama, kao što su vazduhoplovstvo, strujna kola, inkjetorske mlaznice i biomedicina. Među različitim netradicionalnim metodama mikromašinske obrade, elektrohemijaska mikromašinska obrada (EMO) pokazuje jedinstvene karakteristike, na primer, bez habanja alata, bez zaostalog napreznja i visoka tačnost. U ovom istraživanju, smatra se da EMO proučava efekat alata od nerđajućeg čelika (SS) kvadratnog oblika i aluminijumske metalne matrice (AMM) na bušenje kvadratnih rupa. Za proučavanje su uzeti u obzir značajni parametri procesa, kao što su napon obrade, radni ciklus i vodeni elektrolit natrijum-nitrata (NaNO<sub>3</sub>) različitih koncentracija. Performanse EMO procesa se procenjuju u pogledu brzine obrade i prekomerno bušenje. AMM alat pokazuje 43,22% manje prekomerno bušenje od SS alata pri kombinacijama parametara od 8 V, 85% i 23 g/l. Takođe, ista kombinacija parametara brzine obrade za SS alat je za 71,6% veća nega za AMM alat. Analiza slike sa skenirajućim elektronskim mikroskopom pokazuje da mikro kvadratna rupa generisana korišćenjem kompozitne elektrode pokazuje mikro udubljenja na obodu kvadratne rupe. Analiza energetski disperzivne rendgenske spektroskopije se sprovodi da bi se proverilo prisustvo i raspodela armature u AMM alatu..*

*Ključne reči: kvadratna elektroda, kompozitna elektroda, elektrohemijaska mikromašinska obrada, bakar.*